A Comparison of Matrix Microcracking in Thermoplastic Composites at Different Temperatures

Master of Science Thesis

Matej Moravčík

Delft University of Technology

TU Delft

A Comparison of Matrix Microcracking in Thermoplastic Composites at Different Temperatures

Master of Science Thesis

by

Matej Moravčík

to obtain the degree of Master of Science
at the Delft University of Technology,
to be defended publicly on Wednesday September 18, 2024 at 14:00.

Student number:	5010926	
Project duration:	January 15, 2024 – September 18, 2024	
Thesis committee:	Dr.ir. J.A Pascoe,	TU Delft
	M. Simonetto, PhD ,	TU Delft
	Dr.ing. S. G. P. Castro ,	TU Delft
	Dr. N. Yue,	TU Delft

Cover:	D.A.L.E generated image (Modified)
Style:	TU Delft Report Style, with modifications by Daan Zwaneveld

An electronic version of this thesis is available at `http://repository.tudelft.nl/`.

This project received support from the Clean Hydrogen Partnership and its members under Grant Agreement 101101404 (COCOLIH2T). Views and opinions expressed are however those of the author(s) only and do not necessarily reflect those of the European Union or Clean Hydrogen Joint Undertaking. Neither the European Union nor the granting authority can be held responsible for them.

TU Delft

Co-funded by the European Union

Clean Hydrogen Partnership

Acknowledgements

I would like to express my deepest gratitude to all those without whom this master's thesis, and my journey through university, would not have been possible. Firstly, I am thankful to my supervisor, John-Alan Pascoe, for his invaluable guidance and calm demeanour, which helped me navigate the challenges encountered throughout this research. Special thanks go to Mirko S., whose support during his Postdoc enabled my thesis to reach new heights. I am also deeply grateful to the members of my thesis committee, for their valuable time.

Next, I would like to extend my heartfelt thanks to all the DASML technicians and TAs who played a crucial role in helping me successfully conclude the experimental part of this thesis, despite the numerous challenges of lab work. In particular, I would like to express my gratitude to Dave, Chantal, Victor, and Emma for their invaluable assistance and support.

I would like to extend my deepest appreciation to my family, whose encouragement to embark on this academic journey and unwavering support along the way have been invaluable. Without them, I would not be where I am today. I am also grateful to all the friends I have made along the way; your hard work and dedication inspired me to give my best. Lastly, I want to thank to Sara, whose inspiration and support have been my greatest motivation.

Matej Moravčík
Delft, September 2024

Summary

This thesis investigates matrix microcracking behaviour of TC1225/T800 thermoplastic composite at different temperatures. Understanding microcracking is crucial for cryogenic hydrogen storage applications in aerospace. The research aims to correlate room temperature microcracking data with low temperature conditions and provide a model that could predict the microcracking performance at cold temperatures based on experimental testing at room temperature. This reduces the need for extensive low-temperature testing. A comprehensive experimental and analytical approach was adopted.

Firstly, the material properties such as longitudinal stiffness, transverse stiffness, tensile strengths, and shear modulus were evaluated. This baseline data was essential for understanding the fundamental mechanical behaviour of the material, and was used to determine local ply stresses.

A detailed investigation into residual stresses due to thermal effects was also conducted. The study employed dynamic mechanical analysis (DMA) to understand the matrix stiffness evolution, which was then translated into the transverse stiffness of the composite lamina. The residual stresses were analysed using Classical Laminate Theory (CLT) models, which were expanded to account for temperature-dependent properties and thermally induced stresses. The found residual stresses using the parameter evolving model were found to be on average 1.85x smaller on average than using constant room temperature inputs. The research demonstrated that thermoplastic composites exhibit significant internal stresses that influence their mechanical behaviour at cryogenic temperatures. A detailed understanding of these stresses is crucial for predicting microcracking patterns and optimizing material performance.

Microcracking tests focused on cross-ply laminates, and the results were analysed using a Weibull statistical model. The Weibull model was used to capture the cumulative damage progression and inherent data skewness. The first analysed phenomenon was thickness effect. Samples of $[0/90_n/0]$, where n = 1, 2, 4 were tested to access the influence of increasing transverse ply thickness. The experimental testing showed very little influence of the transverse ply thickness on microcracking performance. The single ply (n = 1) performed the best, while the two and the four middle plies had similar performance.

The correlation between room temperature tests and cold temperature (-65°C) performance was not conclusively established. Among the five different ply configurations tested at both temperatures, two cases showed good agreement between the predicted performance based on room temperature data and the experimentally observed values. In two other cases, the material exhibited better performance at cold temperatures than at room temperature. In the final case, the temperature shift required to match the cold temperature test results was underestimated. Consequently, while room temperature tests can provide some insight into the material's performance at colder temperatures, the correlation using residual stresses as a predictor was not fully confirmed.

For future research, it is recommended to focus on analysing the high-cycle fatigue performance of the material, as this is more representative of actual usage scenarios. Additionally, the observation that microcracks can initiate at very low load levels suggests that limiting the maximum allowable stress to prevent microcracking is not practical. Therefore, it is crucial to investigate how crack density affects the material's permeability and to determine the critical crack density level at which cracks connect to form a continuous path, allowing hydrogen to leak.

Contents

List of Figures

List of Tables

Nomenclature

Abbreviations

Abbreviation	Definition
AE	Acoustic Emissions
AFP	Automated Fibre Placement
ASTM	American Society for Testing and Materials
ATL	Automated Tape Laying
CDF	Cumulative Distribution Function
CD	Crack Density
CFRP	Carbon Fibre Reinforced Polymers
cH_2	Cryogenic Hydrogen
CLPT	Classical Laminated Plate Theory
CLT	Classical Laminate Theory
COCOLIH2T	COmposite COnformal LIquid H_2 Tank
COPV	Composite Overwrapped Pressure Vessel
CO_2	Carbon Dioxide
CT	Computer Tomography
CTE	Coefficient of Thermal Expansion
DIC	Digital Image Correlation
DMA	Dynamic Mechanical Analysis
EP	Epoxy
FBG	Fibre Bragg Grating
HDPE	High-Density Polyethylene
LH_2	Liquid Hydrogen
LM	Low-Melt
PA	Polyamide
PAEK	Polyaryletherketone
PEEK	Polyether Ether Ketone
RS	Residual Stress
RT	Room Temperature
SFT	Stress-Free Temperature
SFM	Scanning Force Microscopy
TRA	Transverse
UD	Unidirectional

Greek Symbols

Symbol	Definition
α	Coefficient of Thermal Expansion
γ	Shear Strain
Δ	Change Indicator
δ	Elongation / Displacement
ϵ	Axial Strain
η	Scaling Factor
θ	Central Angle
κ	Curvatures

Symbol	Definition
ν	Poisson's Ratio
ξ	Reinforcing Factor
ρ	Aspect Ratio of Microcracking Unit
σ	Normal Stress
τ	Shear Stress

Other Symbols

Symbol	Definition
A	Area
c	Chord Length
E	Axial Modulus
F	Probability of Failure
G	Shear Modulus
L	Length
M	Moment per Unit Length
m	Shape Parameter
N	Force per Unit Length
P	Force
Q	Compliance Matrix
R	Radius
S_{xy}	Tensile Strength in xy Direction
s	Sagitta Length
T	Temperature
V	Volume Fraction
u, v, w	Displacements
∂	Partial Derivative

1 Introduction

The use of fibre-reinforced polymers (FRPs) for aerospace pressure vessels dates back to the 1950s [1], offering a lightweight yet strong alternative to traditional materials. The recent surge in demand for lightweight hydrogen storage solutions is driven by ambitious sustainability goals aimed at achieving net-zero carbon emissions in aviation by 2050 [2]. One of the key strategies to achieve this is the development of hydrogen propulsion technologies, which leverage hydrogen's high specific energy—a critical factor for commercial aircraft applications. The volumetric energy density of hydrogen is optimized by storing it in liquid form, reducing its volume by about one-third compared to storage at 20°C and 35 MPa [3]. However, this adds complexity to the storage system, which must be lightweight, safe, and capable of sustaining cryogenic conditions.

The safe and efficient storage of hydrogen on-board future aircraft is an essential enabler of hydrogen technologies and presents one of the most complex aerospace engineering challenges the industry has ever faced. The COCOLIH2T (COmposite COnformal LIquid H2 Tank) project, addresses these challenges by proposing a disruptive tank concept that reduces the impact of weight and volume while ensuring safety. The project aims to develop a composite, vacuum-insulated liquid hydrogen (LH2) tank specifically for the aviation sector, using novel fabrication technologies to achieve more than a 60% reduction in production energy consumption and at least a 50% decrease in production time, significantly lowering manufacturing costs [4].

1.1. Purpose of This Thesis

The purpose of this thesis is to investigate matrix microcracking behaviour in thermoplastic composites under varying temperature conditions. Given the critical importance of cryogenic storage solutions for hydrogen in future aerospace applications, understanding microcrack initiation and propagation at low temperatures is vital. This research aims to explore how data from room temperature tests can be used to predict microcracking behaviour under colder conditions, thereby reducing the need for extensive and costly low-temperature testing.

The steps taken to correlate low-temperature testing with room temperature testing and to establish the minimum requirements for a predictive model are outlined in Figure 1.1. The flowchart is divided into three main sections:

- **Material Characterization** (Yellow Boxes): This section details the steps to establish an analytical material model that accurately predicts the elastic response to mechanical loading across a range of temperatures.
- **Residual Stress Analysis** (Green Boxes): This part focuses on assessing how a residual stress model, with temperature-dependent input parameters, can accurately predict residual stresses induced by thermal loading. This thermal loading simulates the storage of gases at low temperatures. It also includes an evaluation of the material's heat treatment.
- **Microcracking Testing** (Gray Boxes): This section covers microcracking tests conducted at room temperature and -65°C. The experimental data are processed using a Weibull model, which captures the cumulative nature of damage progression and accounts for the inherent skewness of microcracking data.

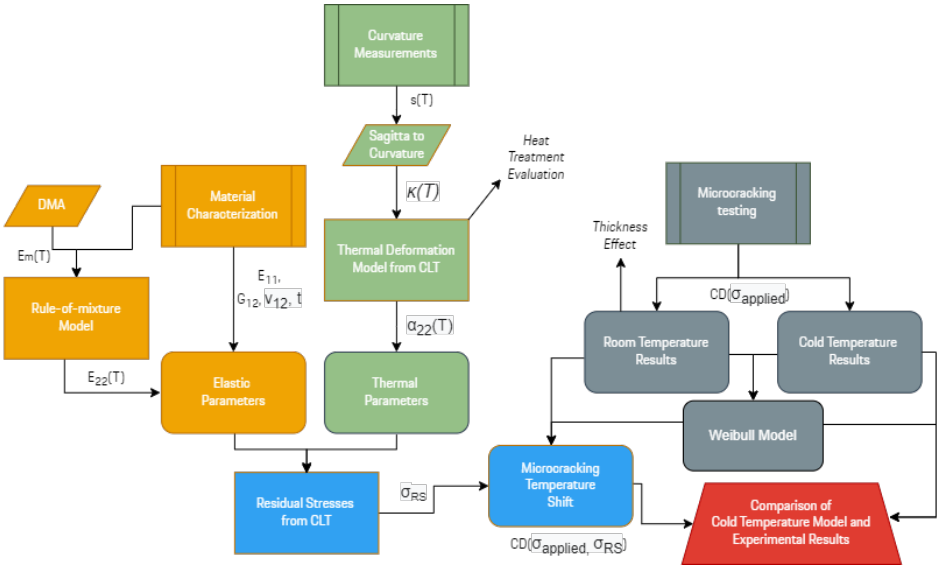

Figure 1.1: Flowdiagram of the Research Steps.

The provisional model outputs (Blue Boxes) represent the final residual stresses, which are then used to predict the material's low-temperature microcracking performance by shifting the room temperature test results based on the calculated residual stress. The final step of this thesis is to compare the predicted performance to experimental data obtained at -65°C.

1.2. Structure of the Report

This thesis is organized into six content chapters. The next chapter, chapter 2, provides the context for the research through a comprehensive literature review. It begins with an introduction to the types of composite pressure vessels. Following that, the mechanical properties of composite materials at low temperatures are discussed. The discussion then shifts to damage mechanisms in composites, including matrix microcracking and its implications for hydrogen permeation. Next, the multiscale nature of residual stresses is considered within the context of designing composite cryogenic tanks. The subsequent sections examine the limitations of using classical failure criteria for microcracking prediction and review experimental damage detection strategies employed in microcracking tests. Finally, the research gap is identified, and the research questions are stated.

Chapter 3 outlines the techniques and procedures used in all experiments. It begins with material characterization, which includes both quasi-static tensile testing and dynamic mechanical testing at various temperatures. Following this, the logic behind interrupted quasi-static tensile testing for observing microcracks is explained. Finally, the chapter discusses the experiments involving warpage in non-symmetrical layups to assess residual stresses.

The next chapter focuses on the methodology of the analytical models used in this research. The process of translating DMA results into lamina transverse stiffness evolution is detailed in chapter 4. The basics of the Classical Lamination Theory (CLT) models are also discussed, along with the expansion of this model to include thermally induced stresses. Finally, the Weibull statistical model for microcracking is introduced.

The results of all experiments are presented in chapter 5.This chapter begins with the presentation of material characterization properties. It then showcases the microcracking graphs for all tested layups at both temperatures. Detailed images, assisted by computer tomography, are also included. The chapter concludes with the evaluation of residual stresses.

Chapter 6 begins with a discussion on the temperature evolution model of transverse stiffness. It then evaluates the effects of heat treatment and residual stresses. The chapter also explores the thickness effect in microcracking as well as the temperature effect, drawing correlations between room temperature and cold temperature microcracking tests.

The final chapter, chapter 7, summarizes the key findings, discusses the implications and limitations of the results, and provides recommendations for future research.

2

Literature Review

The exploration of advanced composite materials for linerless liquid hydrogen storage applications has seen a revival of interest after the historical setback experienced with the rupture of the X-33 composite tank [5], an event that temporarily dampened the momentum of research in this field. However, recent geopolitical shifts and technological advancements have reignited the pursuit of innovative solutions in composite tank technology. This literature review aims to provide a background on thermoplastic composites research, with a specific focus on micro-cracking phenomena, which are critical to the integrity and performance of cryogenic tanks.

The European Composite Conformal Liquid H2 Tank (COCOLIH2T) project represents a component of this renewed research effort. The European Commission is aiming to cut CO_2 emissions per passenger kilometre by 75%. Hydrogen (H_2) and other alternative fuels are viewed as pivotal in achieving a zero emissions future for aviation [4]. Hydrogen is a high potential fuel for future commercial aviation because it has a high energy capacity per unit mass and emits no greenhouse gases during use [6]. The adaptability of hydrogen, capable of being produced from a broad spectrum of primary energy sources, offers a decentralised and dependable fuel supply for the aviation industry [7].

However, the transition to using hydrogen as a fuel for aircraft poses several challenges [8]. The lower volumetric energy density of hydrogen results in larger fuel tanks, which in turn reduces the aerodynamic efficiency of such aircraft compared to those powered by kerosene [9].

2.1. Composite Pressure Vessels

Pressure vessels are classified into Types I. - V. [10] as can be seen in Figure 2.1. The simplest design is Type I., which is a fully metallic pressure vessel. The Types II. to IV. are commonly referred to as composite overwrapped pressure vessels (COPVs). Whereas the Type II. and the Type III. use a metallic liner, the Type IV. uses a polymeric liner, further increasing the weight efficiency of the tank [11]. When metallic materials are exposed to high-pressure hydrogen, they encounter issues due to the diffusion of hydrogen atoms into their lattice structure [12]. The so-called hydrogen embrittlement leads to premature cracking of the structure and brittle failure [13]. Usage of plastic liner mitigates this issue. Materials including High-Density Polyethylene (HDPE) and Polyamide (PA) offer low hydrogen permeability, high cryo-toughness [14] while being cost-efficient [15]. However, there is still a mismatch between the CTE (Coefficient of Thermal Expansion) of the composite over-wrap and the liner, leading to debonding and separation of the plastic liners under cryogenic cyclic stress [16].

To address the issue of the strain compatibility of the liner and the composite over-wrap while offering up to 20% weight reduction [18] [19], linerless composite pressure vessels (CPVs) of Type V. were developed. For space applications, the research on linerless technology began in the 1980s [20]. The first materials used for such purpose were thermosetting, carbon fibre reinforced composites with matrix such as epoxy (EP), phenolic, polyester, bismaleimide resins. However, the high cross-link density diminishes the fracture toughness and, therefore, the capacity to resist crack initiation. This limitation significantly constrains their usability in cryogenic environments [21].

These constraints can be mitigated either by reducing the cross-link density of the thermoset resin or by introducing heterogeneous phases through the addition of substances like rigid inorganic

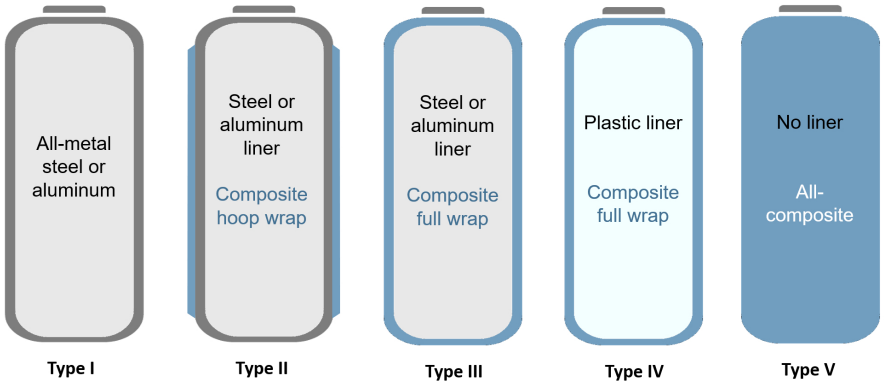

Figure 2.1: Five Types of Pressure Vessels Illustrated [17].

nanomaterials or soft polymers [22].

Thermoplastics demonstrate a significant enhancement in fracture toughness compared to thermosets, highlighting their strong potential for cryogenic applications. Thermoplastics can be stored indefinitely at room temperature without any adverse effects, showing better mechanical properties, the absence of a curing process, less hazardous chemical compositions, and the possibility of recycling [22].

Nevertheless, the use of all-composite materials in the production of linerless cryogenic hydrogen (cH2) storage vessels encounters two primary obstacles: mechanical failure at cryogenic temperatures and hydrogen leakage [23].

2.2. Composite Materials at Low Temperatures

The mechanical properties of the matrix are highly dependent on temperature [24]. The decrease in temperature reduces the thermal energy available to the polymer chains, thus decreasing their mobility [25]. This reduction in mobility stiffens the material, increasing its modulus of elasticity and yield strength. The material responds more elastically to deformation rather than plastically, which can also lead to an increase in its brittleness [26]. Polyether ether ketone (PEEK), a widely utilised matrix in thermoplastic composites, exhibits beta relaxation at approximately -30°C, which leads to alterations in its thermomechanical properties. Hine et al. reported a noticeable reduction in plasticity for PEEK at temperatures below -60°C [27], thereby confirming that the matrix's contribution to the composite's mechanical response is temperature-dependent [28].

The temperature-dependent evolution of mechanical properties in pure thermoplastic PEEK cannot be directly translated to the transverse lamina stiffness in composite materials. Zhang [29] tested PEEK and AS4/PEEK material at 4.2 K, 77 K, and 300 K. The axial stiffness of pure PEEK increases linearly across this temperature range, while the transverse lamina stiffness shows a bilinear evolution. The stiffness of PEEK increases by 100%, whereas the transverse lamina stiffness increases by 40%, and the longitudinal stiffness exhibits only a 10% increase. Matrix-dominated shear properties also show significant evolution with temperature.

Barnes et al. [30] studied the evolution of thermal parameters with temperature for AS4/PEEK. The longitudinal coefficient of thermal expansion (CTE) shows a slight variation, starting with small positive values around 350 K, dropping to zero, and then returning to positive values around 60 K. While the exact CTE values depend heavily on the type of fibre used, this quadratic trend in evolution is consistent across all tested PEEK carbon fibre-reinforced materials as seen in Figure 2.2a.

The transverse coefficient of thermal expansion (CTE) for PEEK material reinforced with carbon fibres shows little variation across different types of carbon fibres when measured at 296 K [30]. The evolution of transverse CTE with temperature for AS4/PEEK is illustrated in Figure 2.2b. The change from 100 K to 400 K is significant and, in absolute terms, exceeds the variation in CTE parallel to the fibre direction. This confirms that matrix-dominated laminate properties are more influenced by changes in temperature compared to fibre-dominated properties.

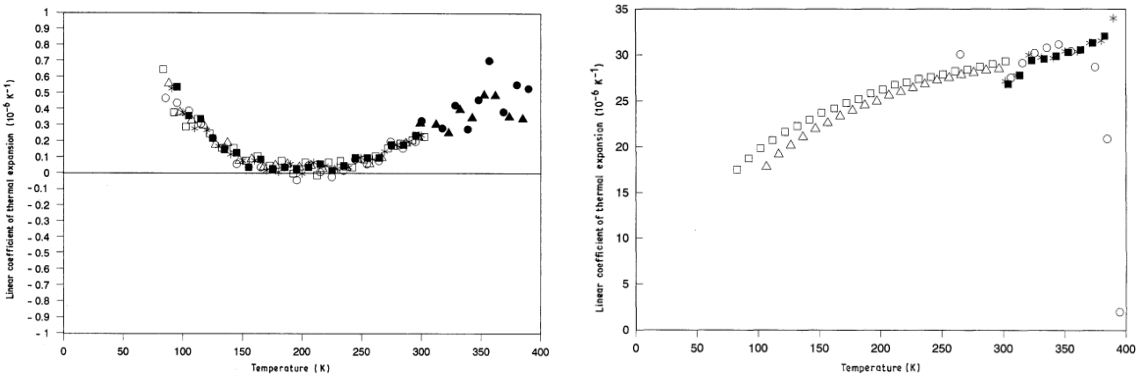

(a) Variation with Temperature of Linear CTE Parallel to the Fibre Direction.

(b) Variation with Temperature of Linear CTE at 90° to the Fibre Direction.

Figure 2.2: Temperature Evolution of CTE_{11} and CTE_{22} for AS4/PEEK Taken from Ref. [30].

Composite materials, especially thermoplastic composites produced through methods such as Automated Fibre Placement (AFP), exhibit a strong dependency on processing conditions that can greatly affect their low-temperature performance. Among these conditions, humidity during manufacturing plays a crucial role. Research indicates that humidity can have a substantial impact on the microcracking behaviour of composites under freezing conditions [24]. Moisture absorbed during processing can expand when exposed to freezing temperatures, promoting microcrack formation and propagation, which deteriorates the material's integrity. Although this effect is not an inherent characteristic of the composite material itself, it underscores the importance of precise process control.

2.3. Damage Mechanism in Composites

The composites utilized in Composite Pressure Vessels (CPVs) are subject to the same damage mechanisms as those observed in other composite structures. According to Talreja [31], these primary mechanisms include:

- Interfacial debonding
- Matrix microcracking, also referred to as intralaminar cracking
- Interfacial sliding
- Delamination, known as interlaminar cracking
- Fibre breakage
- Fibre microbuckling

These damage mechanisms, along with their interactions as the stress level within the structure increases, lead to mechanical failure, typically indicated by a reduction in the stiffness of the structure.

In the context of cryogenic hydrogen (cH2) tanks, which are designed to store highly volatile cryogenic propellants, the choice of material is critical. Laminates are selected for their low permeability to various gases, especially hydrogen. The permeability is largely attributed to the small molecular diameter and high kinematic viscosity of hydrogen [11]. Within this framework, classical mechanical failure, accompanied by a drop in mechanical properties, does not represent the primary concern. More critical is the issue of propellant leakage due to permeation — a phenomenon that may occur before any noticeable degradation in mechanical properties. The predominant damage mechanism leading to leakage in composite materials has been identified as matrix cracking.

The initiation of damage, characterised by transverse matrix cracking, requires the lowest energy input, whereas the final stages, such as fibre breakage, demand considerably higher energy levels. Damage initiation typically occurs in areas of reduced strength, notably at the matrix-fibre interfaces and within the matrix itself (Figure 2.3), resulting in intralaminar cracks. These cracks, which are generally parallel and uniformly distributed, represent the initial phase of damage. It has been observed that crack density increases with strain rate [32]. Although this form of damage exerts minimal impact on the ultimate strength of the material, the formation of microcracks establishes interconnected 'channels', that allow gas to escape [33].

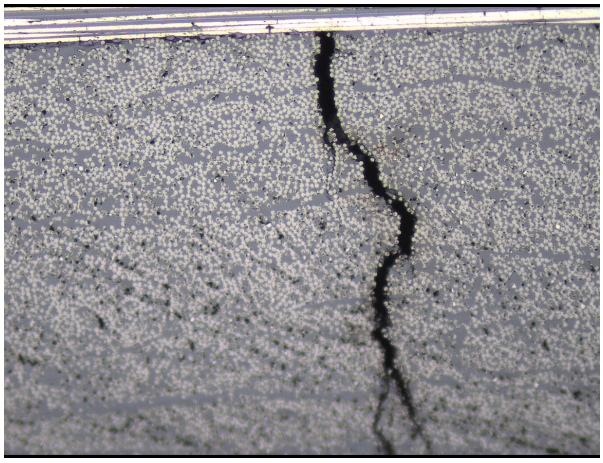

Figure 2.3: Matrix Damage in TC1225/T800 Thermoplastic Composite.

A significant body of research has been devoted to the study of permeation dynamics at cryogenic temperatures. Empirical evidence suggests that the rate of gas leakage escalates in conjunction with mechanical strain, crack density, and a decrease in temperature. This can be explained by the decreasing critical energy release rates for temperatures between room temperature (RT) and 4 K observed for woven carbon reinforced thermoset composites [34]. The damage process for CFRPs is well described for composites at room temperature. However, the mechanical properties of composites cannot be simply transferred to the cryogenic condition [35].

Gas permeation through composite materials can be characterised by the damage state and load state of the laminate [36]. Numerous studies have examined gas permeation in both thermosetting and thermoplastic composites [37]. The permeability of carbon fibre reinforced thermoplastic PEEK is notably low, making it a promising material for cryogenic hydrogen storage applications [38]. Nonetheless, it is observed that the rate of leakage increases with increasing damage. While thermoplastic matrix composites, due to their superior matrix toughness, are expected to outperform their epoxy-based counterparts, Nairn [39] observed a similar behaviour between thermoplastic and thermosetting composites, despite the difference in toughness. This phenomenon was attributed to the higher internal thermally induced stresses present in thermoplastic composites, highlighting their significance in the design of cryogenic hydrogen storage systems.

2.4. Residual Stresses

The phenomenon of residual stress formation is inherent to all fibre-reinforced polymers, due to their intrinsic inhomogeneous nature. Residual stress can be conceptualised as a stress that persists within a material despite the absence of external forces or thermal gradients. Thermal stress can be defined as a type of residual stress that occurs within a material due to variations in temperature [40].

Thermal residual stresses within a laminate manifest themselves across very different, discontinuous scales, ranging from the nanoscale to the macroscale.

2.4.1. Nanoscale Residual Stresses

At the nanoscale, for semi-crystalline polymers, a significant correlation has been identified between residual stresses, crystal orientation, and mechanical properties [42]. The distribution and magnitude of these stresses are significantly modulated by the microstructural characteristics of the polymer, in particular the orientation and dispersion of crystalline domains within the amorphous matrix. This complexity in the formation of residual stresses is further compounded when considering the crystallinity gradient across the ply thickness, as reported by El Bayssari [43]. The surface of the ply typically exhibits an amorphous region, attributable to the rapid cooling rates associated with Automated Tape Laying (ATL) and Automated Fibre Placement (AFP) processes, with crystallinity increasing towards the ply's midpoint. The absence of nanoscale residual stress modelling in the literature, particularly for applications within a design framework, can be primarily attributed to the computational challenges associated with nanoscale modelling. Given the complexities of accurately simulating the behaviour of

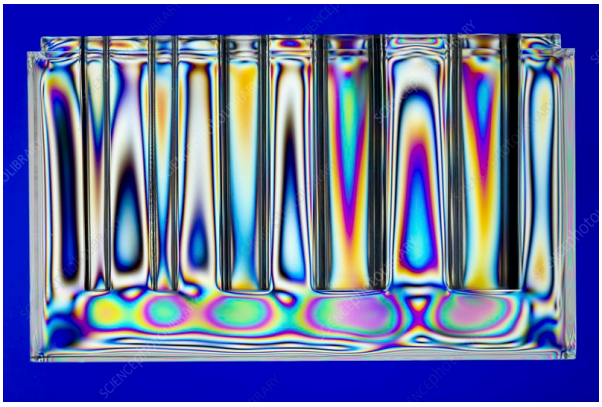

Figure 2.4: Example of Photo-Elastic Stress Effect [41].

materials at the nanoscale, the computational resources required to extend these models to a physically meaningful scale become prohibitively expensive.

2.4.2. Residual Stresses at Microscale

Transitioning to the microscale, thermal residual stresses emerge as a consequence of the difference in the Coefficient of Thermal Expansion (CTE) among the composite constituents, as shown in Figure 2.5. The critical factor in this context is the disparity in CTE values between the fibre and the matrix. This heterogeneity, between matrix and carbon fibres, leads to different shrinkage behaviour (curing or crystallisation shrinkage for thermosetting and thermoplastic matrices respectively), which in turn induces residual stresses. For composites with thermoplastic matrix, during the cooling phase from the melt state, the thermoplastic matrix exhibits a greater degree of shrinkage relative to the fibres. Moreover, specifically for (semi-) crystalline matrices the shrinkage is attributed not only to the higher CTE of the matrix material, but also to the crystallisation shrinkage that occurs with the formation of crystals. Consequently, this differential shrinkage results in residual strains within both the fibre and the matrix components of the composite [43]. Nguyen et al. developed a model to characterise the thermal stresses at the constituent level within thermosetting composite materials used in overwrapped pressure vessels. Utilising a homogenisation scheme, they transitioned their analysis to the lamina level. Their findings revealed that the actual epoxy matrix properties in a composite, compared to those of the neat resin, exhibit significant differences. This led them to believe that the thermal stresses would have a greater effect than initially predicted by their model [44].

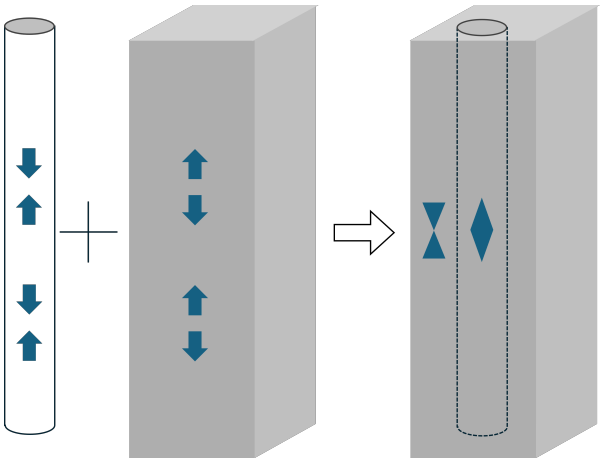

Figure 2.5: Mechanism Behind Microscale Residual Stresses [45].

2.4.3. Mesoscale Residual Stresses

At the mesoscale, residual stresses manifest across ply-to-ply interfaces, due to the inherent anisotropy of each subsequent lamina, as shown in Figure 2.6. In general, these stresses arise primarily from the difference in the coefficients of thermal expansion (CTE) in the transverse and longitudinal directions of the plies. For thermoplastic cross-ply composites structures, the plies oriented at 90° mechanically constrain those at 0° during the cooling process, and vice versa, due to the directional differences in thermal shrinkage [46]. The analysis of mesoscale thermal stresses represents a prevalent approach within composite materials' research, largely because it allows for the direct incorporation of thermal loading effects on each lamina within the framework of Classical Laminate Theory (CLT) as in Ref. [47]. Residual stresses calculated using CLT have been observed to be overestimated when compared to experimental results [48]. The primary reason for this discrepancy is that CLT assumes that thermal and mechanical material properties are independent of temperature.

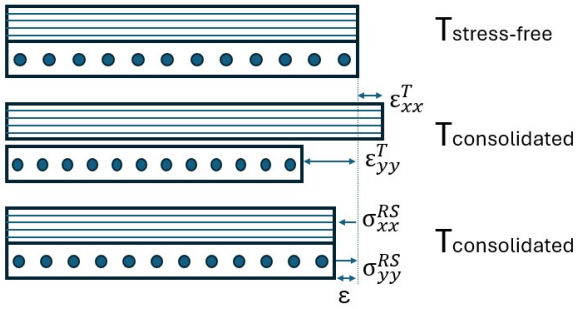

Figure 2.6: Mechanism Behind Mesoscale Residual Stresses.

2.4.4. Residual Stresses at Macroscale

On the structural or macroscale, the development of residual stresses can be attributed to gradients in cooling rates or temperature conditions across the thickness of the composite laminate or structure, culminating in a distinct distribution of residual stresses through the laminate's thickness. Typically, in a laminate of considerable thickness, the cooling rate in the centre of the laminate is lower than at the surface. At a specific temperature point, while the centre plies may still be in the process of solidifying, the surface plies might have already solidified. As cooling progresses, the solidified surface plies mechanically constrain the shrinkage of the still-solidifying centre plies. This dynamic often results in a parabolic distribution of residual stresses, characterised by compressive stresses in the surface plies and tensile stresses in the centre plies [49].

Thermal residual stresses are generated by variations in temperature from a state considered to be free of internal stresses. The specific temperature at which a composite material is assumed to be free of internal residual stresses is referred to as the stress-free temperature. The mechanisms and various scales at which these stresses can manifest have been previously discussed.

During the manufacturing process, such stresses can occur, particularly for high-performance composites that require processing at elevated temperatures. For thermosets, the cure temperature is considered to be the stress-free temperature, as the matrix remains viscous at this stage, allowing for the relaxation of the fibres. In the case of thermoplastic composites, the stress-free temperature is generally associated with the glass transition temperature for amorphous or the peak crystallisation temperature for the semi-crystalline polymers [49]. As the composite material cools from this designated stress-free temperature, differential thermal expansions between the composite constituents lead to the introduction of residual stresses. Several models have been proposed to estimate thermal residual stresses at room temperature, incorporating various considerations to accurately predict these stresses in composite materials. In particular, El Bayssari [43] adopted the glass transition temperature as the stress-free temperature (SFT) for semi-crystalline PEEK in their modelling efforts. Similarly, Peron et al. [50] focused on predicting and comparing residual stresses in the PA66 matrix. Both models factored in the effects of crystallisation shrinkage. Peron et al. [50] also use a modified version of Classical Laminate Theory (CLT), which demonstrated reasonable agreement with empirically measured values within specific temperature ranges where the Coefficient of Thermal Expansion (CTE) of the laminate remains relatively constant.

2.4.5. Determination of Residual Stresses

Direct measurement of residual stresses is not possible. All measurements methods rely on indirect techniques. Parlevliet et al. [51] have categorised measurement techniques based on whether they use intrinsic or extrinsic material properties to infer these stresses.

Techniques based on intrinsic material properties include:

1. **Photo-elasticity:** Applicable only to materials with transparent matrices, this method relies on the stress-induced birefringence effect to visualise stress patterns.
2. **Micro-Raman Spectroscopy:** Suitable for semi-crystalline polymers, this technique's accuracy improves with the inclusion of aramid fibres in the composite, leveraging the shift in Raman spectra under stress.
3. **Electrical Conductivity of Carbon Fibre Reinforcement:** Utilised for carbon fibre reinforced composites, where stress can alter the electrical conductivity properties of the carbon fibres.

The techniques utilising the extrinsic material properties are:

1. **Embedded Strain Gauges:** Involves integrating strain gauges in the composite material to measure deformation due to internal stresses.
2. **Embedded Fibre Optic Sensors:** Fibre optic cables, when embedded in the composite, can detect stress through changes in light transmission properties.
3. **Embedded Metallic Particles:** Involves using X-ray diffraction on metallic particles embedded within a composite matrix to measure thermal deformation.
4. **Warpage of Non-Symmetric Laminates:** Observes the deformation patterns of non-symmetric laminates under thermal or mechanical loading.

Beyond these non-destructive techniques, other methods exist, including destructive and relaxation techniques like layer removal, where layers of the composite are removed sequentially to measure the stress relief at each stage.

Figure 2.7: X-33 Composite Sandwich Tank [52].

The critical role of thermal residual stresses in the structural integrity and failure of composite materials is underscored by numerous researchers. A notable example is the failure of the X-33 composite tank, in Figure 2.7, which has been largely attributed to significant residual stresses, with estimates suggesting that thermal stresses accounted for 56.5% to 84.6% of the total stress level [53], [24]. Furthermore, Grogan et al. [54] observed that thermal residual stresses in thermally cycled PEEK laminates were substantial enough to initiate damage. This highlights the necessity for integrity assessments and failure criteria that incorporate the effects of thermally induced residual stresses and their role in initiating microcracks in composite structures.

2.5. Failure Criteria

In general, failure criteria are used in composite analysis to predict the condition under which a material will fail, given applied loads and/or stresses. Failure criteria are developed based on empirical observations, experimental data, and theoretical understanding of the material behaviour under different loading conditions. The purpose of a failure criterion is to identify the threshold beyond which a material will no longer behave as expected, resulting in a loss of functionality, structural integrity, or complete fracture. This threshold can be defined in terms of stress, strain, energy, or a combination of these and other factors, depending on the material and the specific conditions it is subjected to. For fibre-reinforced composites, failure criteria must take into account different failure modes.

The failure criteria for continuous fibre-reinforced polymers and composite materials aim to predict the onset of failure under various loading conditions, as seen in Figure 2.8. These criteria take into account the anisotropic and heterogeneous nature of composites, offering different approaches to assess their failure mechanisms, such as matrix cracking, fibre breakage, and delamination. The most widely used and known failure criteria together with their main ideas are:

- **Maximum Stress Criterion:** This simple criterion predicts failure when the stress in any of the material directions exceeds its strength. It treats the composite's failure modes (fibre, matrix, and shear) independently and assumes linear elastic behaviour up to failure.
- **Maximum Strain Criterion:** Similar to the Maximum Stress Criterion, this approach predicts failure when the strain in any direction exceeds the allowable strain.
- **Tsai-Hill Criterion:** Based on the von Mises yield criterion for isotropic materials, the Tsai-Hill criterion modifies it to suit anisotropic composite materials. It predicts failure when a certain quadratic function of the stresses exceeds a critical value.
- **Tsai-Wu Criterion:** An extension of the Tsai-Hill criterion, the Tsai-Wu criterion incorporates different tensile and compressive strengths in the material directions. It predicts failure through a more comprehensive quadratic polynomial that includes interaction terms between the stress components.
- **Hashin's Criterion:** This criterion separates failure modes for fibre and matrix, including fibre tension/compression and matrix tension/compression.
- **Puck's Criteria:** This approach focuses on the matrix failure, particularly under transverse tension and compression. It is known for its ability to predict the onset of matrix cracking and delamination by considering the interaction between normal and shear stresses on the failure plane.
- **LaRC04 Criterion:** Addresses some of the limitations of previous criteria by providing a more accurate prediction of failure under a wide range of stress states, including those involving shear interactions.

The maximum stress, strain and Hashin criteria are favoured for their simplicity and minimal parameterisation. The Maximum Strength criterion uses (microscopic) strength parameters of the polymer matrix to model interactions between the matrix and inclusions. This *microscopic* approach shows good accuracy in predicting matrix cracking phenomena at cryogenic temperatures for thermoset matrix composites [56]. The adoption of microscopic failure criteria over macroscopic strength criteria is motivated by the limitation of the latter to consider only macroscopic average thermal residual stresses between adjacent laminate layers. Microscopic strength criteria, in contrast, facilitate consideration of internal stresses generated at microscopic scale. Furthermore, microscopic strength criteria do not need experimental characterisation of lamina strength parameters.

From the more advanced failure criteria, the LaRC03 criterion has been used to assess *macroscale* fractures in unidirectional fibre-reinforced composites. This principle incorporates in-situ strength parameters to predict the failure of fibre-reinforced laminates. For both the Puck and LaRC03 criteria, accurate determination of the fracture angle under compressive loading conditions is crucial for predicting matrix failure. However, in the context of thermoplastic materials, such experimental investigations to determine a typical fracture angle have yet to be conducted, leaving a gap in the application of these criteria to thermoplastic composites [57].

Another limitation of stress-based failure criteria is their tendency to fall short in accurately predicting the effects of ply thickness and position on microcracking behaviour in carbon fibre-reinforced composites. The ply thickness effect suggests that thinner plies generally suppress matrix

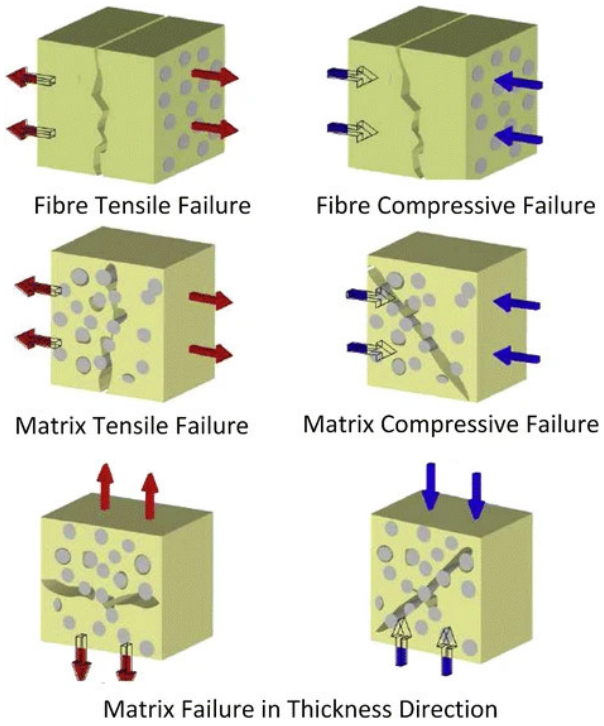

Figure 2.8: Failure Modes in Fibre Reinforced Composites [55].

cracking, thereby improving the overall mechanical performance of the composite. Thinner plies reduce stress concentration and delay the onset of cracks, enhancing damage tolerance [58]. Additionally, the position of plies within the laminate plays a significant role in the initiation and propagation of microcracks, with plies closer to the surface being more susceptible to damage [59]. The challenge arises because the stress predicted by Classical Lamination Theory (CLT) in transverse layers under axial loading is independent of ply position and has minimal dependence on ply thickness. Consequently, for stress-based failure criteria to account for these effects, they must incorporate in-situ strength parameters.

2.6. Damage Detection

This section critically examines methodologies for microcrack detection in continuous carbon fibre reinforced polymers (CFRPs), highlighting their significance for ensuring structural integrity.

Several techniques have been successfully employed for in-situ crack detection during material testing. Acoustic emission technique is one of them. As outlined by Huguet et al. [60], it provides a framework for damage characterisation in composites, which has been further validated for crack growth studies by Pascoe et al. [61]. The Acoustic Emission (AE) technique utilizes piezoelectric transducers to detect transient waves generated by the rapid release of energy during damage events. The challenge in AE emission analysis lies in accurately correlating these emissions with specific damage mechanisms. Different types of damage produce distinct AE signatures, which are then analysed to identify the type and progression of damage within the composite. Optical methods, including the edge crack observation technique used by Xi Li [62], allow for the real-time observation of crack formation. Enhancing contrast for these observations can be achieved through dye penetrant methods. The disadvantage of this method is the need for very high quality surface polish and the method is quite time-consuming due to high magnification required to see the microcracks. Digital Image Correlation (DIC) offers a means to detect strain concentrations indicative of microcrack initiation, complementing the detection capabilities of Fibre Bragg Grating (FBG) sensors, which monitor strain changes via shifts in Bragg wavelength. The strain based methods are limited to very small detection area, in which no microcracks could be nucleated, leading to incorrect results.

X-ray computed microtomography (microCT) is a valuable tool for improved post-test examination of the crack tip. This technique enables the detailed characterisation of internal flaw geometries, including

microcracking, by providing high-resolution images of the internal structure [63]. The disadvantage of CT is the time required for specimen preparation and subsequent analysis, as well as the small observation area that can be scanned. In cases where destructive methods are used to expose the crack tip within the laminate, microscopy techniques become instrumental for analysis. In particular, Scanning Force Microscopy (SFM) has been effectively utilised to evaluate the local mechanical properties of fibre-reinforced polymers, providing insights into the microscale interactions and damage mechanisms [64]. Again, SFM is limited by the sample size that fits inside the microscope.

2.7. Research Gap

Numerous micromechanical models have been developed to predict the stress onset of microcracking in composites, leveraging the micromechanical responses of the thermoset matrix fibre representative volume. Techniques such as the Mori-Tanaka method, which fall into the category of trans-scale or homogenisation approaches, have been used to evaluate mesoscale failure scenarios. These models primarily addressed simple stress states induced by transverse tension or tension-tension loading in the 90-degree ply [56, 65, 66, 67, 68, 69]. The hexagonal unit cell approach does not accurately capture all the complexities, such as material heterogeneity, structural imperfections, or interfacial properties. Additionally, the effect of thermal cycling on thermoplastic composites down to cryogenic temperatures and the critical role of residual stresses have been subjects of several investigations [54, 70, 71]. Sophisticated models have been proposed to determine residual stresses due to crystallisation and thermal expansion anisotropy [43].

Despite the extensive research on micromechanical models and thermal cycling of composites, the literature does not reveal any study that explores the correlation between room temperature testing of a specific material (and possibly layup) and its cryogenic response. Establishing such a correlation could significantly streamline the process of evaluating microcracking behaviour under cryogenic conditions, and replace it with more feasible testing at room temperature. Identifying a correlation would not only reduce the time and cost associated with cryogenic testing, but also aid in the comparative evaluation of different materials. By conducting tests at room temperature and analysing the outcomes alongside other known properties, it could become possible to infer the cryogenic performance of materials, providing a practical and efficient approach to material selection and performance prediction in cryogenic environments.

Despite the extensive understanding of residual stresses, damage formation in thermoplastic composites, and the underlying physics of failure, there appears to be a notable lack of the prediction of the cryogenic matrix cracking behaviour of thermoplastic composites. The literature currently lacks the essential mechanisms and material properties needed for accurate model predictions. Key factors that need to be considered include residual thermal stresses, the matrix stiffness change, the evolution of material toughness, variations in the coefficient of thermal expansion (CTE) of materials, the presence of manufacturing defects, and the distribution of fibres within the composite. These factors highlight the complexity of developing a predictive model, but also emphasise the scientific value and potential impact of addressing this research gap. The exploration of these variables offers a promising avenue for advancing the understanding of the behaviour of thermoplastic composites under cryogenic conditions, presenting a clear opportunity for novel research contributions. Therefore, two research questions were formulated:

”*How does the matrix microcracking evolution correlate between room temperature and colder temperature conditions?*”

and

”*To what extent and with what minimum requirements can a model, validated through room temperature testing, accurately predict this relationship?*”

3

Experimental Methodology

This chapter outlines a structured plan to better understand the mechanical responses of thermoplastic composites at different temperatures. The methodology is divided into two experimental phases. Firstly, comprehensive material characterisation at ambient and low temperature provides baseline mechanical properties of the thermoplastic composites. The subsequent phase will focus on assessing the initiation and evolution of matrix microcracking with cross-ply laminate configurations under applied stresses.

3.1. Material Characterization Procedures

The material used in this thesis is Toray Cetex® TC1225, a high-performance thermoplastic matrix reinforced with unidirectional Toray T800 carbon fibres. The matrix is a low-melting point semi-crystalline PAEK resin. The lower melting point allows for reduced processing temperatures compared to other high-performance plastics. Given the importance of minimizing residual stresses in cryogenic applications, the lower thermal stresses resulting from the reduced process temperatures make the TC1225 / T800 composite material a suitable candidate for cryogenic storage tanks. All specimens were manufactured from panels produced by the automatic fibre placement (AFP) technique and consolidated with a vacuum bag. The panels were cut to their final dimensions using a diamond saw. Finally, 30 mm glass-fibre composite tabs were bonded to each end of the samples to ensure better load introduction.The shape of the specimens used for material characterization and microcracking testing is illustrated in Figure 3.1. The highlighted observation area is specifically relevant for the microcracking tests.

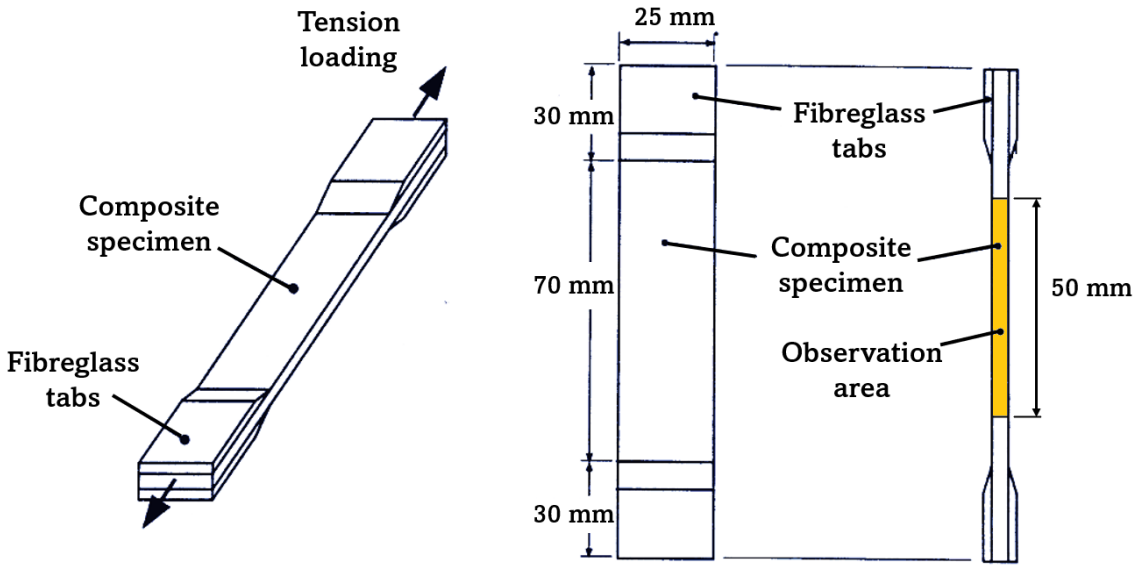

Figure 3.1: Tensile Coupon Specimen Configuration for Experimental Testing (adapted from Ref. [72]).

These specimens are used to determine various material properties. At room temperature (22°C), the following properties are measured: longitudinal stiffness (E_{11}), transverse stiffness (E_{22}), tensile strengths in the longitudinal and transverse directions (S_{11}, S_{22}), shear modulus (G_{12}), and Poisson's ratio (ν_{12}). For tests conducted at cold temperature (-65°C), the focus is on determining the longitudinal and transverse stiffness ($E11$ and E_{22}) and tensile strengths (S_{11} and S_{22}) in these directions. By comparing the elastic material properties at these two temperatures, it is possible to assess how these parameters change with temperature.

3.1.1. Methodology for Determining Ply Thickness

To determine the ply thickness, each received panel was measured at multiple points using a micrometer. The average thickness of these measurements was then divided by the number of plies in the panel to obtain the thickness of a single ply. These calculated ply thickness values were then used as inputs for the Classical Laminate Theory (CLT) model.

3.1.2. Tensile Properties of the Material

The first set of tests determined the in-plane tensile properties of the TC1225/T800 material. Table 3.1 shows the designed specimens. A Zwick 250 kN tensile machine with a 250 kN load cell was used for testing. Strain was determined using a combination of extensometer displacement and axial/biaxial strain gauge readings. The samples were loaded quasi-statically under displacement control at 0.1 mm/min. The Zwick machine recorded data 10 times per second. Hydraulic clamps were used for room temperature testing, while wedge clamps were used for low-temperature testing to avoid the risk of freezing the hydraulic fluid.

Table 3.1: Definition of Specimens Used for Testing of Tensile Properties.

Name	Layup	Heat Treatment	Testing Temperature	Wanted Properties	Nominal width	Nominal length
UD	$[0°]_6$	No	22°C -65°C	E11, S11, ν12	15 mm	150 mm
TRA	$[90°]_6$	Yes	22°C -65°C	E22, S22	25 mm	150 mm
SHR	$[\pm 45]_6$	No	22°C	G12	25 mm	150 mm

The testing followed specific ASTM standards for different specimen orientations. For specimens oriented at 0° and 90°, the ASTM D3039/D3039M-17 standard was used to determine the tensile properties of polymer matrix composite materials. For specimens oriented at ±45°, ASTM D3518/D3518M-18 standard was used to determine the shear properties through tensile testing.
The ASTM D3039/D3039M-17 specifies the following relations for tensile stress/strength:

$$S_t = P^{max}/A \tag{3.1}$$

$$\sigma_i = P_i/A \tag{3.2}$$

where S_t is the ultimate tensile strength, P^{max} is the maximum force before failure, σ_i is the tensile stress at the ith data point, P_1 is the force at the ith data point and A is the average cross-sectional area. If an extensometer is used, the tensile strain is calculated as:

$$\epsilon_i = \delta_i/L_g \tag{3.3}$$

where ϵ_i is the tensile strain at the ith data point, δ_i is an extensometer displacement at the ith data point and L_g is the extensometer gauge length. Finally, the modulus of elasticity and the Poisson's ratio are calculated as:

$$E^{chord} = \Delta\sigma/\Delta\epsilon \tag{3.4}$$

$$\nu = -\Delta\epsilon_t/\epsilon_l \tag{3.5}$$

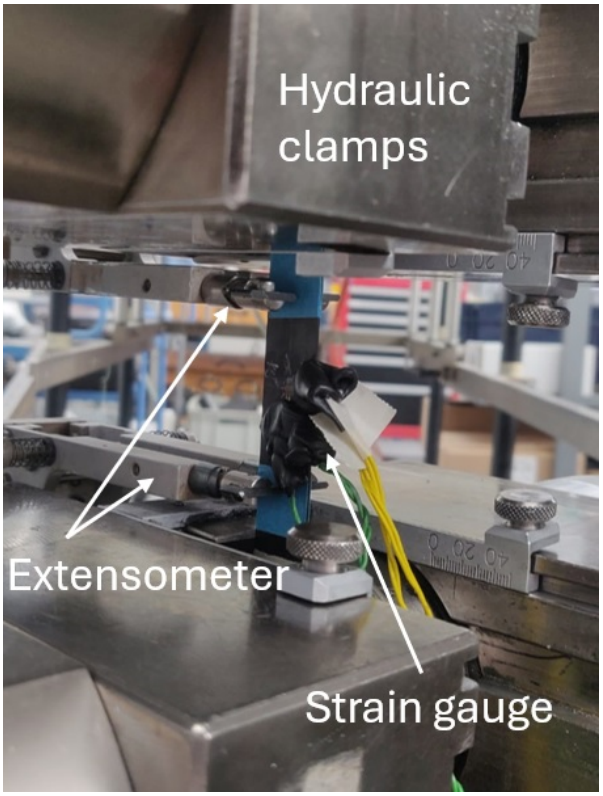

Figure 3.2: Tensile Test Setup Used for Room Temperature Tests.

The ASTM D3518/D3518M-18 specifies the following relations for the shear response of polymer matrix composites:

$$\gamma_{12i} = \epsilon_{x_i}/\epsilon_{y_i} \tag{3.6}$$

$$\tau_{12_i} = P_i/2A \tag{3.7}$$

$$G_{12} = \Delta\tau_{12}/\Delta\gamma_{12} \tag{3.8}$$

where ϵ_{x_i}, and ϵ_{y_i} are the longitudinal and lateral normal strain at the ith data point, γ_{12i} is the engineering shear strain at the ith data point, τ_{12_i} is the shear stress at the ith data point, and finally, G_{12} is the shear modulus of elasticity. More details on material characterization can be found in the CHADA material characterization workflow in Appendix A.

3.1.3. Dynamic Mechanical Properties of the Material

Dynamic Mechanical Analysis (DMA) testing is a good tool for understanding material behaviour at low temperatures. By subjecting a material to oscillatory stress while systematically varying the temperature, DMA provides insights into the material's viscoelastic properties, such as storage and loss moduli and damping. DMA helps identify changes in the material's mechanical performance, such as altered damping characteristics. For rheologically simple polymers, DMA testing allows the very low test temperature to be shifted to a higher, more readily achievable temperature by testing the material at a higher frequency. The foundation of time/temperature superpositioning lies in the fact that molecular relaxation or rearrangement processes in viscoelastic materials accelerate at higher temperatures, creating a direct equivalency between time (or measurement frequency) and temperature. Consequently, the duration of these processes can be shortened by performing measurements at elevated temperatures and then shifting the resulting data to represent lower temperatures [73].

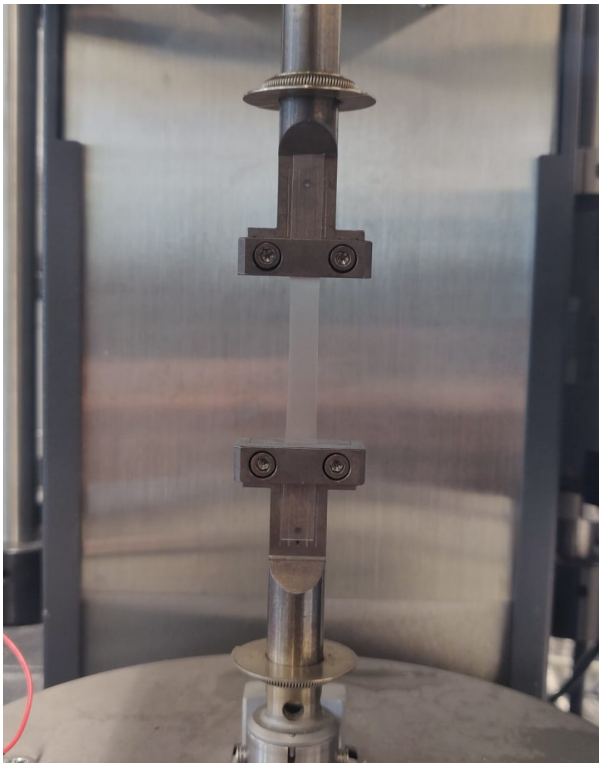

Figure 3.3: DMA Test Setup.

Due to the limitations of the DMA machine, Toray Cetex® TC1225 composite prepreg material could not be tested with this set-up due to its high stiffness. Therefore, the material used for DMA testing was polymer Victrex AE™ 250 LM-PAEK, which, to the author's best knowledge, is very similar or even identical to the matrix material of Toray Cetex® TC1225. The polymer film specimen used was 0.06 mm thick, 8.5 mm wide, and 35 mm long. The testing plan included a tensile frequency sweep from 0.1 Hz to 100 Hz across a temperature range from -150°C to 140°C. Dynamic Mechanical Analysis (DMA) allows the matrix tensile modulus to be determined as a function of time (frequency) and temperature, which is then used to determine the lamina transverse stiffness as a function of temperature as described in section 4.1.

3.2. Microcracking Testing and Characterization Procedures

Microcracking testing and characterization involved two primary steps. Initially, the material is subjected to tensile load up to a predetermined level. Then, the specimen is optically scanned using Keyence VK-X1000 confocal microscope to photograph the cracks in each 90° layer. This process was repeated, with the specimen being loaded to progressively higher levels and subsequently scanned, until sufficient damage was observed in the material. The edge observation methodology was adapted from the work of Xi Li [62].

The tested specimen layups are specified in Table 3.2. During the initial phase of testing, various layups, including non-cross-ply configurations, were examined. However, due to the less distinct crack formation observed in these configurations, the focus was shifted to cross-ply specimens in order to obtain clearer and more consistent results.

3.2.1. Specimen Preparation for Microcracking Testing

The specimens were cut to their final dimensions using a diamond saw. Glass fibre tabs were adhesively bonded to each end of the specimen to ensure better load introduction. Following this, the edges of the specimens were polished. The polishing process involved using silicon carbide foils with grits of 340, 600, 1000, 2000, and 4000 in succession. The final polishing step utilized an oxide polishing method using a chemically aggressive alkaline colloidal silica suspension. The quality of the polish

Table 3.2: Definition of Specimens Used for Microcracking Testing.

Name	Layup	Heat Treatment	Testing Temperature	Nominal Width	Nominal Length
CR	$[90°/0°/90°/0°/90°/90°]_s$	Yes	22°C -65°C	25 mm	150 mm
CR1	$[0°/90°_2]_s$	Yes	22°C	25 mm	150 mm
CR2	$[0°/90°]_s$	Yes	22°C -65°C	25 mm	150 mm
CR3	$[90°/0°/90°]_T$	Yes	22°C	25 mm	150 mm
CR4	$[0°/90°/0°]_T$	Yes	22°C	25 mm	150 mm

was verified using optical microscopy to ensure that potential cracks would be clearly visible. Prior to loading the specimens, each side was marked to ensure consistent placement in the tensile machine clamps. Additionally, the scanning edge area was marked approximately 1 cm from the end of the tabs to ensure a uniform load distribution within the observed section. The specimen in a microscopy fixture, with markings and the marked observation area, can be seen in Figure 3.4.

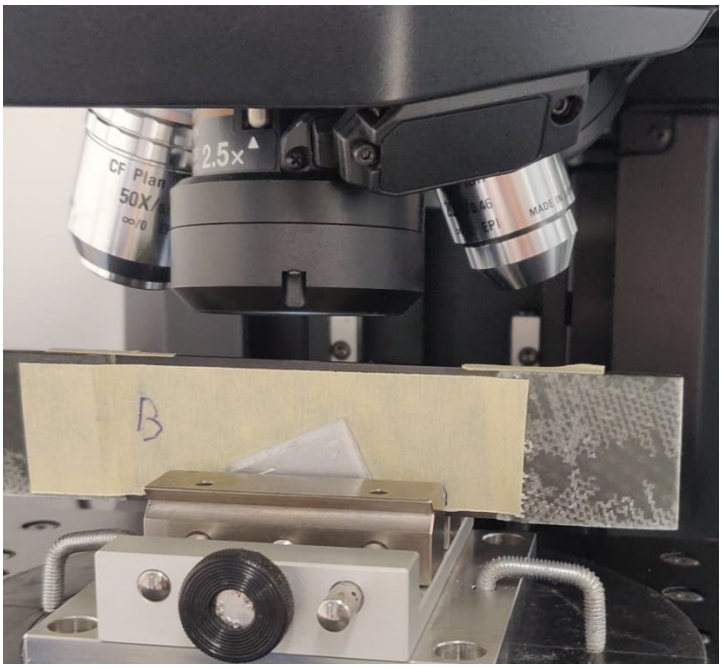

Figure 3.4: Microscopy Test Setup.

3.2.2. Interrupted Quasi-Static Testing

The prepared specimens were loaded into a Zwick 250 kN tensile machine. Hydraulic clamps were used for room temperature tests. However, due to the risk of the hydraulic fluid freezing, manual wedge clamps were employed for cold temperature testing at -65°C. The setup, including the climate chamber and the wedge clamps used for cold temperature testing, can be seen in Figure 3.5. The thermocouple in the picture was connected to the tested specimen to obtain an accurate temperature reading.

The load levels were determined using a straightforward strategy. Initially, a basic first ply stress-based failure criterion was used to identify the applied load at which the 90° plies reached their ultimate tensile stress (S_{22}). The first load amplitude was set at 70% of this calculated load. However, if extensive damage was observed at this load, a lower load was used for subsequent samples in the sample family tested. An illustration of such a load profile is shown in Figure 3.6.

For the cold temperature tests, the residual stress resulting from the difference in testing

temperature (ΔT = 22°C to -65°C) was calculated using CLT, extended to account for thermally induced stress as described in section 4.2. The first test load amplitude for cold temperature tests was chosen such that the sum of the local stress and the residual stress from temperature differences matched the local stress applied in room temperature tests.

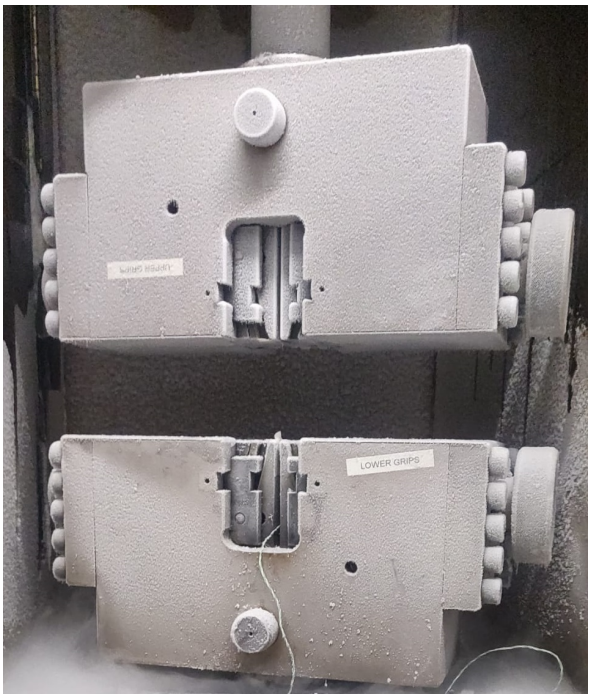

Figure 3.5: Wedge Clamps in the Climate Chamber, Used for Cold Temperature Tensile Testing.

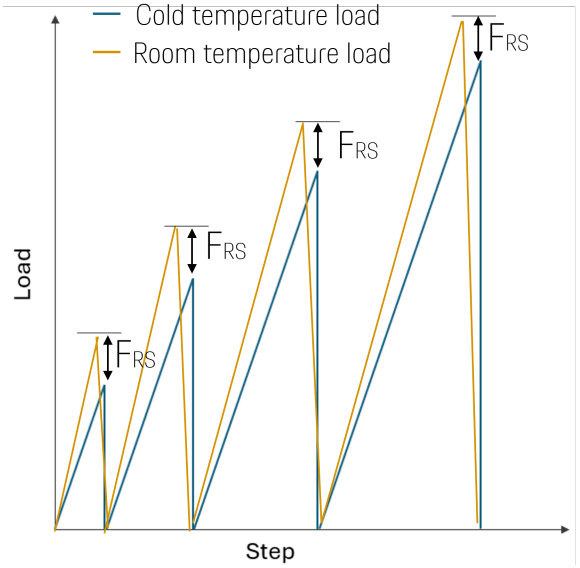

Figure 3.6: Illustration of Interrupted Quasi-Static Loading Profile.

3.2.3. Post-Loading Sample Analysis

After each loading step, the sample was removed from the clamps and placed in the microscopy test fixture, as shown in Figure 3.4. The edges of the sample were cleaned with an acetone cloth before observation. Confocal microscopy at 10x to 20x magnification was then used to collect high-resolution images of the cracks. Although higher magnifications are possible, they may result in the loss of macro features, making 10x to 20x the optimal range for capturing detailed and comprehensive images.

The Keyence VK-X1000 used also allows for laser scanning. The laser beam scans the surface of the sample, focusing to a fine spot that interacts with the surface features. This interaction enhances the contrast between the cracked and uncracked areas, allowing for clearer and more detailed imaging of the cracks.

The microscopy images obtained were processed using ImageJ software [74]. This processing involved measuring the crack length (l_i), and local ply thickness (t_i) to determine the relative crack size. Then the crack density (*CD*) is calculated using Equation 3.9, where l_i is the crack length of the ith crack, t_i is the ply thickness at the ith crack and l_{OA} is the length of the observation area for a given sample as define in Figure 3.1. *N* is the total number of cracks observed in the observation area for a given sample after a given load. This step was crucial in quantifying the extent of microcracking and understanding the distribution and severity of cracks within the specimen.

$$CD = \left[\sum^{N} \frac{l_i}{t_i}\right] / l_{OA} \tag{3.9}$$

More detailed information regarding the microcrack testing methodology can be found in Appendix A, in the CHADA testing template.

3.3. Residual Stress and Temperature Change Experiments

To understand the stresses induced by processing and temperature changes, as well as the effects of heat treatment on these stresses, a series of experiments was conducted. During the experiments, the maximum height of the specimen from the resting plane was measured at different temperatures, ranging from -60°C to 150°C. The specimens used, as defined in Table 3.3, have a non-symmetrical layup, which causes it to naturally curve. This curvature is directly proportional to the residual stresses that would exist if the specimen were symmetrical.

By measuring the curvature, we can quantify and analyse the residual stresses. This approach offers insight into the stress-free temperature of the material. The experimental results also help in assessing how heat treatment can reduce these residual stresses and improve the material's performance. Therefore, one set of measurements was performed on heat-treated samples and another set on untreated samples.

Table 3.3: Definition of Specimen Used for Residual Stress Testing.

Name	Layup	Heat Treatment	Testing Temperature	Nominal width	Nominal length
RS	$[0°/0°/0°/90°/90°/90°]_T$	Yes / No	-60°C to 150°C	15 mm	245 mm

The measured height is equal to the sagitta (*s*) of the circumcircle of the specimen, and the specimen length represents the arc length (*L*) of the circumcircle as shown in Figure 3.7. Then, the curvature κ is defined as:

$$\kappa = \frac{1}{R} \tag{3.10}$$

where R is the radius of the circumcircle. From the Figure 3.7, following can be derived

$$\cos\frac{\theta}{2} = \frac{R-s}{R} \tag{3.11}$$

$$R(1-\cos\frac{L}{2R}) = s \tag{3.12}$$

The Equation 3.12 does not have an explicit solution for the radius of curvature of the circumcircle; therefore, a numerical method is used to determine the radius of curvature *R*. From the radius of curvature (*R*) the curvature (κ) is calculated and compared to the curvature predicted by CLT for a thermal loading of the non-symmetric laminate. The theory behind the thermally induced curvature in the non-symmetric composite plate is further discussed in section 4.2.

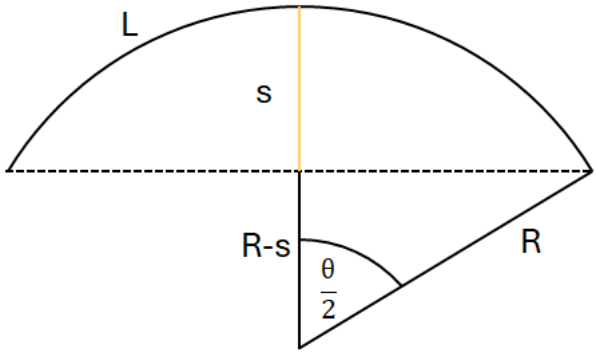

Figure 3.7: Definitions of the Circumcircle Sagitta and the Arc Lenght.

4

Analytical Methodology

This chapter details the analytical models adopted to better understand and characterize microcracking behaviour in the material. The first model, described in section 4.1, makes use of the Halpin-Tsai equations to develop a function of transverse laminate stiffness based on dynamic testing described in subsection 3.1.3. The second model is based on the extended Classical Laminate Theory (CLT). This model is used to determine local stress on ply level and thermally induced residual stresses. Lastly, a statistical model based on the Weibull distribution is developed, which can be adjusted to predict microcracking at various temperatures beyond the test temperature.

4.1. Halpin-Tsain Model for Stiffness Evolution

In order to understand the microcracking of the material at different temperatures, it is necessary to consider evolution of material properties as a function of temperature. Dynamic mechanical tests of the pure matrix material were described in subsection 3.1.3. To derive macromechanical (lamina) properties from these measurements, the Halpin-Tsai model [75] is used. This model provides a more refined estimation of the composite's transverse modulus by considering the properties and volume fractions of the fibres and matrix.

$$E_{22} = E_m \frac{1 + \xi \eta_{22} V_f}{1 - \eta_{22} V_f} \tag{4.1}$$

where E_m is the matrix modulus, obtained from DMA tests as a function of temperature and frequency, V_f is the fibre volume fraction and η_{22} is defined as:

$$\eta_{22} = \frac{(E_f/E_m) - 1}{(E_f/E_m) + \xi} \tag{4.2}$$

where E_f is the fibre stiffness and ξ is a reinforcing factor that depends on fibre geometry, packing geometry, and loading conditions. This parameter is used to fit the model to measured transverse stiffness values from tensile testing at room temperature and at -65°C.

The fibre modulus is assumed to be constant over the range of temperatures. The structure of the composite is also constant, and therefore also the volume fractions stay also constant.

4.2. Lamina Stresses due to Applied Load and Temperature

In order to combine tests of different layups, it is important to know the stress in each ply and in the local direction. The Classical Lamination Theory is used for this purpose. As the residual stresses are also considered, the Theory was extended to include thermally induced residual stresses.

4.2.1. Theoretical Background of CLT

The displacement field in the Theory is restrained by the Kirchhoff hypothesis. Therefore, each panel is treated as an infinite 2D plate, representing the midplane of the physical plate. The midplane is capable of simple translation and rotation. The displacement of any point is given as [76]:

$$\begin{aligned} u(x,y,z) &= u^0(x,y) - z\frac{\partial w^0(x,y)}{\partial x} \\ v(x,y,z) &= v^0(x,y) - z\frac{\partial w^0(x,y)}{\partial y} \\ w(x,y,z) &= w^0(x,y) \end{aligned} \tag{4.3}$$

where u^0, v^0 and w^0 are displacements of the midplane and *z* is the distance from the midplane in the thickness direction. From the Equation 4.3, it can be seen that in-plane displacements vary linearly with *z* everywhere in the plate.

The strain ϵ is defined as:

$$\begin{aligned} \varepsilon_x(x,y,z) &= \varepsilon_x^0(x,y) + z\kappa_x^0(x,y) \\ \varepsilon_y(x,y,z) &= \varepsilon_y^0(x,y) + z\kappa_y^0(x,y) \\ \gamma_{xy}(x,y,z) &= \gamma_{xy}^0(x,y) + z\kappa_{xy}^0(x,y) \end{aligned} \tag{4.4}$$

where the midplane strain and curvature are defined as:

$$\begin{aligned} \varepsilon_x^0(x,y) &= \frac{\partial u^0(x,y)}{\partial x} \quad \text{and} \quad \kappa_x^0(x,y) = -\frac{\partial^2 w^0(x,y)}{\partial x^2} \\ \varepsilon_y^0(x,y) &= \frac{\partial v^0(x,y)}{\partial y} \quad \text{and} \quad \kappa_y^0(x,y) = -\frac{\partial^2 w^0(x,y)}{\partial y^2} \\ \gamma_{xy}^0(x,y) &= \frac{\partial v^0(x,y)}{\partial x} + \frac{\partial u^0(x,y)}{\partial y} \text{ and } \kappa_{xy}^0 = -2\frac{\partial^2 w^0(x,y)}{\partial x \partial y} \end{aligned} \tag{4.5}$$

The stress in each lamina of the stack can be determined using Equation 4.6, where the $\bar{Q}$ matrix is the rotated compliance matrix of each lamina. This matrix is constructed using the elastic properties of the material, see [76] for more details.

$$\begin{Bmatrix} \sigma_x \\ \sigma_y \\ \tau_{xy} \end{Bmatrix} = \begin{bmatrix} \bar{Q}_{11} & \bar{Q}_{12} & \bar{Q}_{16} \\ \bar{Q}_{12} & \bar{Q}_{22} & \bar{Q}_{26} \\ \bar{Q}_{16} & \bar{Q}_{26} & \bar{Q}_{66} \end{bmatrix} \begin{Bmatrix} \varepsilon_x^o + z\kappa_x^o \\ \varepsilon_y^o + z\kappa_x^o \\ \gamma_{xy}^o + z\kappa_{xy}^o \end{Bmatrix} \tag{4.6}$$

Equation 4.6 is used in the analysis of residual stress experiments. At multiple temperatures, the curvature is measured, which is a direct result of the residual stresses alone, as no load is applied to the specimens. The residual stress is calculated from the known curvature, therefore, the curvature of the specimens is proportional to the residual stress.

The stress distribution across the thickness of the laminate can be integrated to obtain the force and moment resultants. These resultants provide a macroscopic description of the laminate's behaviour. The force resultants are the in-plane forces per unit length, while the moment resultants are the bending and twisting moments per unit length. They are defined as:

$$\begin{aligned} N_x &\equiv \int_{-\frac{H}{2}}^{\frac{H}{2}} \sigma_x dz \qquad M_x \equiv \int_{-\frac{H}{2}}^{\frac{H}{2}} \sigma_x z dz \\ N_y &\equiv \int_{-\frac{H}{2}}^{\frac{H}{2}} \sigma_y dz \qquad M_y \equiv \int_{-\frac{H}{2}}^{\frac{H}{2}} \sigma_y z dz \\ N_{xy} &\equiv \int_{-\frac{H}{2}}^{\frac{H}{2}} \tau_{xy} dz \qquad M_{xy} \equiv \int_{-\frac{H}{2}}^{\frac{H}{2}} \tau_{xy} z dz \end{aligned} \tag{4.7}$$

The ABD matrix consolidates the extensional (*A*), coupling (*B*), and bending (*C*) stiffness properties of the laminate into a single matrix. The relationship between the force and moment resultants and the midplane strains (ϵ_x^0, ϵ_y^0, γ_{xy}^0) and curvatures (κ_x^0, κ_y^0,κ_{xy}^0) is given by:

$$\begin{Bmatrix} N_x \\ N_y \\ N_{xy} \\ M_x \\ M_y \\ M_{xy} \end{Bmatrix} = \begin{bmatrix} A_{11} & A_{12} & A_{16} & B_{11} & B_{12} & B_{16} \\ A_{12} & A_{22} & A_{26} & B_{12} & B_{22} & B_{26} \\ A_{16} & A_{26} & A_{66} & B_{16} & B_{26} & B_{66} \\ B_{11} & B_{12} & B_{16} & D_{11} & D_{12} & D_{16} \\ B_{12} & B_{22} & B_{26} & D_{12} & D_{22} & D_{26} \\ B_{16} & B_{26} & B_{66} & D_{16} & D_{26} & D_{66} \end{bmatrix} \begin{Bmatrix} \varepsilon_x^o \\ \varepsilon_y^o \\ \gamma_{xy}^o \\ \kappa_x^o \\ \kappa_y^o \\ \kappa_{xy}^o \end{Bmatrix} \tag{4.8}$$

4.2.2. Thermally Induced Stress

In Classical Laminate Theory (CLT), thermally induced stresses arise due to differences in thermal expansion properties between the plies of a composite laminate. When a laminate is subjected to a temperature change (ΔT), each lamina attempts to expand or contract according to its own coefficient of thermal expansion (CTE). However, because the plies are bonded together, they are constrained by each other, leading to internal stresses. The mismatch in CTEs between the different plies results in these thermally induced stresses. The thermal force and moment resultant due to a temperature change ΔT is given by [76]:

$$\begin{aligned}
N_x^T &= \sum_{k=1}^{N} \left(\bar{Q}_{11_k}\alpha_{x_k} + \bar{Q}_{12_k}\alpha_{y_k} + \bar{Q}_{16_k}\alpha_{xy_k}\right)(z_k - z_{k-1})\,\Delta T \\
N_y^T &= \sum_{k=1}^{N} \left(\bar{Q}_{12_k}\alpha_{x_k} + \bar{Q}_{22_k}\alpha_{y_k} + \bar{Q}_{26_k}\alpha_{xy_k}\right)(z_k - z_{k-1})\,\Delta T \\
N_{xy}^T &= \sum_{k=1}^{N} \left(\bar{Q}_{16_k}\alpha_{x_k} + \bar{Q}_{26_k}\alpha_{y_k} + \bar{Q}_{66_k}\alpha_{xy_k}\right)(z_k - z_{k-1})\,\Delta T \\
M_x^T &= \frac{1}{2}\sum_{k=1}^{N} \left(\bar{Q}_{11_k}\alpha_{x_k} + \bar{Q}_{12_k}\alpha_{y_k} + \bar{Q}_{16_k}\alpha_{xy_k}\right)\left(z_k^2 - z_{k-1}^2\right)\Delta T \\
M_y^T &= \frac{1}{2}\sum_{k=1}^{N} \left(\bar{Q}_{12_k}\alpha_{x_k} + \bar{Q}_{22_k}\alpha_{y_k} + \bar{Q}_{26_k}\alpha_{xy_k}\right)\left(z_k^2 - z_{k-1}^2\right)\Delta T \\
M_{xy}^T &= \frac{1}{2}\sum_{k=1}^{N} \left(\bar{Q}_{16_k}\alpha_{x_k} + \bar{Q}_{26_k}\alpha_{y_k} + \bar{Q}_{66_k}\alpha_{xy_k}\right)\left(z_k^2 - z_{k-1}^2\right)\Delta T
\end{aligned} \tag{4.9}$$

where *k* is subscript for each lamina in the laminate, *z* is the distance of the lamina to the midplane, and the off-axis Coefficient of Thermal Expansion for each ply is calculated as:

$$\begin{aligned}
\alpha_x &= \alpha_1 \cos^2\theta + \alpha_2 \sin^2\theta \\
\alpha_y &= \alpha_1 \sin^2\theta + \alpha_2 \cos^2\theta \\
\alpha_{xy} &= 2\left(\alpha_1 - \alpha_2\right)\cos\theta \sin\theta
\end{aligned} \tag{4.10}$$

The global thermal strains and curvatures are obtained by multiplying the thermal force and moment resultant with the *abd* matrix, which is the inverse of the *ABD* matrix described in Equation 4.8. In the case of a non-symmetrical layup, the free thermal response is particularly interesting because it involves both reference surface curvatures and in-plane surface strains when the temperature is altered.

The local thermal residual stress for each ply is calculated by taking the global thermal strains and curvatures, rotating them to the local coordinate system, and multiplying them with the lamina compliance matrix *Q*, as described in Equation 4.6. As mentioned before, this process can be reversed: by measuring the curvature of non-symmetrical layups over a range of temperatures, the residual stress can be calculated from that data. This approach provides a strategy for validating the residual stress model used.

By incorporating thermal effects, CLT can predict the additional stresses and deformations due to temperature changes, providing a more comprehensive model for analysis of laminate behaviour over a range of temperatures. This model enables a comparison of microcracking performance at room temperature with that at low temperature (-65°C) by considering residual stresses.

4.2.3. CLT and Temperature Dependence of Material Properties

The thermally induced stress is a function of temperature and certain material parameters, specifically the rotated stiffness matrix ($\bar{Q}$) and the thermal expansion coefficients (α). Importantly, both the elastic material properties, which are encapsulated in the $\bar{Q}$ matrix, and the thermal properties (α) are also functions of temperature.

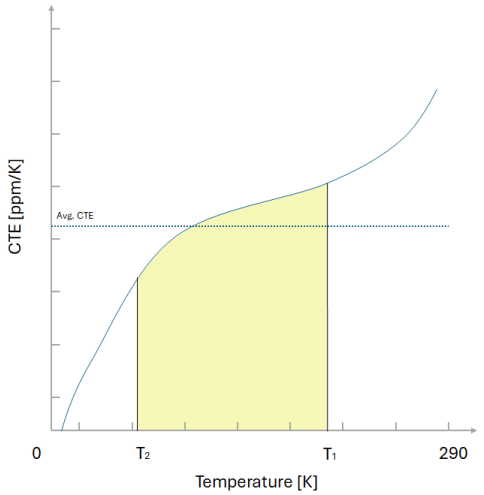

Figure 4.1: Illustration of CTE Evolution Trends, Demonstrating the Methodology for Calculating Average CTE for Residual Stress Analysis.

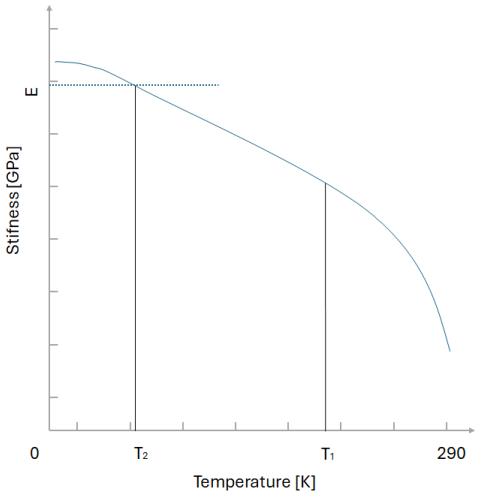

Figure 4.2: Illustration of Stiffness Evolution Trends, Demonstrating the Methodology for Determining Stiffness for Residual Stress Analysis.

Figure 4.1 and Figure 4.2 show the expected trends of CTE and stiffness evolution respectively between the cryo temperature and the glass transition temperature of a thermoplastic composite. For the residual stress calculation, going from temperature T_1 to a lower temperature T_2, the CTE and the stiffness are calculated as follows:

$$\alpha_{RS} = \frac{\int_{T_1}^{T_2} \alpha(T) \partial T}{T_1 - T_2} \tag{4.11}$$

$$E_{RS} = E(T_2) \tag{4.12}$$

As can be seen in Equation 4.11, an average coefficient of thermal expansion α is calculated between the two temperatures of interest and subsequently applied in Equation 4.10.

For the elastic values, the stiffness is calculated at the temperature where residual stress is used, as shown in Equation 4.12.

4.3. Weibull Statistical Model of Microcracking

The Weibull statistical model is an effective tool for modelling the microcracking behaviour of thermoplastic composites by treating transverse strength as a statistical parameter. The justification for using this model lies in the inherent statistical variability present in the microstructure of composites, along with the existence of intrinsic flaws [39].

In composite materials, the microstructure is not perfectly uniform; there are variations in fibre distribution, matrix properties, and the presence of defects such as voids or microvoids. An example of such a region with a matrix crack can be seen in Figure 4.3. These variations lead to statistical differences in the transverse ply strength, meaning that different regions within the composite will exhibit different strengths. Consequently, the Weibull model accounts for these variations by providing a probabilistic description of the strength distribution across the material.

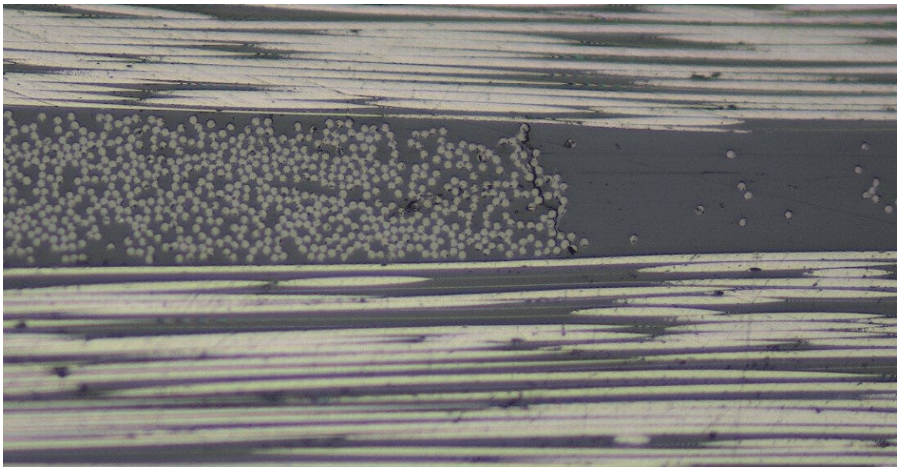

Figure 4.3: Crack at Region of Lower Local Ply Strength due to Ply Waviness.

In this section, a mathematical definition of the Weibull distribution, explaining the meaning and role of its parameters. Following that, the methodology used to determine the model parameters from observed microcracking data is outlined. Finally, the concept of temperature induced residual stress and its implications are discussed.

4.3.1. Weibull Distribution

Microcracking typically initiates in regions where the local strength is reduced. Such regions may include areas with local ply deformation, higher matrix volume fractions, or other stress concentrators. The Weibull model's ability to describe the distribution of strength across these regions makes it particularly suitable for predicting the onset of microcracking. By treating transverse strength statistically, the model can effectively capture the likelihood of microcrack formation in different areas of the composite. This is done by using a cumulative distribution function (CDF) of the Weibull distribution, defined as:

$$F(\sigma) = 1 - \exp\left[-\left(\frac{\sigma}{\sigma_0}\right)^m\right] \tag{4.13}$$

where σ is the ply stress, σ_0 is the average strength of the ply and *m* is the model shape parameter. As material failure is an accumulative process, the CDF inherently captures this by accumulating probabilities up to a given value.

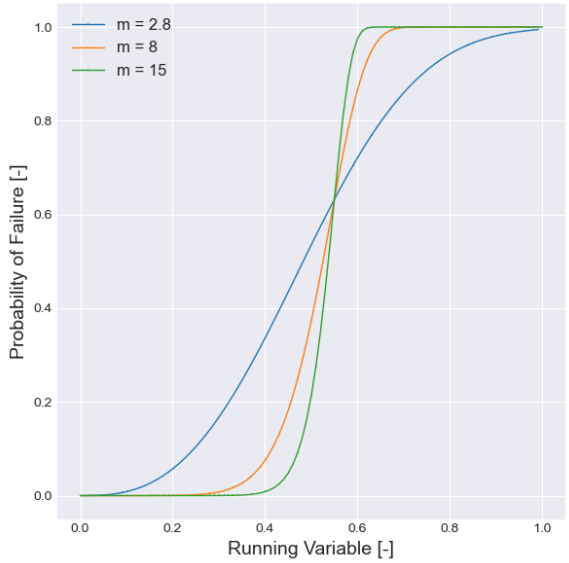

Figure 4.4: Generic CDF of Weibull Distribution with Varying Shape Parameter m and σ_0 = 0.55

4.3.2. Model Parameters

Experimental data can be fitted by adjusting the Weibull scale (σ_0), and shape (m) parameters. For most sample families, three different samples were tested within a similar range of local stress. Due to the inherent probabilistic and discontinuous behaviour of microcracking, it often occurs that a crack develops in one sample at a specific stress level, while the other two samples do not show any cracks at the same stress level. This results in three different sets of shape and strength model parameters for each sample set.

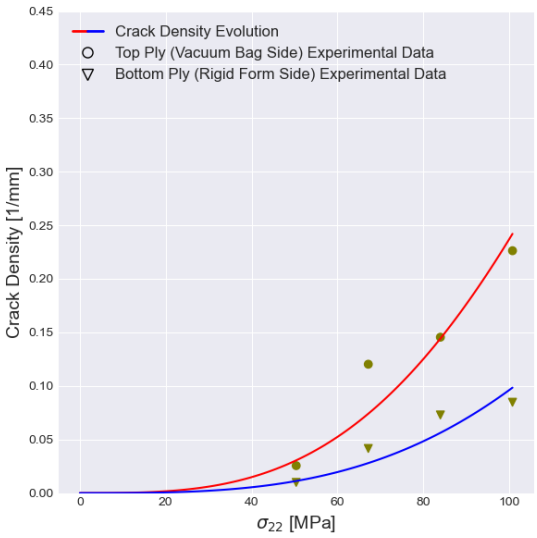

Figure 4.5: Visualization of Finding a Strength for Each Ply Tested.

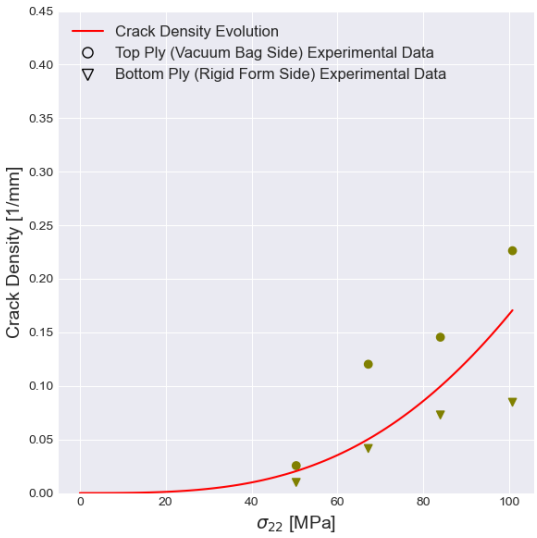

Figure 4.6: Visualization of Plotting an Average Strength of Each Sample Family.

To streamline this, a shape parameter is first fitted to the results of the entire sample family. Then, an optimal strength parameter is determined for each individual ply set. The final parameters for the whole sample family are the common shape parameter and the average of the strength parameters from each sample.

To visualize this process, two different plies are shown in Figure 4.5 and Figure 4.6. In these figures, the experimental values for one ply are plotted using circle scatter markers, while the values for a different ply of the same type are plotted using triangle scatter markers. Once a suitable shape parameter is determined, fitting both sets of data, the Weibull distribution with this shape parameter is used to find the optimum strength parameter for each ply. The resulting fitted curves, shown in red and blue, are depicted in Figure 4.5.Subsequently, the average strength value is calculated, and a final curve representing the entire sample family is plotted in Figure 4.6.

4.3.3. Temperature Shift

Given the model parameters and residual stress, it is possible to shift the resulting microcracking curve from one temperature to another. If the microcracking test is performed at temperature T_1, and it is necessary to approximate the microcracking behaviour of the material at temperature T_2, and if it is possible to obtain elastic and thermal parameters between the T_1 and T_2, the shift is performed as follows:

$$F(\sigma_{22_2}, T_2) = 1 - \exp\left[-\left(\frac{\sigma_{22_2} + \sigma_{RS_{12}}}{\sigma_{0_1}}\right)^{m_1}\right] \tag{4.14}$$

where F is the probability of material failure at local stress σ_{22_2} at temperature T_2, $\sigma_{RS_{12}}$ is the residual stress calculated between temperature T_1 and T_2, as explained in section 4.2, and the model parameters σ_{0_1} and m_1 are determined from the test at temperature T_1. An example of such a shift given experimental data and residual stress can be seen in Figure 4.7.

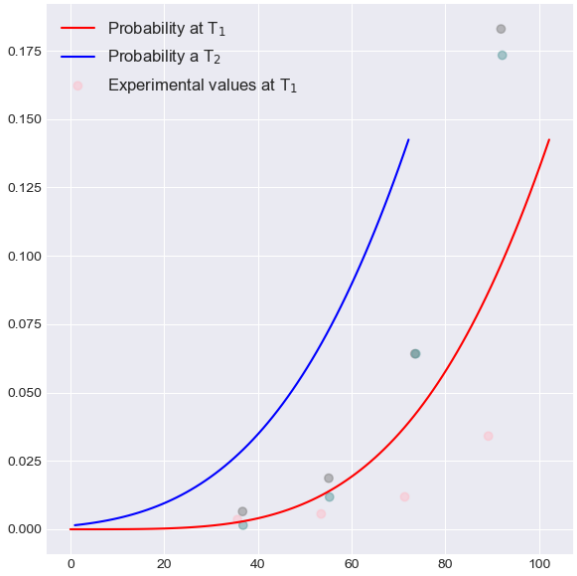

Figure 4.7: Illustration of the Temperature Shift from T_1 to T_2.

The proposed shifting of microcracking curves considers mesoscale residual stresses in the composite and changes in both the elastic and thermal properties of the material. However, it does not account for the potential reduction in matrix ductility, which leads to lower energy absorption and an expected acceleration of crack growth.

5 Results

This chapter presents the results obtained from the studies described in chapter 3 and chapter 4. The experiments were designed to characterize the material properties and to evaluate the microcracking behaviour of the specimens at various temperatures. The results are systematically categorized into three main sections: Material Characterization, Microcracking, and Residual Stresses. Each section provides a detailed insight into the respective aspects of the found results.

5.1. Characterization of Lamina Properties

In this section, the intrinsic properties of the material are characterized through tensile tests. The subsections detail the methods and results used to determine ply thickness, tensile elastic properties, and dynamic properties.

5.1.1. Ply Thickness Measurement

An accurate average thickness value is necessary for Classical Laminate Theory, discussed in section 4.2. A total of 12 different panels were measured at a minimum of six different locations within each panel. Each measurement is plotted in Figure 5.1, and the distribution is shown in Figure 5.2. The average ply thickness was found to be 0.1349 mm, with a standard deviation of 0.00678 mm.

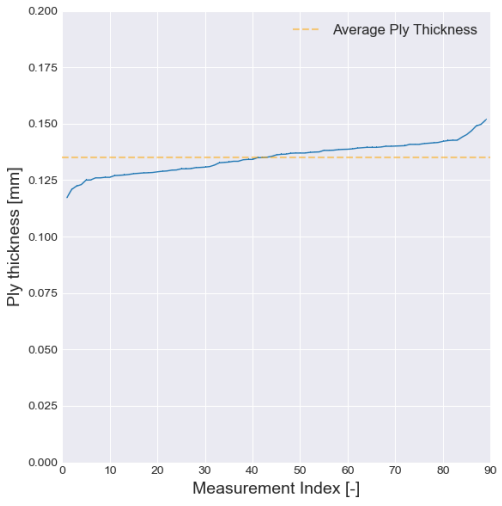

Figure 5.1: Measured Ply Thickness Across Different Samples.

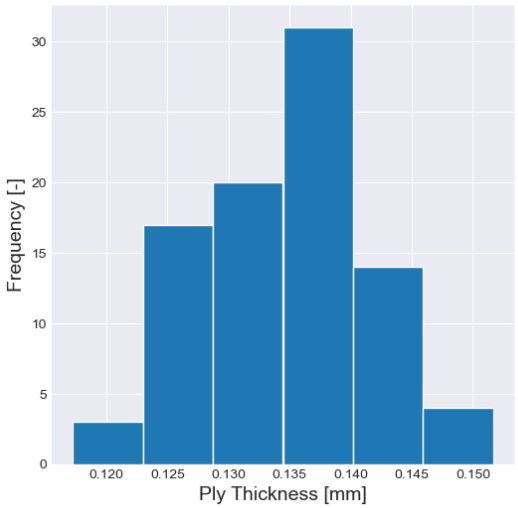

Figure 5.2: Distribution of Measured Ply Thickness.

5.1.2. Tensile Elastic Properties

The elastic constants of carbon-fibre composite material, considered to be orthotropic, are defined as:

- **Longitudinal Stiffness Modulus** - response to axial deformation aligned with the fibre direction
- **Transverse Stiffness Modulus** - response to axial deformation perpendicular to the fibres within the plane of the laminate
- **In-plane Shear Modulus** - response to shear deformation in the plane formed by the longitudinal and transverse directions
- **Major Poisson's Ratio** - coupling between normal strains in transverse strain and axial strain direction

Longitudinal Young's Modulus (E_{11})

The longitudinal Young's modulus, E_{11}, measures the stiffness of the composite in the direction parallel to the fibres, which is typically the strongest and stiffest due to the fibre alignment.

Figure 5.3 and Figure 5.4 display the strain response to the applied stress at room and cold temperatures (-65°C), respectively. As expected, the curves are linear until failure, and their slopes represent the Young's modulus of the material, E_{11}.

In the room temperature tests, two different data acquisition sensors were used for strain measurement: an extensometer with a 50 mm gauge length and an attached strain gauge with a 2 mm gauge length. As shown in Table 5.1, these different measurement techniques resulted in slightly different moduli. This discrepancy may be due to a systematic error in one of the measurements or a large spatial variation in the material's stiffness. Since the source of this difference is unknown, both measurements are retained.

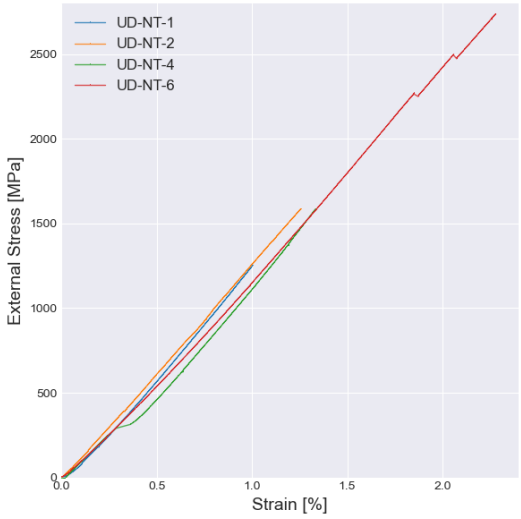

Figure 5.3: Stress-Strain Curve for TC1225/T800 at Room Temperature.

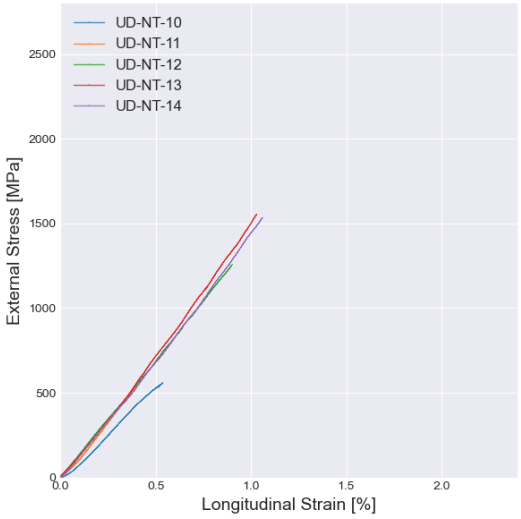

Figure 5.4: Stress-Strain Curve for TC1225/T800 at Cold Temperature.

Table 5.1: Test Results of Unidirectional Specimens at Room Temperature.

Specimen Label	Average Width [mm]	Average Thickness [mm]	Modulus Strain Gauge [GPa]	Modulus Extensometer [GPa]	Poisson's Ratio [-]	Ultimate Tensile Stress [MPa]
UD-NT-1	18.35	0.87	-	136	-	3143.1
UD-NT-2	17.75	0.89	140	133	0.36	2662.1
UD-NT-4	17.93	0.86	140	133	0.42	2405.8
UD-NT-6	17.55	0.83	143	134	0.33	2757.9
Mean				137.4	0.37	2742.3
Standard Deviation				4.3	0.05	305.8

The cold temperature tests of the unidirectional specimens in Table 5.2 used only the strain gauge for strain data acquisition. The results show considerable scatter in the moduli between samples, with the mean modulus being slightly higher than in the room temperature tests. Ultimate tensile stress data marked with an asterisk did not result in material failure and are therefore excluded from the mean value calculation. These samples experienced clamp slippage issues and were not reloaded, as the extent of damage after the initial loading could not be accurately assessed.

Table 5.2: Test Results of Unidirectional Specimens at Cold (-65°C) Temperature.

Specimen Label	Average Width [mm]	Average Thickness [mm]	Modulus Strain Gauge [GPa]	Ultimate Tensile Stress [MPa]
UD-NT-10	14.93	0.82	124	555.7*
UD-NT-11	14.56	0.83	160	535.6*
UD-NT-12	15.36	0.84	138	1254.1
UD-NT-13	15.07	0.84	157	1689.3
UD-NT-14	19.73	0.87	138	2625.4
	Mean		143	1856.3
	Standard Deviation		15.2	700.7

Transverse Young's Modulus (E_{22})

The transverse Young's modulus, E_{22}, is another crucial parameter in the characterization of the elastic properties of carbon fibre composites. Unlike the longitudinal Young's modulus (E_{11}), which measures stiffness parallel to the fibres, E_{22} quantifies the stiffness perpendicular to the fibre direction. This modulus is typically lower than E_{11} due to the matrix material's dominance in this direction.

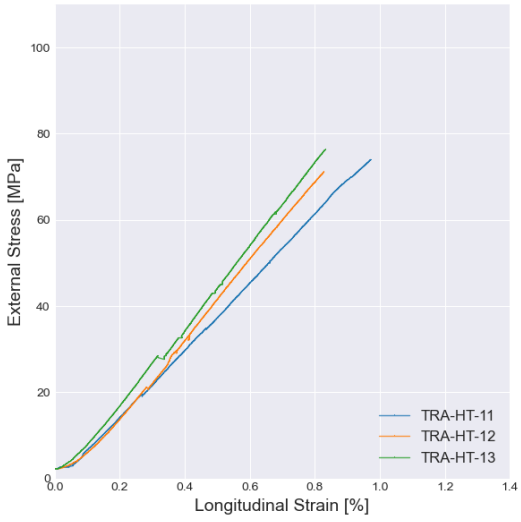

Figure 5.5: Stress-Strain Curve for TC1225/T800 at Room Temperature.

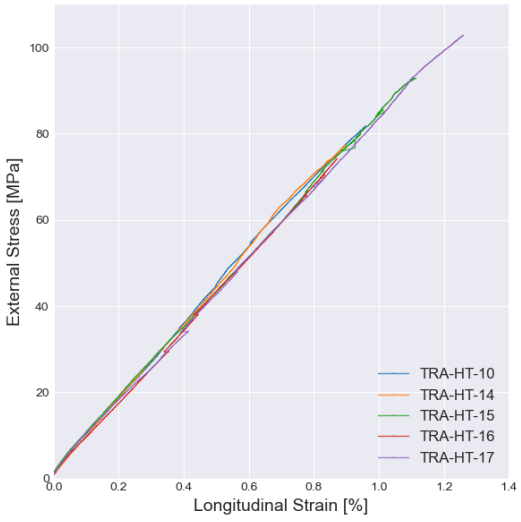

Figure 5.6: Stress-Strain Curve for TC1225/T800 at Cold Temperature.

Table 5.3: Test Results of Transverse Specimens at Room Temperature.

Specimen Label	Average Width [mm]	Average Thickness [mm]	Modulus Strain Gauge [GPa]	Ultimate Tensile Stress [MPa]
TRA-HT-11	26.91	0.87	7.9	94.00
TRA-HT-12	27.09	0.87	9.2	81.45
TRA-HT-13	26.50	0.86	9.9	80.18
Mean			9.0	85.21
Standard Deviation			1.03	7.64

The test results at room temperature are presented in Table 5.3, and for cold temperature in Table 5.4, graphically in Figure 5.5 and Figure 5.6 respectively. An increase in transverse Young's modulus is observed in the cold temperature samples, while the ultimate tensile stress, S_{22} remains unchanged at both temperatures.

Table 5.4: Test Results of Transverse Specimens at Cold (-65°C) Temperature.

Specimen Label	Average Width [mm]	Average Thickness [mm]	Modulus Strain Gauge [GPa]	Ultimate Tensile Stress [MPa]
TRA-HT-10	25.32	0.86	10.8	81.76
TRA-HT-14	24.52	0.85	9.5	84.26
TRA-HT-15	26.37	0.87	11.1	93.84
TRA-HT-16	27.19	0.86	10.0	73.98
TRA-HT-17	27.14	0.87	11.6	102.78
Mean			10.6	87.12
Standard Deviation			0.82	11.04

Shear Modulus (G_{12})

The shear modulus, G_{12}, is a fundamental parameter in characterising the mechanical properties of carbon fibre composites. It represents the material's response to shear deformation in the plane defined by the longitudinal and transverse directions.

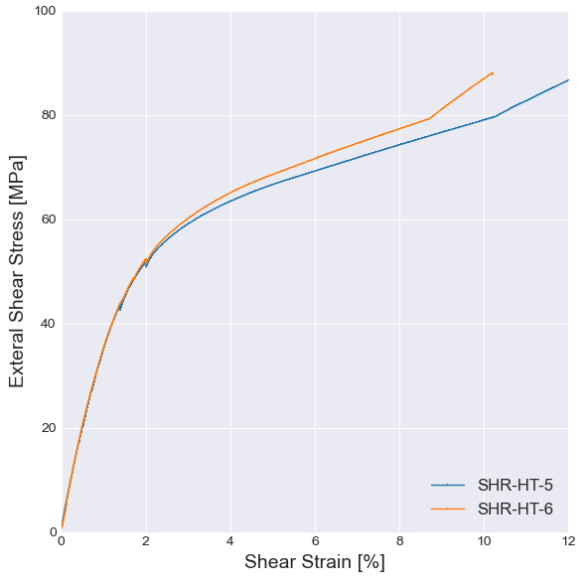

Figure 5.7: Shear Stress-Strain Curve for TC1225/T800 at Room Temperature.

The Figure 5.7 shows a typical shear stress-strain curve for a polymer composite material with a ductile matrix, characterized by approximately two bilinear regions. It can be observed that a third, slightly stiffer region appears after the second linear region. However, for the determination of G_{12}, only the initial linear part is considered, as its slope represents the shear modulus. The results for room temperature can be seen in Table 5.5.

Table 5.5: Test Results of Shear Specimens at Room Temperature.

Specimen Label	Average Width [mm]	Average Thickness [mm]	Shear Modulus Strain Gauge [GPa]	Ultimate Shear Stress [MPa]
SHR-HT-5	26.54	1.61	3.6	113.86
SHR-NT-6	27.22	1.67	3.8	87.77
Mean			3.7	100.82
Standard Deviation			0.12	18.44

Major Poisson's Ratio (ν_{12})

The major Poisson's ratio, ν_{12}, is an essential parameter in the study of the mechanical properties of carbon fibre composites. It describes the ratio of transverse strain to axial strain when the composite is subjected to uniaxial stress in the longitudinal direction. Specifically, ν_{12} measures how much the material contracts in the transverse direction when it is stretched in the longitudinal direction.

As can be seen in Figure 5.8, the transverse strain is negative and of lower magnitude than the strain along the loading direction, which was aligned with the fibres. This trend is expected from the material's Poisson effect. The slope of the transverse contraction shows scatter of unknown origin, which may be attributed to experimental inconsistencies or material heterogeneity. Despite this scatter, the overall value is consistent with that published in the TC1225 technical data sheet [77]. As the Poisson's ratio was calculated from the same experiments as the longitudinal Young's modulus, the final results are summarised in Table 5.1.

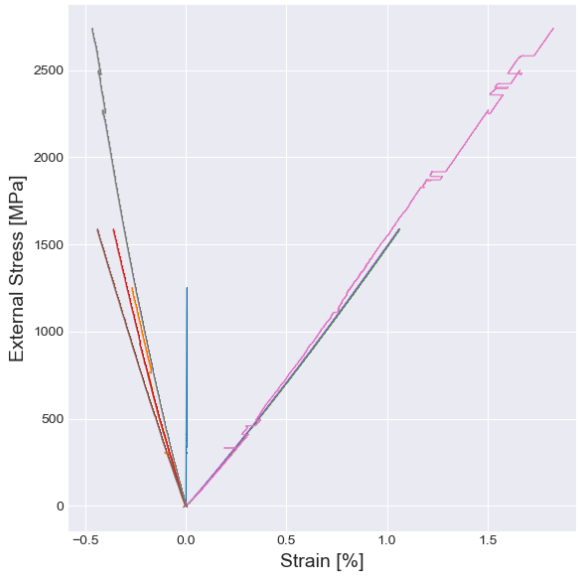

Figure 5.8: Stress-Strain Curve for TC1225/T800 at Room Temperature, Including Longitudinal and Transverse Strains.

5.1.3. Dynamic Mechanical Properties

The frequency sweeps for each temperature are shown in Figure 5.9. Temperatures are incremented in 10°C steps, ranging from -150°C to 130°C, with warmer temperatures depicted in warmer colours. The

dynamic mechanical tensile testing of the matrix material shows a clear increase in stiffness across the entire frequency range as temperature decreases. However, there are noisy regions at low frequencies, highlighting the limitations of the DMA machine.

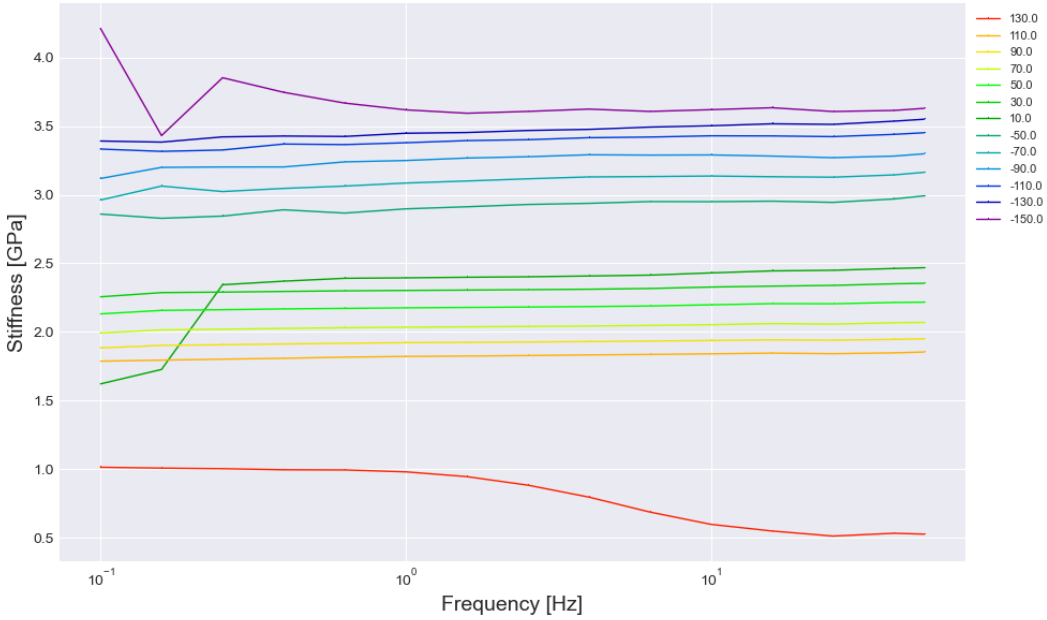

Figure 5.9: DMA Testing over a Frequency Range from 0.1Hz to 100Hz and a Temperature Range from 130°C to -150°C.

To better visualize the increase in stiffness with decreasing temperature, the stiffness at 0.25 Hz is plotted against temperature in Figure 5.10. Although this data lies within the previously mentioned noisy region, it is selected because it best represents the quasi-static nature of the tensile test on the composite mentioned above. Consequently, the same trend of matrix stiffening with decreasing temperature is confirmed. The trend seems to follow a linear pattern, as indicated by the dashed line.

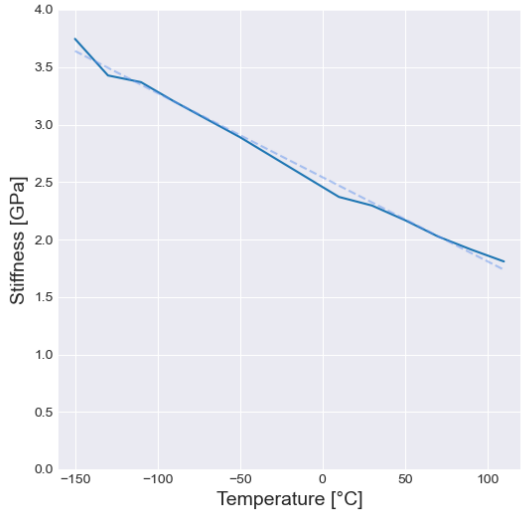

Figure 5.10: Victrex AE™ 250 LM-PAEK Stiffness Evolution at 0.25 Hz Frequency between 110°C and -150°C.

5.1.4. Lamina Transverse Stiffness Function

Dynamic properties of the matrix material were obtained across a range of temperatures and translated into a quasi-static transverse modulus of the lamina using the model described in section 4.1. Volume fractions and fibre stiffness were sourced from the material's data sheet. To fit the model parameter ξ, measured transverse moduli of the lamina at room temperature and -65°C were used, as detailed in subsection 5.1.2.

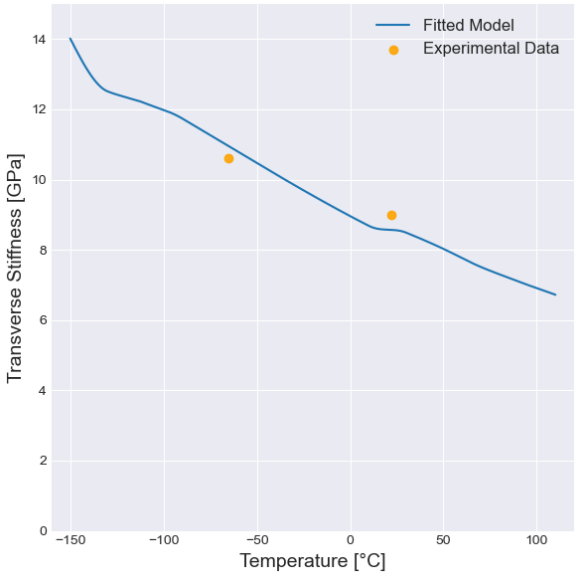

Figure 5.11: Evolution of Lamina Transverse Stiffness Based on Matrix Stiffness Evolution.

The model exhibits an almost linear behaviour across most of its range, which aligns with the matrix stiffness trend observed in the DMA test. This model can only be constructed within the temperature range of the dynamic mechanical testing. However, its validity cannot be confirmed below -65°C. Data from the COCOLIH2T consortium highlight this limitation, showing that the lamina transverse stiffness at cryogenic temperatures (-253°C) is lower than the model's prediction even at -100°C.

5.2. Microcracking Behaviour Analysis

This section examines the microcracking behaviour of TC1225/T800, focusing on crack density as a function of local stress in the transverse ply. It includes room temperature testing, where the relationship between local stress and crack density is highlighted with supporting graphs. This is followed by low-temperature testing at -65°C, analysis of stress-induced crack density trends under low-temperature conditions, and finally visualization, visualization of the cracks using computed tomography (CT) scans to reveal internal microcrack patterns.

5.2.1. Room Temperature Microcracking Testing

As previously shown in Table 3.2, five different cross-ply layups were tested at room temperature. Layups CR1, CR2, and CR4 have stacking sequence $[0/90_n]_s$ where *n* is 4, 2, and 1 respectively. The results for these sample families consist of one graph that plots the crack density of the middle ply block against the local stress of the 90° ply. The sample family CR has outside 90° plies, two inner 1x 90° plies, and one block of 4x 90° plies; therefore, the results for this sample family consist of three graphs. The sample family CR3 has 90° plies on the outside and one 0° ply in the middle.

Compounded layup of three different ply types - CR

For all specimens of CR layups, the outer 90° plies showed the highest crack densities at a given load. The figure Figure 5.12 shows two different model fits: one for the ply on the vacuum bag side and one for the form side of the laminate. It was found that the vacuum bag side cracks more easily for this set of samples.

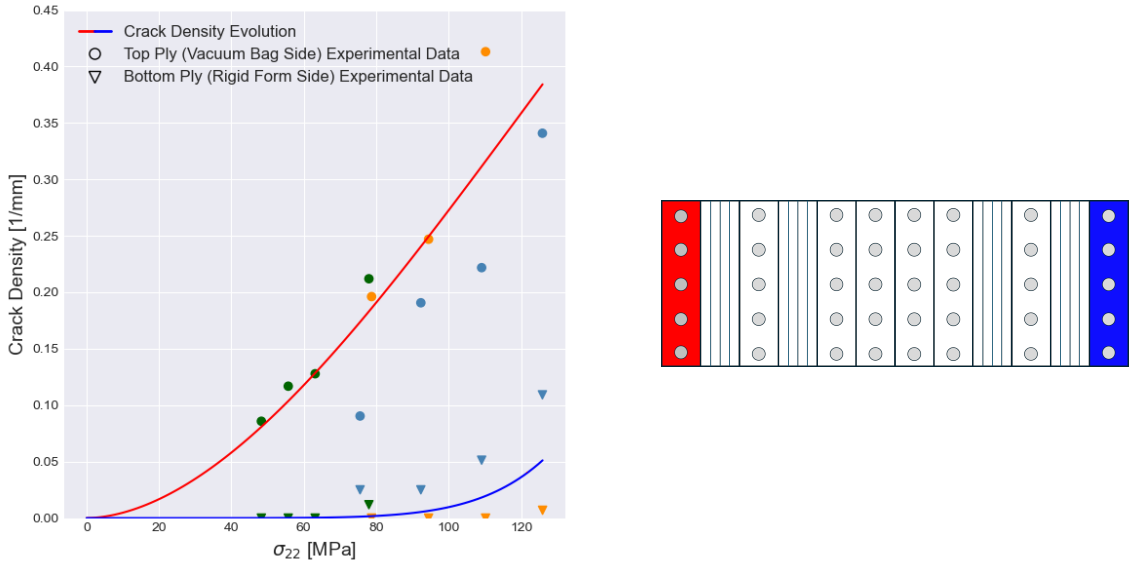

Figure 5.12: Stress-Induced Crack Density in Outer 90° Plies of CR Layup Family at Room Temperature.

Figure 5.13 illustrates the crack density evolution for two symmetrically placed 1x 90° plies in the layup. Since there was no reason to expect one ply to crack more easily than the other, the results for both plies were combined into a single plot. The experimental data points for each ply are distinguished by different marker types. Figure 5.14 shows the crack evolution of the middle ply block, consisting of four 90° plies. Due to the cumulative nature of microcracking, it is evident that even if a crack is observed at lower load levels with little to no further evolution in crack density at higher loads, it significantly influences the final model fit. This confirms that microcracking prediction is heavily influenced by the inherent randomness of crack nucleation. There is always some probability that cracks can develop even at unexpectedly low load levels. Note that the scale of the graph for the crack density of the outside plies is different from that of all the inner plies graphs.

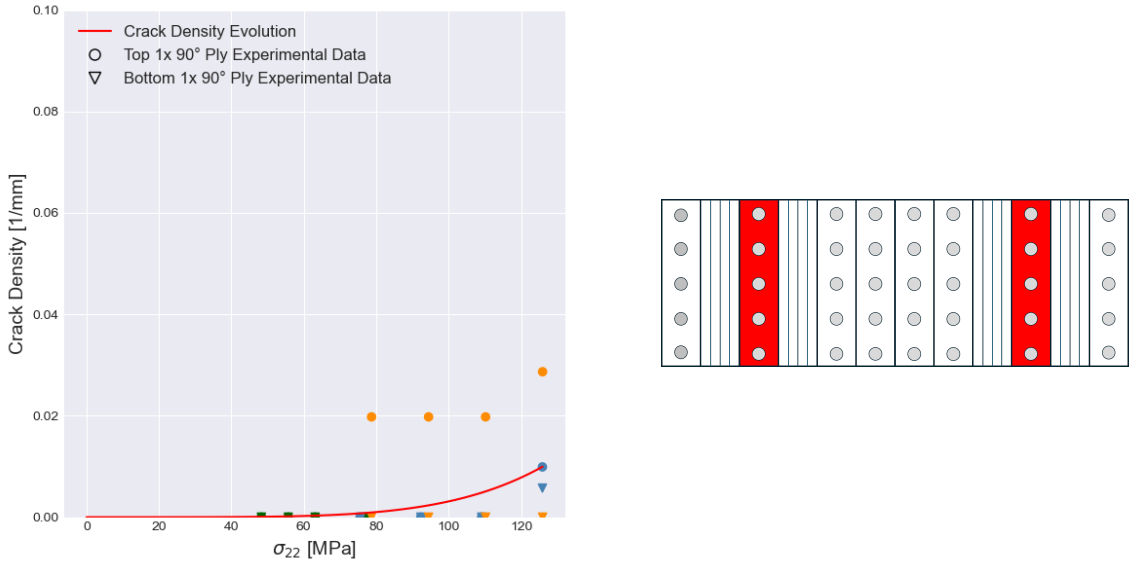

Figure 5.13: Stress-Induced Crack Density in 90° Plies of CR Layup Family at Room Temperature.

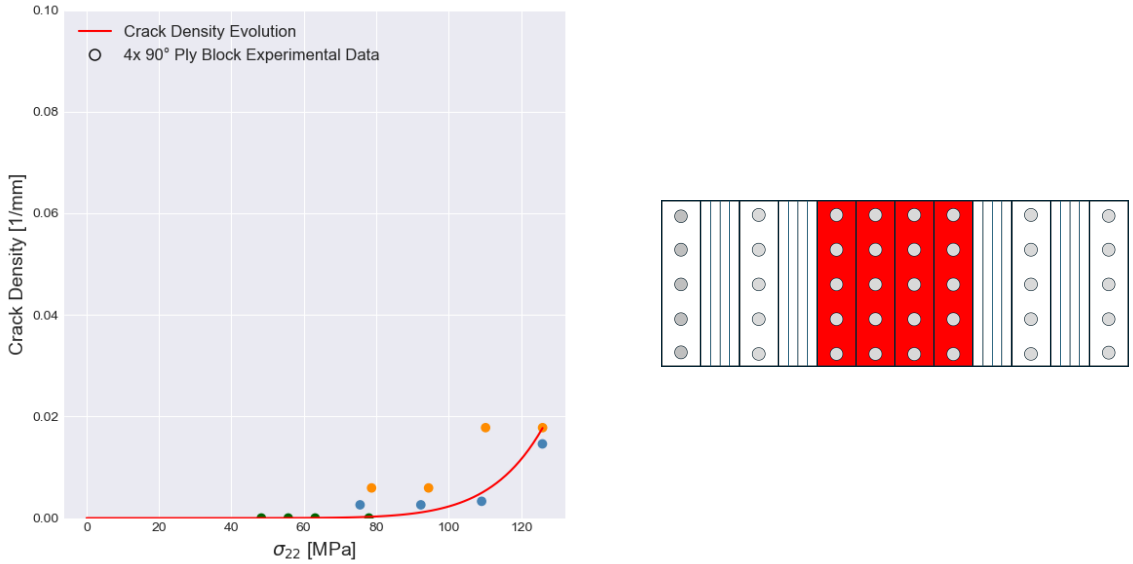

Figure 5.14: Stress-Induced Crack Density in 4x 90° Ply Block of CR Layup Family at Room Temperature.

Four plies thick middle region layup - CR1

The middle block of transverse plies consisting of 4x 90° plies in CR1 samples shows good repeatability of data around the crack nucleation local stress. This consistency indicates that the material's behaviour under stress is reliable and predictable for this sample family. Each sample of the CR1 family in Figure 5.15 is plotted using a different colour, to allow clear visual differentiation and comparison. However, when this stack of 4x 90° plies is compared to the CR sample family in Figure 5.14, CR1 shows lower microcracking strength values. Thus, a higher crack density was developed at a lower local stress in the CR1 samples.

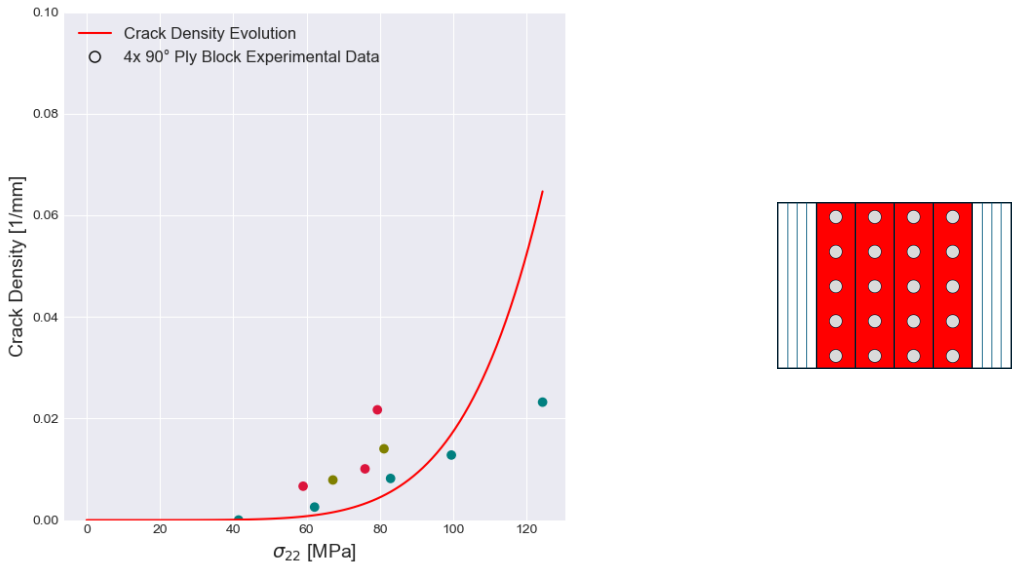

Figure 5.15: Stress-Induced Crack Density in 4x 90° Ply Block of CR1 Layup Family at Room Temperature.

Two plies thick middle region layup - CR2

The two plies thick middle block of 90° plies in the CR2 sample family developed cracks at a relatively low local stress compared to both the CR and CR1 sample families. This indicates a lower threshold for crack initiation in the CR2 samples. However, the crack density near the crack nucleation local

stress shows good repeatability between individual specimens in the CR2 family, as can be seen in Figure 5.16.

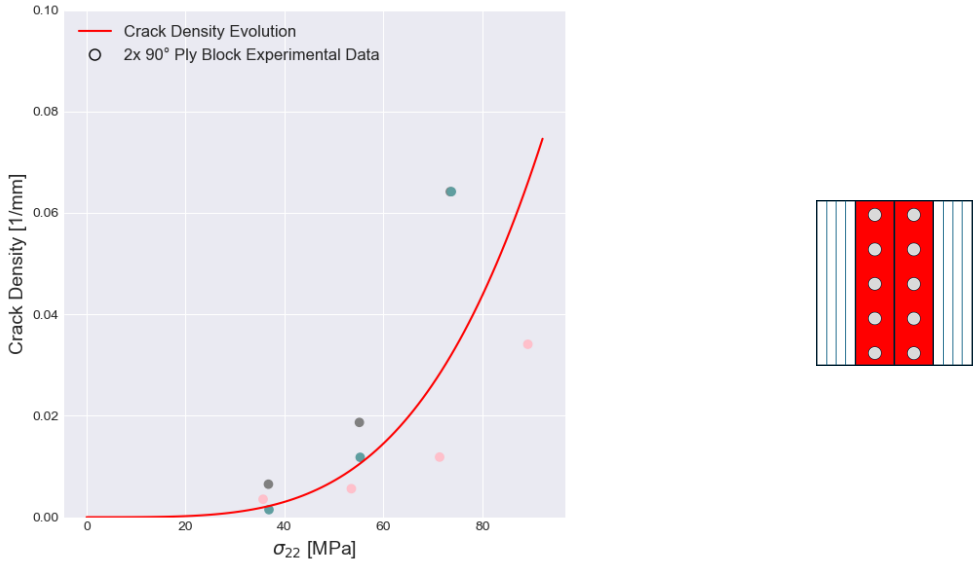

Figure 5.16: Stress-Induced Crack Density in 2x 90° Ply Block of CR2 Layup Family at Room Temperature.

Transverse plies on the outside only layup - CR3

The outer 90° plies of the CR3 family, as shown in Figure 5.17, exhibit significantly higher crack densities compared to the inner 90° plies. Note that the scale of crack density has changed, similar to the outer plies of the CR layup in Figure 5.12. The experimental data are for a sample with two symmetrically placed 90° plies on each side of the specimen.

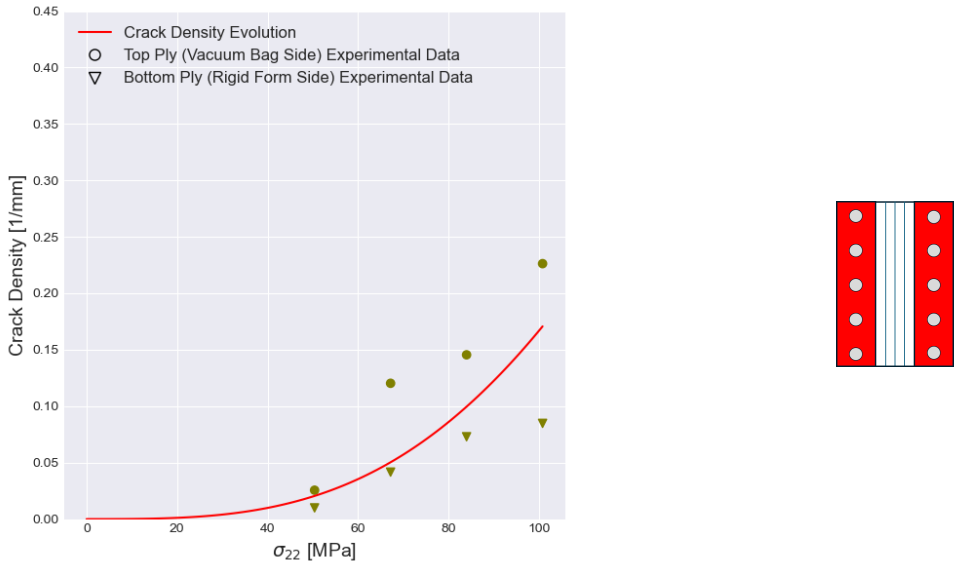

Figure 5.17: Stress-Induced Crack Density in Outer 90° Plies of CR3 Layup Family at Room Temperature.

One ply thick middle region layup - CR4

The last set of samples tested at room temperature are the CR4 samples, which feature a single 90° middle ply and 0° plies on the outside of the specimen. As shown in Figure 5.18, there is limited

scatter between individual samples around the first crack nucleations. Subsequently, there is a gradual increase in crack density with increasing local stress in the 90° ply.

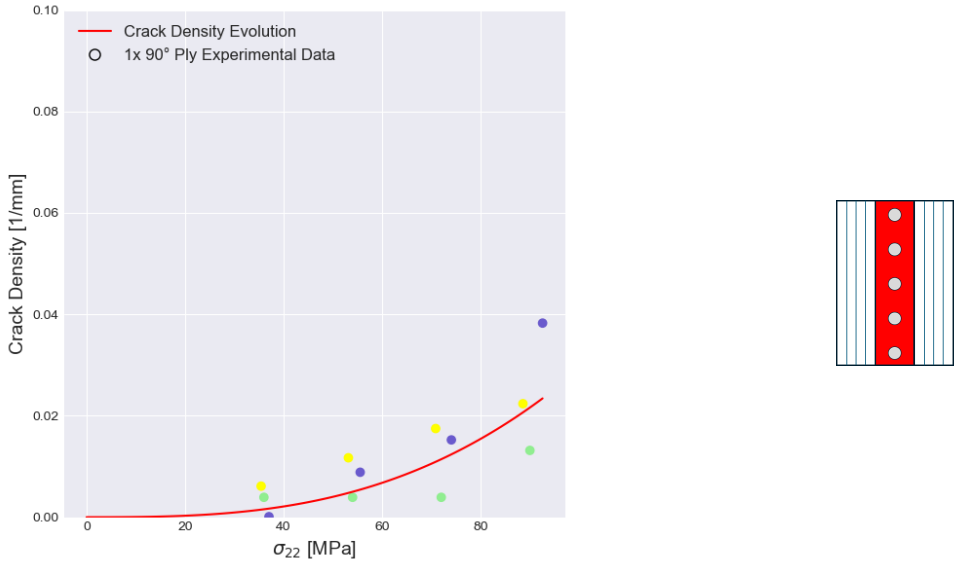

Figure 5.18: Stress-Induced Crack Density in 90° Ply of CR4 Layup Family at Room Temperature.

5.2.2. Cold Temperature Microcracking Testing

Cold temperature testing was conducted in a climate chamber at -65°C. A thermocouple attached to the testing rig near the sample indicated temperature variations of around ±8°C due to the on/off cooling control system. As introduced in Table 3.2, two sample families, CR and CR2, each consisting of three samples each, were tested.

The graphs present crack density as a function of externally applied local stress σ_{22}. However, the change in temperature to -65°C introduces additional internal residual stresses, making direct comparison between room temperature and cold temperature tests inappropriate. For this part of the analysis, only the stresses caused by mechanical loading are considered when plotting the σ_{22} variable.

All specimens tested at low temperature were thermally conditioned before any mechanical loading. Thermal conditioning consisted of leaving the specimens in a closed climate chamber at -65°C for one hour. After this temperature cycle, the specimens were examined for any cracks using an optical microscope.

Compounded layup of three different ply types - CR

The results for the CR sample family at cold temperatures are presented in three graphs, similar to the room temperature tests. The first graph, Figure 5.19 shows the microcracking evolution for the outer 90° plies. It distinguishes between the vacuum bag side and the form / mould side, showing a clear difference between the two. As with the previous cases of outer plies, this graph uses a different scale due to the significantly higher damage severity compared to all other configurations.

The second graph, for the CR layup in Figure 5.20, shows the crack density evolution for the two symmetrically placed 1x 90° plies, distinguishable by the marker shape. Some cracks nucleated at low load levels and showed no evolution in subsequent loadings. This highlights the stochastic probability distribution of crack nucleation, even at low loads, which must be considered when predicting microcracking.

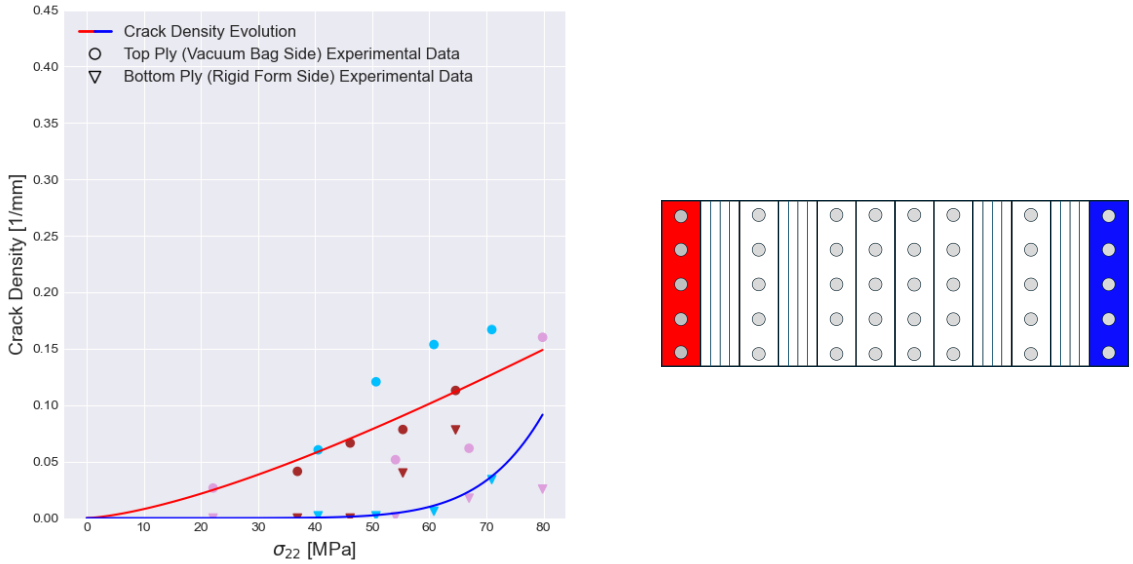

Figure 5.19: Stress-Induced Crack Density in Outer 90° Plies of CR Layup Family at Cold Temperature.

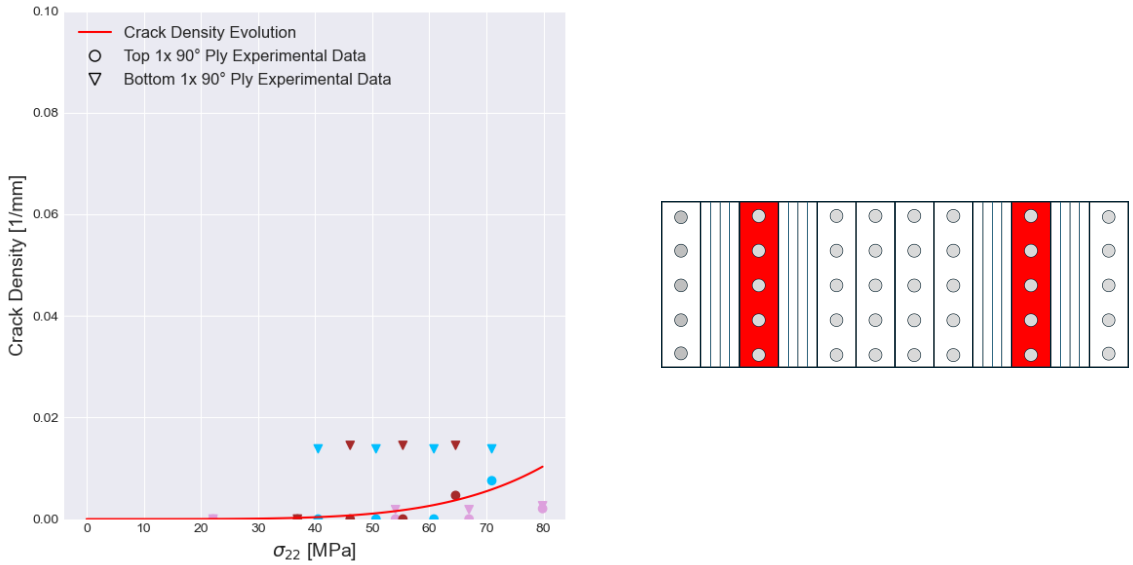

Figure 5.20: Stress-Induced Crack Density in 90° Plies of CR Layup Family at Cold Temperature.

The last graph in Figure 5.21 shows the crack growth for the 4x 90° plies thick block in the middle of the CR specimens. This particular layer exhibited very little microcracking across a range of applied local stresses.

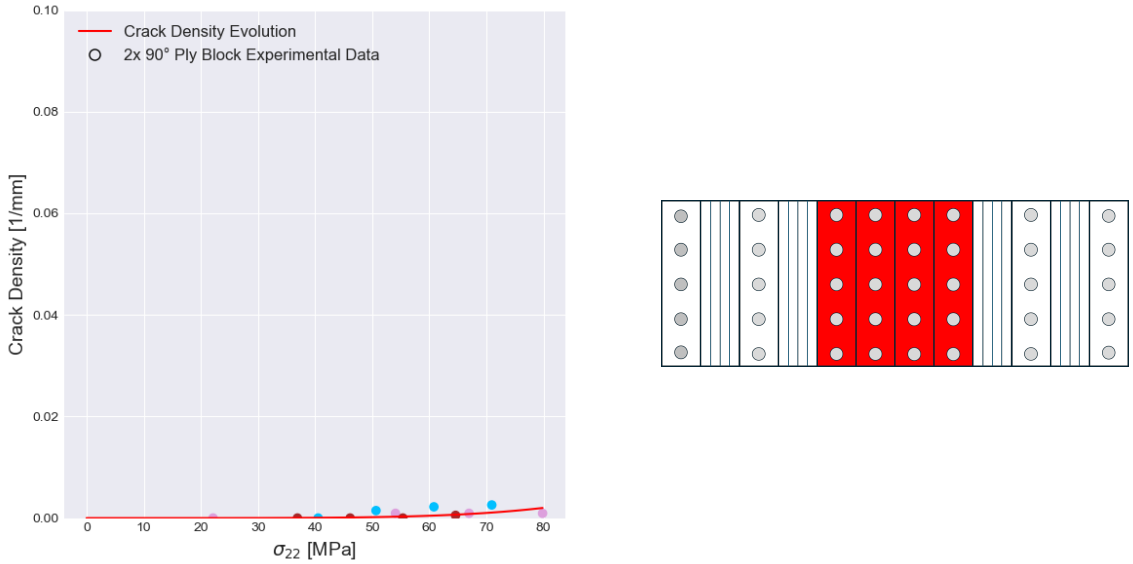

Figure 5.21: Stress-Induced Crack Density in 4x 90° Ply Block of CR Layup Family at Cold Temperature.

Four plies thick middle region layup - CR1

The final tested specimens were from CR2 layup, with a transverse block ply thickness of two plies at cold temperature. Unfortunately, data from two loadings of CR2-HT-4 were lost due to accidental overwrite. However, the collected data show a clear increase in a crack density over the tested loads, as shown in Figure 5.22.

This last test concluded the microcracking testing at both room temperature and -65°C. Detailed numbers for each sample and each loading step can be found in Appendix B. The appendix also includes stiffness evolution graphs. An extensometer measured elongation during the microcracking tests, which was then analysed. Stiffness at various load levels was plotted for each sample to determine if microcracking damage visibly influenced the stiffness of the specimens. However, this was not confirmed, so the results are not presented in this main chapter.

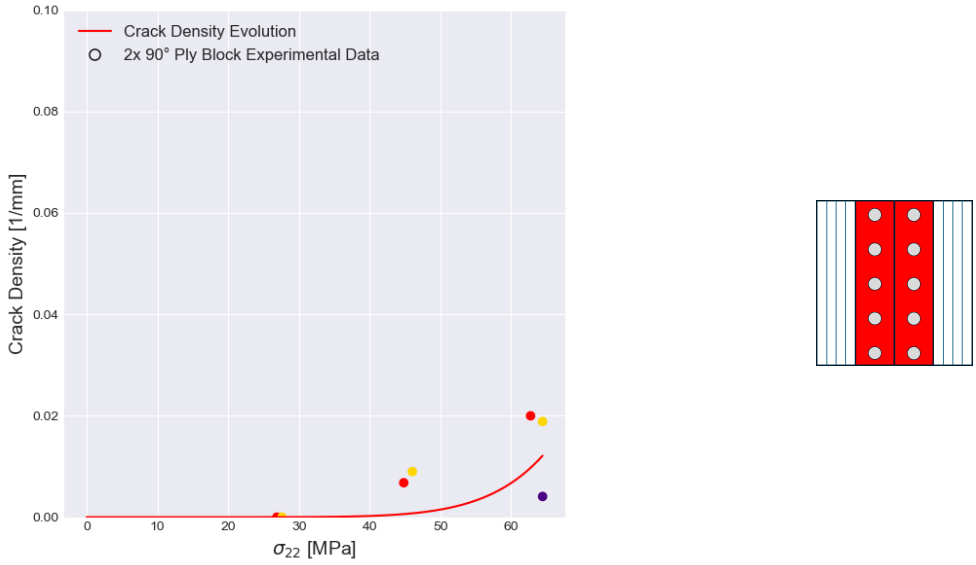

Figure 5.22: Stress-Induced Crack Density in 2x 90° Ply Block of CR2 Layup Family at Cold Temperature.

5.2.3. Microcrack Visualization Using CT Scanning

Specimens CR-HT-2, CR-HT-3, and CR2-HT-2 underwent CT scanning following the completion of the loading cycle and microcrack characterization. Due to the space constraints of the CT scanner, each specimen was divided into two sections. The first section, referred to as the 'Edge Part Cut-Out,' included the edge observed with the optical microscope during the microcracking tests. The second section, named the 'Middle Part Cut-Out,' did not include either edge. The schematic illustration of the cutting process is shown in Figure 5.23. To enhance the contrast between the cracks and the substrate, a dye penetrant was applied.

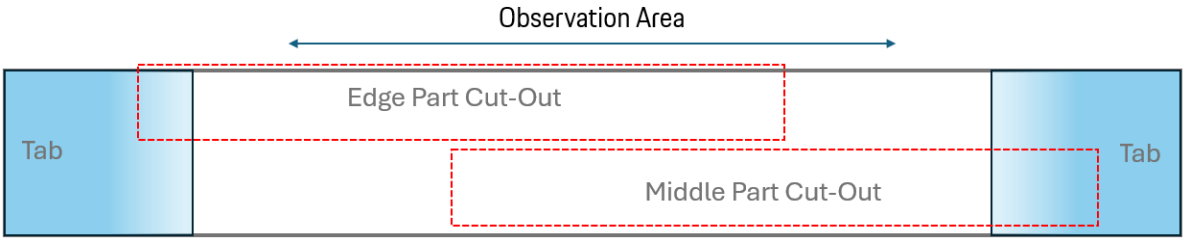

Figure 5.23: Cutting Diagram for the CT Scanning.

Unfortunately, despite selecting samples with the highest number of observed cracks for scanning, no cracks could be detected in either section of the CR2-HT-2 specimen. This could be attributed to the insufficient resolution of the CT scanner for detecting such small cracks, or there may have been another unidentified error in the scanning process for this particular sample.

Several cracks were identified in the CR-HT-2 specimen. In Figure 5.24, both a 3D image of the entire specimen scan and a top-down image from the inside of the outer ply are presented. The horizontal lighter lines represent the cracks. Most of the cracks span from the edge across the entire width of the specimen, confirming the hypothesis that the number of cracks observed on the edge is representative of the number of cracks within the specimen. These cracks were also easily identifiable from the scans, indicating that the dye penetrant had sufficient time to penetrate the entire length of the specimen and provided good contrast between the cracks and the substrate. All the observable cracks in this section of the sample were in the outer, most cracked ply.

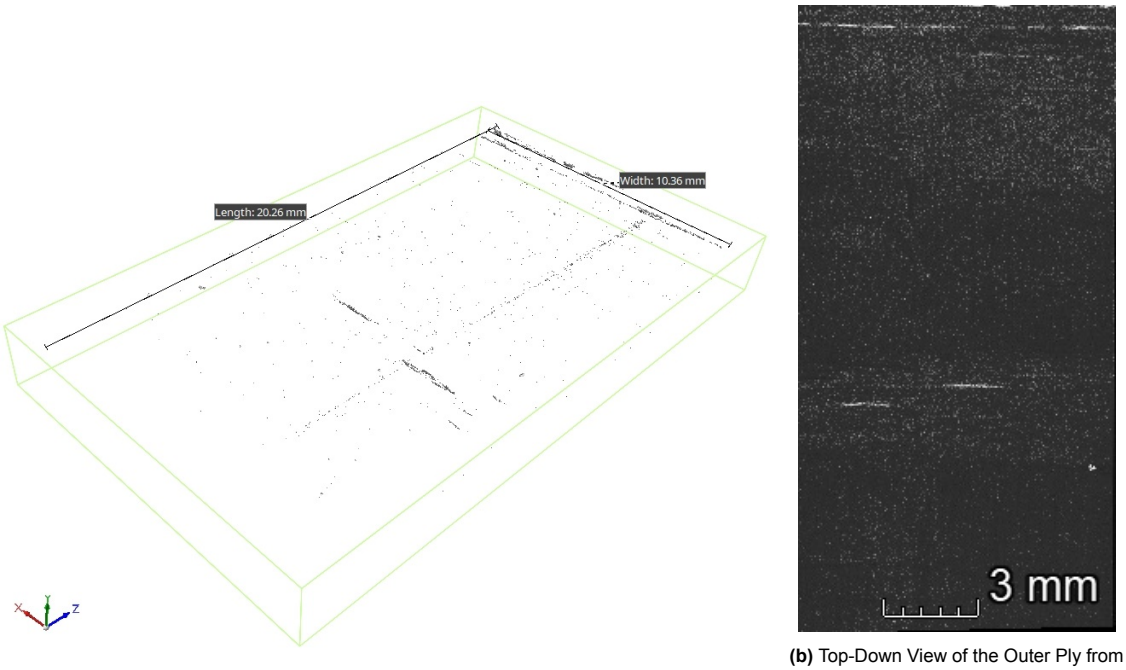

(a) 3D CT Scan of CR-HT-2.

(b) Top-Down View of the Outer Ply from CT scan of CR-HT-2.

Figure 5.24: CT Scan of the Edge Section of the CR-HT-2 Sample.

The second, middle section of the CR-HT-2 sample is shown in Figure 5.25. The 3D image of the scan in Figure 5.25a reveals a variety of crack lengths observed in this section. Although difficult to see from the image, the most prominent crack running the entire width of the specimen is located in the outer ply, as expected from the previously discussed results.

In contrast, the smaller, more scattered cracks originate from the middle block of four 90° plies. Seemingly, these cracks do not extend from edge to edge of the sample section. The top-down view in the Figure 5.25b is from the inside of the middle ply block, also shows the smaller, scattered cracks. This might be caused by accumulation of the dye penetrant on one side of the crack. It would be impossible to see any cracks with the imagining resolution of 0.012 mm without the contrast fluid penetrating into the cracks from the edge of the specimen. Therefore, the edge part of the crack is simply not visible, but the cracks must extend to the edge.

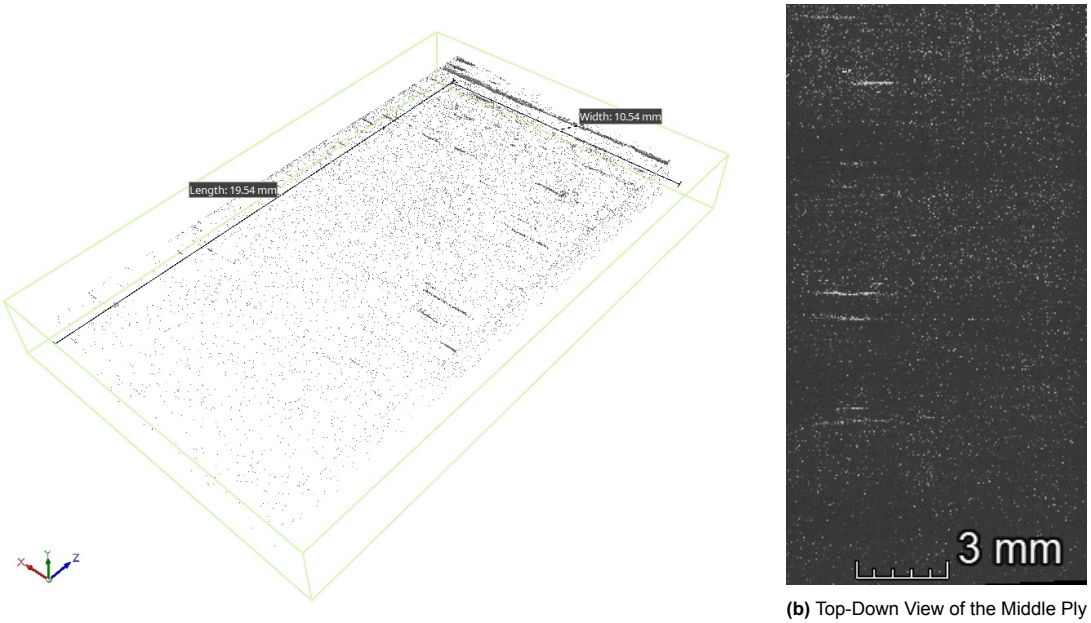

(a) 3D CT Scan of CR-HT-2.

(b) Top-Down View of the Middle Ply Block from CT scan of CR-HT-2.

Figure 5.25: CT Scan of the Middle Section of the CR-HT-2 Sample.

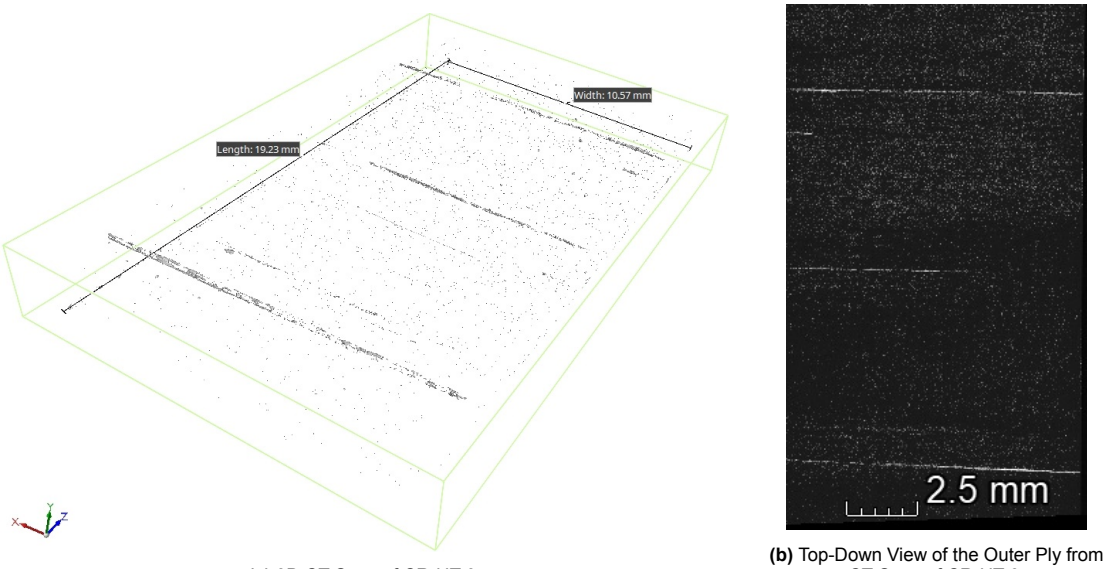

(a) 3D CT Scan of CR-HT-3.

(b) Top-Down View of the Outer Ply from CT Scan of CR-HT-3.

Figure 5.26: CT Scan of the Edge Section of the CR-HT-3 Sample.

The CT scan of the edge section of CR-HT-3 in Figure 5.26 again shows cracks only in the outer plies. The top-down view in Figure 5.26b is taken from the inside of the outer ply. The same observation applies to the CT scan of the middle section in Figure 5.27, where only the cracks in the outer ply are visible, and the top-down view is also taken from this ply. Interestingly, the crack spacing appears to be very similar in both top-down views.

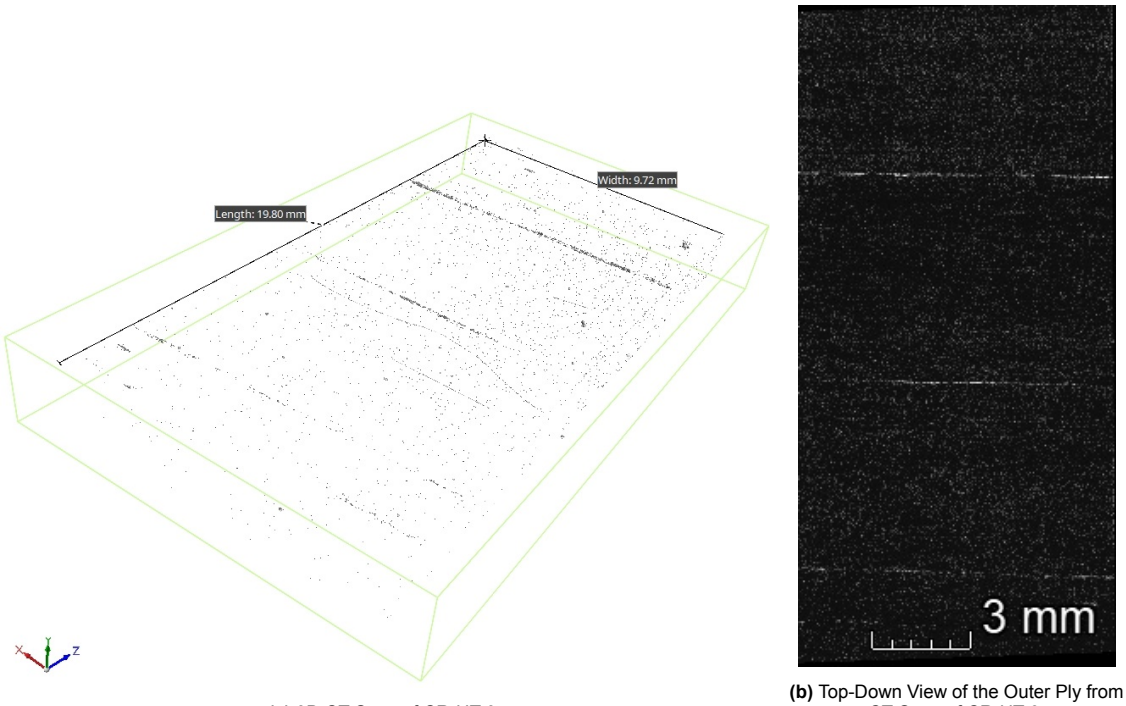

(a) 3D CT Scan of CR-HT-3.

(b) Top-Down View of the Outer Ply from CT Scan of CR-HT-3.

Figure 5.27: CT Scan of the Middle Section of the CR-HT-3 Sample.

5.3. Evaluation of Residual Stresses

The first step in evaluating the residual stresses is to measure the physical dimensions of the non-symmetric composite strips. Each strip is 15 mm wide, and the lengths are provided in Table 5.6. Of the four samples, two underwent heat treatment and are labelled 'HT', while the other two samples, which did not receive heat treatment, are labelled 'NT'. The heat treatment consisted of heating the material to 180°C, holding it at that temperature for 6 hours, and then gradually cooling it down to room temperature over a 3-hour period.

Table 5.6: Residual Stress Specimens Lengths.

	RS-HT-1	RS-HT-2	RS-NT-3	RS-NT-4
Specimen Length [mm]	244.7	244.5	244	245
Specimen Width [mm]	15	15	15	15

The samples were placed in a climate chamber for low-temperature tests and in an oven for high-temperature tests. A thermocouple was used to log the temperature of the samples. Figure 5.28 presents an example of a test performed in the climate chamber.

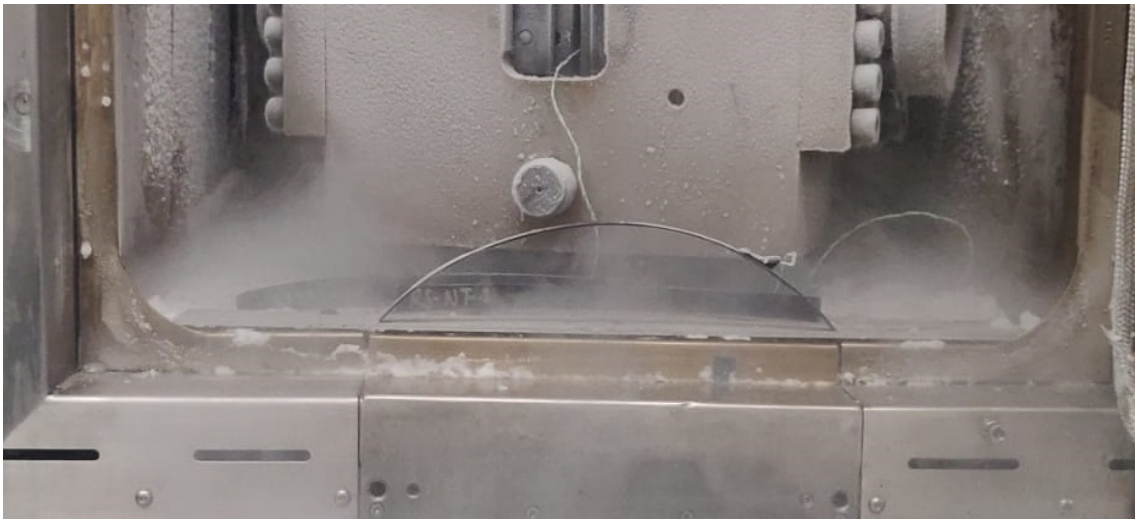

Figure 5.28: Curvature Measurement in a Climate Chamber

The measured values of the sagittae of the samples (the distance from a plane to the highest point of the sample) are presented in Table 5.7. As expected, the distance decreases with increasing temperature, as the residual stresses relax with the increase in temperature.

Table 5.7: Sagitta Measurement for Unsymmetrical Specimens.

Temperature [°C]	RS-HT-1 [mm]	RS-HT-2 [mm]	RS-NT-3 [mm]	RS-NT-4 [mm]
150	19.28	20.41	16.77	16.94
100	28.94	30.31	23.23	24.79
75	33.96	34.30	30.11	29.55
50	37.85	38.70	33.86	33.98
24	40.65	40.93	35.84	37.07
0	44.05	44.21	39.68	39.98
−25	46.53	46.21	41.21	42.91
−50	49.73	49.60	44.21	45.20
−60	51.18	51.55	48.14	48.22

The graphical representation of the measured values is shown in Figure 5.29a. These measurements are then processed to obtain the radius of curvature and the curvature for each sample, as explained in section 3.3. The resulting radii of curvature are displayed in Figure 5.29b. In both plots, the dashed blue line represents the linear extrapolation of the sagitta measurements. The intercept with the x-axis indicates the stress-free temperature. Due to the differences between the heat-treated and non-heat-treated samples, there are two stress-free temperatures: 259°C for the non-heat-treated samples and 281°C for the heat-treated samples.

This result was unexpected, as a higher stress-free temperature indicates higher residual stresses, assuming the coefficient of thermal expansion (CTE) remains constant between samples. Consequently, the performed heat treatment, which was aimed at reducing residual stresses, increased them.

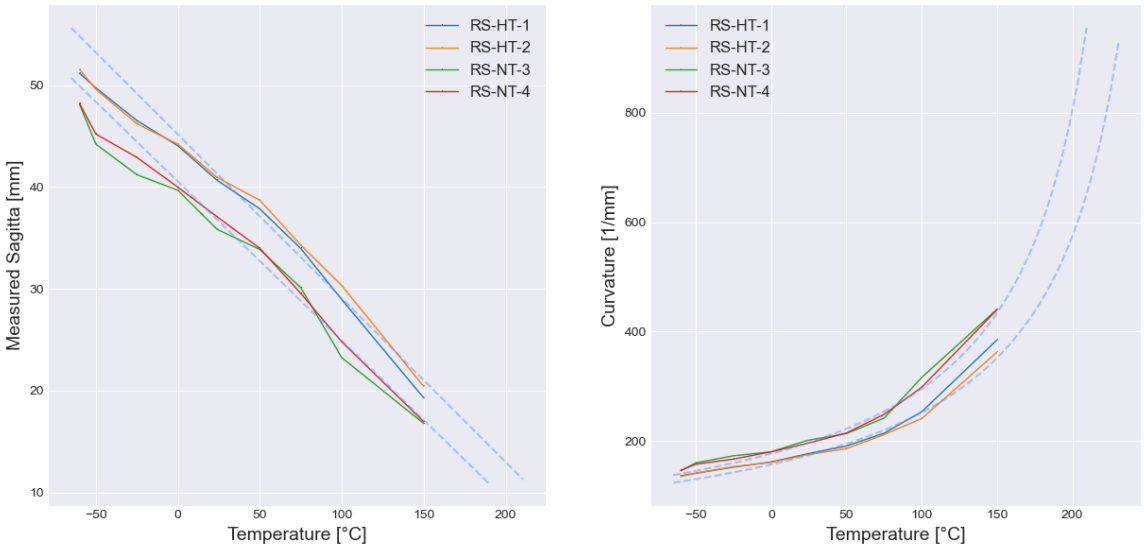

(a) Evolution of Sagittas with Temperature.

(b) Evolution of Radius of Curvature with Temperature.

Figure 5.29: Influence of Temperature on Residual Stresses in Non-Symmetrical Laminate.

Once the stress-free temperature has been obtained, the model outlined in section 4.2 can be used to verify if the predicted curvature matches the measured curvature for the non-symmetric layup. The elastic parameters used are taken from subsection 5.1.2, and the transverse stiffness as a function of temperature is taken from subsection 5.1.4. All other elastic properties are assumed to be constant with temperature. The thermal coefficients are sourced from [78], reporting values for T700G/LM-PAEK of -0.9x10^{-6}K^{-1} in the fibre direction and 38x10^{-6}K^{-1} in the transverse direction. The expected curvature, indicated by circles, compared to the measured data is shown in Figure 5.30.

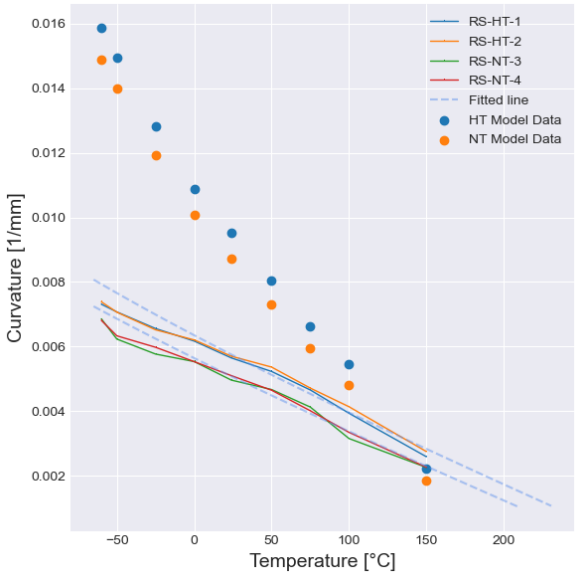

Figure 5.30: Residual Model Curvatures Versus Measured Curvatures for Non-Symmetrical Laminate.

The match between the measured curvature and the calculated curvature in Figure 4.7 is not optimal, especially at low temperatures. This discrepancy might be caused by assuming constant values for the coefficients of thermal expansion (CTE) over the entire temperature range. If the CTE in the fibre direction is kept constant and independent of temperature, it is possible to find a transverse CTE that aligns the measured and calculated curvatures. Subsequently, if the transverse CTE as a function of

temperature is obtained, the residual stress model can be verified.

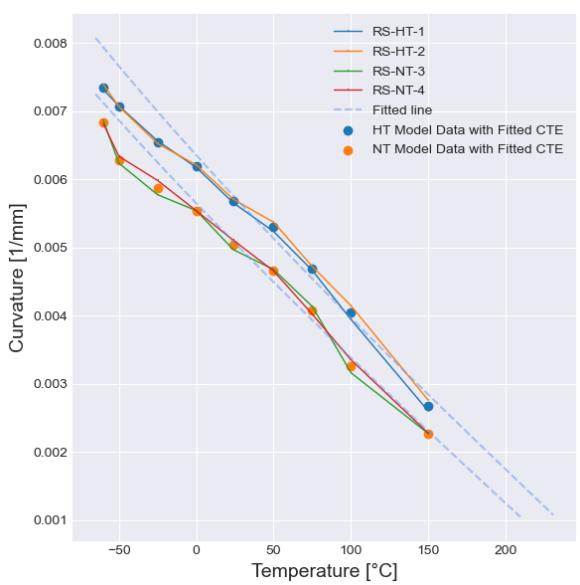

(a) Model Matched (in Circles) Curvature Evolution.

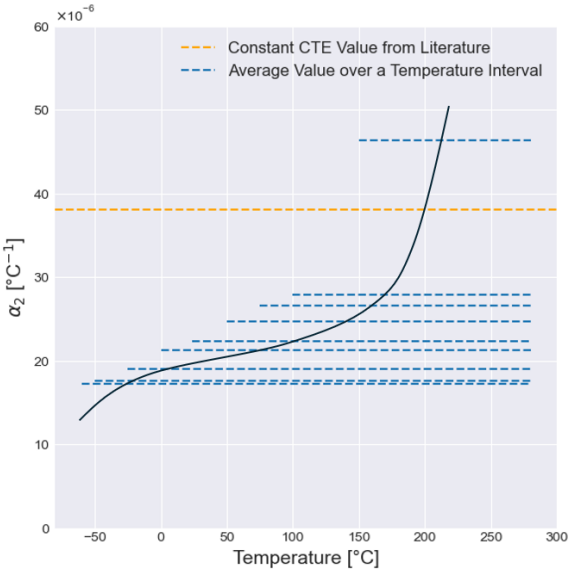

(b) Calculated Average CTE_{22} on Given Interval (Dashed Blue Lines) and Estimation of the Function in Solid Line.

Figure 5.31: Model Matching to Calculate CTE_{22} Evolution with Temperature

The updated curvature plot with the model-fitted values can be seen in Figure 5.31a. The plot in Figure 5.31b illustrates the estimated transverse CTE required as a function of temperature for the model to exactly fit the measured curvature. As explained in section 4.2, the model uses the average CTE value between two temperature points. The dashed blue lines represent this average from T_1, the stress-free temperature, to a given T_2. The length of the dashed blue lines corresponds to this interval. The dashed orange line shows the constant CTE value found in the literature, which was used for Figure 5.30. The solid grey line is a third-degree polynomial fit, suggesting how the actual CTE function might behave. Although there is no reason why the actual CTE function should follow a third-degree polynomial, this fit illustrates the overall trends and approximately fulfils the given boundary conditions.

Several observations can be made regarding the behaviour of the actual unknown function of transverse CTE over the temperature range. At low temperatures, the CTE decreases. Around room temperature, the CTE remains approximately constant, with a rapid sharp increase near the glass transition temperature, which is 147°C for this material.

6 Discussion

This chapter discusses the final results of the three main parts of the thesis. The first section focuses on the elastic properties, with particular attention given to the developed evolution of transverse stiffness with temperature. The next section examines the increase in stresses between room temperature and cold temperature, as well as the effects of the applied heat treatment. The last section on microcracking addresses the thickness effect observed in the tested TC1225/T800 material and, finally, the (lack of) correlation between microcracking tests conducted at room temperature and those conducted at cold temperatures.

6.1. Elastic properties

In this thesis, a number of elastic properties were determined that are then used in subsequent models. Accurate determination of the elastic properties provides a basis for all the modelling efforts. The longitudinal Young's modulus determined at room and cold temperatures showed little to no effect of the temperature on this property. This was expected as it is a fibre dominated direction and little effect of temperature on carbon fibre dominated properties was expected as discussed in section 2.2.

The transverse Young's modulus showed an increase of 16% over the temperature range tested. This led to a dynamic mechanical analysis (DMA) of the pure matrix thermoplastic. Using the DMA data and the Halpin-Tsai equations, a model for stiffness evolution was proposed, as shown in Figure 6.1 in blue. This model is based on the physical stress-sharing between matrix and fibre constituents in the composite. However, with additional data generated at cryogenic temperatures by the COCOLIH2T partners, it became evident that the model overestimates the transverse stiffness even at -100°C. Consequently, a trilinear illustration of more realistic evolution is also presented in Figure 6.1 in orange. No other elastic properties were tested over both at room temperature and at -65°C. However, it may be necessary to construct a model for the temperature evolution of the shear modulus as well. This was not pursued due to the poor performance of the transverse stiffness rule of mixtures model and the lack of additional time to test the shear modulus at low temperatures that would be required for a model.

6.2. Residual Stresses and Heat Treatment

The result of the residual stress analysis is a model for assessing the residual stresses in the material. During the analysis, the stress-free temperature, transverse CTE, and transverse stiffness as functions of temperature were determined. This information is now synthesised to find the increase of the residual stresses between room temperature and cold temperature (-65°C). This synthesis allows for a comparison of both testing conditions using the total local stress, which consists of the applied mechanical stress and the thermal stress.

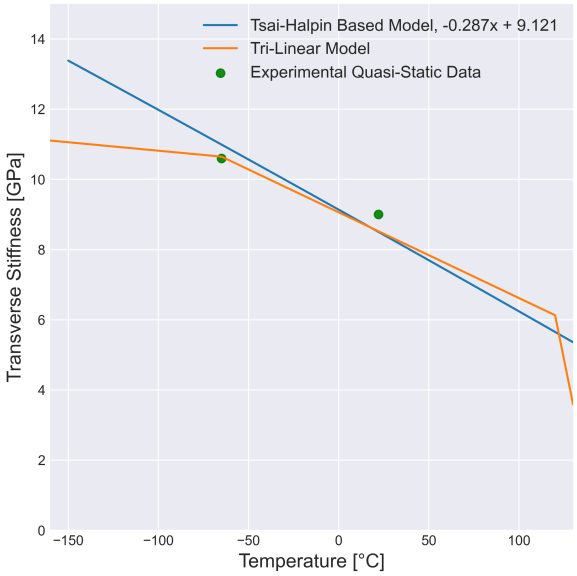

Figure 6.1: Two Models Used for Transverse Stiffness Evolution with Temperature.

Table 6.1: Residual Stresses Summary for CR and CR2 Layups.

	CR-HT	CR2-HT
At Room Temperature (22°C)	42.8 MPa	44.8 MPa
At Cold Temperature (-65°C)	56.3 MPa	59.8 MPa
Difference	13.5 MPa	15 MPa

Curvature measurements of the non-symmetrical layup were used to calculate the stress-free temperature. These curvature measurements at different temperatures provide valuable insights into the residual stresses.

The main objective of the residual stress model was to decouple the material's stiffening effect from the evolution of CTEs with temperature.

To achieve this, three different tests were planned. First, a dynamic stiffness measurement was conducted with a very small preload of 0.1 N applied prior to each test at a given temperature, which offsets the influence of thermal expansion on the test results. Secondly, a TMA test was planned to precisely measure the thermal expansion of the material without the influence of stiffening. Lastly, the residual stress model would be used to couple these two phenomena back together. The results would then be compared to the curvature measurements of the non-symmetrical samples, where the coupling of stiffening and CTE evolution is present.

However, this model verification was not possible due to a malfunction of the TMA machine. Therefore, an alternative approach was chosen, in which the average CTE in the direction transverse to the fibres was calculated for certain temperature ranges, but the model could not be validated due to missing CTE measurements.

The importance of parameter evolution can be illustrated by comparing the residual stress for CR and CR2 layups between room temperature and -65°C. The CLT model with evolving parameters, as shown in Table 6.1, predicts a residual stress increase of 13.5 MPa for the CR layup and 15 MPa for the CR2 layup. In contrast, using the same model with constant room temperature values for E_{22} and α_2 gives residual stresses of 26 MPa and 27.3 MPa, respectively. This represents increases of 1.93x and 1.82x compared to the presented parameter-evolving approach.

Yet, there are indications that the calculated residual stress might be underestimated due to the sensitivity of the CTE evolution to measurement errors. Observations during the non-symmetric

samples production revealed that curvature depends on the samples' physical width, a factor not accounted for by CLT, which assumes an infinitely large 2D plate. CLT predicts that thermal loading causes the non-symmetric laminate to deform into a saddle shape with equal curvature in both directions. However, finite plates exhibit bi-stable equilibrium, developing curvature in only one direction unless a perturbation changes the equilibrium position. This restricted deformation field 'locks-in' some residual stress, reducing curvature. To mitigate this effect, samples should be as thin as possible. The tested samples were 15 mm wide, but a decrease in width would result in higher curvature. The higher measured curvature would then lead to higher calculated values for CTE.

Finally, the heat treatment used had a negative effect on the residual stresses in the material. The treatment involved ramping up to 180°C, maintaining this temperature for 6 hours, and then slowly ramping down to room temperature over 3 hours. Previously, measurements from the COCOLIH2T partners showed a reduction in curvature after a similar heat treatment. However, in this case, the heat-treated samples exhibited higher stress-free temperatures and consequently higher residual stresses than their non-heat-treated counterparts.

The increase in residual stresses observed in the heat-treated samples can be explained by the effects of annealing at temperatures above the glass transition temperature (T_g) and within the crystallization range. At 180°C, the heat treatment temperature is above the T_g of the LM-PAEK matrix (147°C) but below its melting temperature (T_m) and crystallization temperature (T_c). Under these conditions, annealing can lead to an increase in the crystallinity level of the materials. This increase in crystallinity is accompanied by an increase in matrix modulus, which makes the material stiffer [49].

As crystallinity increases, so does the crystallization-induced shrinkage during cooling, creating a more pronounced mismatch in thermal contraction between the crystalline and amorphous regions. This enhanced shrinkage results in higher residual stresses within the material [49]. Consequently, while a similar heat treatment might have previously resulted in a reduction in curvature, the current samples exhibit higher stress-free temperatures and, therefore, higher residual stresses.

6.3. Microcracking

Microcracking testing is a time-consuming process and is sensitive to specimen preparation. High-quality edge polishing is essential to make the cracks to be observable. Since the samples are detected with an optical microscope while unloaded, there was a concern that the cracks might close completely, making them invisible. Although it is difficult to guarantee that all cracks were noticeable, the reproducibility of finding cracks indicated that they had not closed to the point of being unobservable. This reproducibility in locating the same cracks at different load levels allows crack growth to be observed. An example of a crack evolution can be seen in Figure 6.2.

The crack shown in Figure 6.2 formed in the outer ply of the CR layup sample. These outer plies exhibited the highest crack density compared to all other plies in all the layups tested. Both the number of crack nucleations and the average crack length were highest for these specific plies. However, as indicated by one of the COCOLIH2T partners, the poor performance of these layers might have been influenced by a manufacturing error, since two different batches of plates were tested and the second batch did not perform as poorly. This discrepancy could not be confirmed within the scope of this thesis, as all plates provided by the COCOLIH2T consortium were manufactured in a single batch. Nevertheless, this potential issue should be considered when interpreting the results for the outer plies. As discussed in section 2.2, there was initial concern that crack density from the cold temperature tests could be higher compared to room temperature tests due to trapped humidity between the layers, which could freeze and expand. However, this effect was not observed, and the microcracking performance was similar at both room and cold temperatures. Therefore, it can be concluded that the process conditions were controlled effectively, preventing this issue from occurring.

The remaining subsections discuss the thickness effect reported in the literature. The results of the microcracking tests at different temperatures are compared using the previously determined residual stresses. Lastly, more details of the crack structure are discussed.

6.3.1. Thickness Effect

Nair [39] showed that the stress required to nucleate the first microcrack decreases with the total thickness of 90° plies in $[0/90_n]_s$ laminates. This phenomenon is generally known as the thickness effect. It cannot be predicted by a stress-based failure criterion without resorting to the concept of in

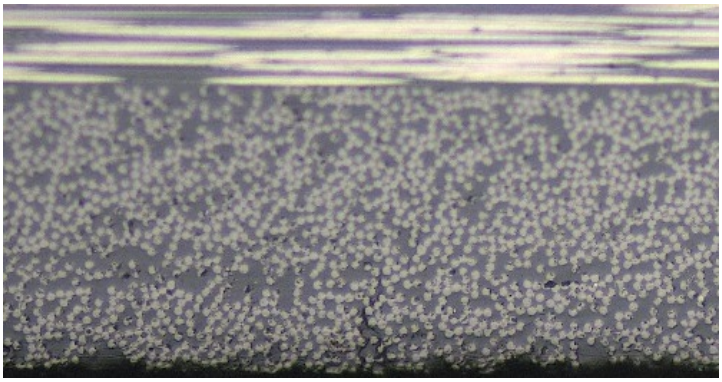

(a) Crack after 15 kN Applied Load.

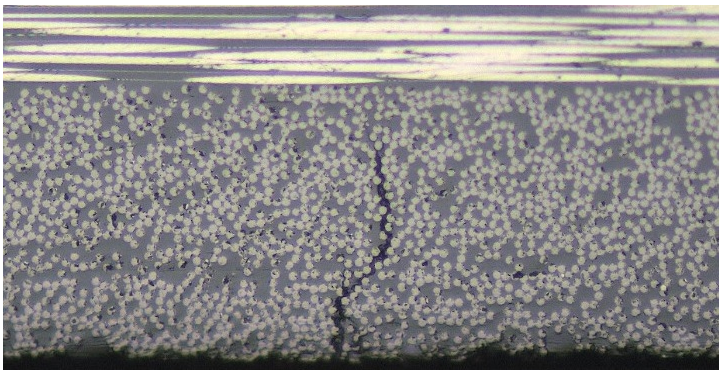

(b) Crack after 17.5 kN Applied Load.

Figure 6.2: Crack Evolution.

situ strength properties, which limits the predictive capabilities. However, when examining Figure 6.3, which shows test results of the CR1, CR2, and CR4 samples, the thickness effect is not as obvious as it is for the AS4/3501-6 thermosetting composite material used in Nair's study.

It is evident from Figure 6.3 that the single 90° middle ply of CR4 (in green) performs better than the stack of two plies in CR2 samples (in orange). The microcracking curves for these two layups have similar shape parameters and are therefore easily comparable. However, the microcracking curve of the CR1 samples (in blue) has a very different shape. Cracks start to nucleate at a local stress similar to the two-ply thick block, but the evolution is slower, and the curve even crosses the single ply curve.

To explain why the thermoplastic composite TC1225/T800 material does not exhibit a clear thickness effect compared to 3501-6/AS4, one can refer to the finite fracture mechanics approach used by Nair [39]. This approach was used to construct a master plot and to confirm the accuracy of the model in predicting microcracking while taking into account the thickness effect in thermosetting composites.

The approach uses an 'aspect ratio of the microcracking unit,' defined as $\rho = a/t_1$ where a is half the distance between two cracks and t_1 is the crack length equal to the ply thickness. In thermosetting composites, the crack always spans the entire height of the ply. For thicker blocks of plies, this aspect ratio decreases as the thickness of the 90° ply (and therefore the crack length) increases.

However, this increase in relative or total crack length with increased ply thickness was not confirmed for the TC1225/T800 material during the microcracking test. When comparing the average relative crack length of a four-ply thick block to any other configuration, it showed the lowest value at 0.12 of the local ply thickness, compared to 0.19 for the single ply and 0.2 for the two-ply block. When comparing the absolute crack length, the four-ply block still does not reach the highest value; it is behind the single outer plies and very close to the average crack length in the two-ply block.

The consequence of the difference in relative crack behaviour for different thicknesses of transverse plies is that the aspect ratio of the microcracking unit ρ does not have direct correlation to the increasing transverse ply thickness.

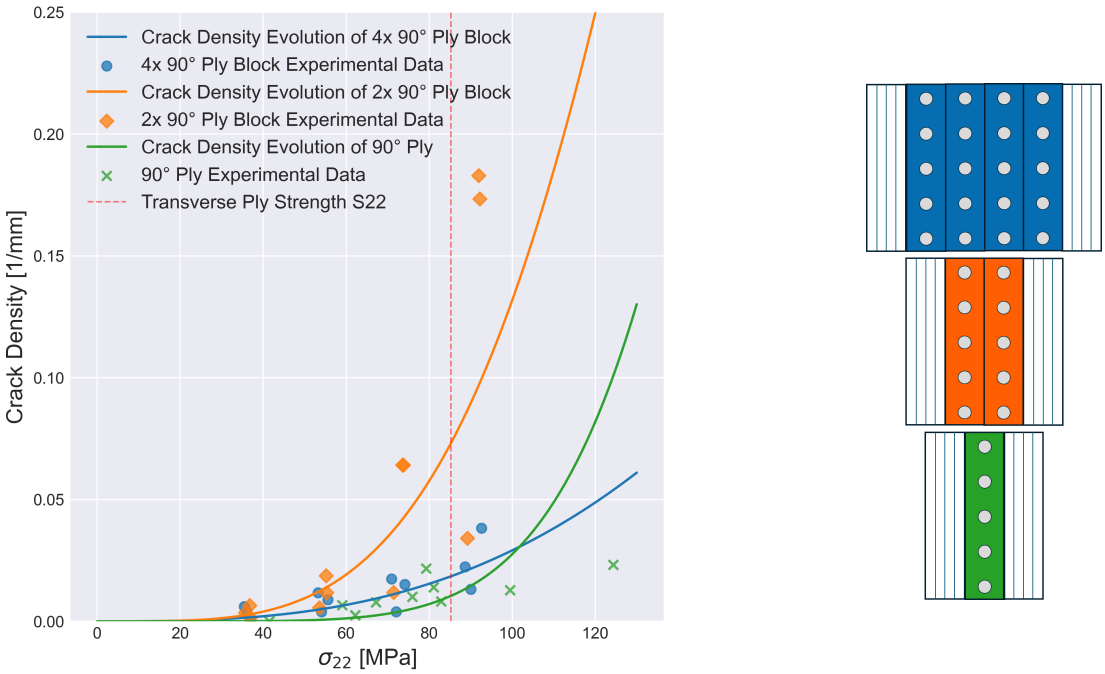

Figure 6.3: Microcracking Test Results for $[0/90_n]_s$ Layups, n = 1, 2, 4.

6.3.2. Temperature/Residual Stress Effect

The graphs in this subsection display three curves and one vertical line. The solid orange line represents microcracking test results at -65°C, with the experimental data points in triangles, while the dashed blue line shows results from the same ply tested at room temperature. The solid blue line depicts the shifted room temperature results to -65°C, adjusted for the calculated residual stresses. The red vertical line indicates the determined strength of the transverse ply in tension at room temperature, also shifted to -65°C by accounting for the residual stress.

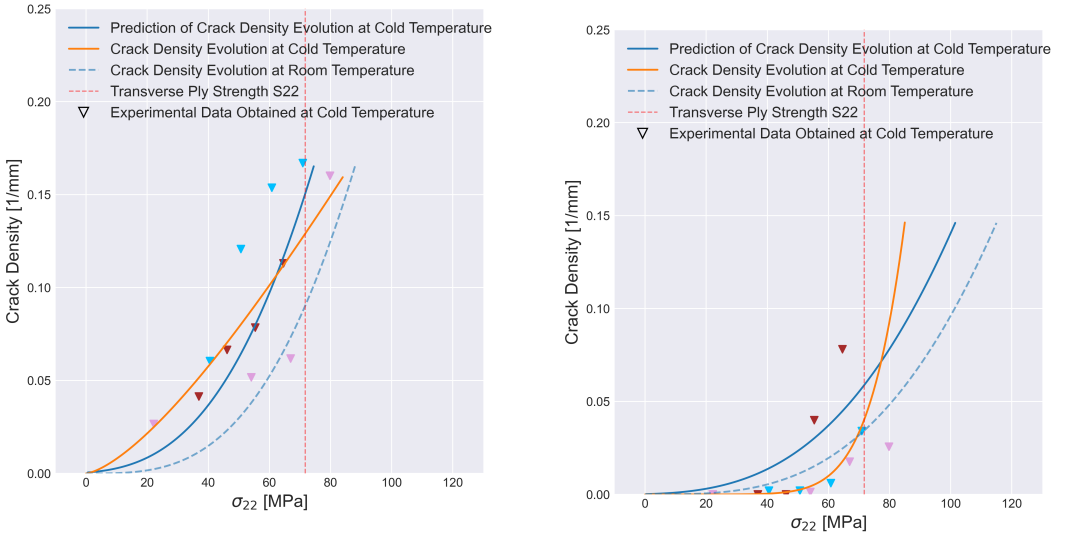

(a) Temperature Shift for Outer Ply - Vacuum Bag Side - of CR Layup.

(b) Temperature Shift for Outer Ply - Form Side - of CR Layup.

Figure 6.4: Temperature Shift for Outer Plies of CR Layup.

The results of outer plies of CR layup are shown in Figure 6.4. For the vacuum bag side, both the predicted and experimental test curves closely match the experimental data points. However, due to

very early crack nucleation in this layer, it is difficult to determine if either curve accurately represents the precise stress onset. The form side ply, on the other hand, has more data points capturing the nucleation of the first cracks. In this case, the predicted curve performs worse than the non-shifted room temperature curve, suggesting that the material was more resistant to microcracking at low temperature (-65°C) than at room temperature. This is an unexpected result, as residual stresses would typically reduce performance. However, it is possible that the samples tested at low temperatures had fewer manufacturing imperfections, and the limited number of tested plies (three at each temperature) does not provide a statistically significant result.

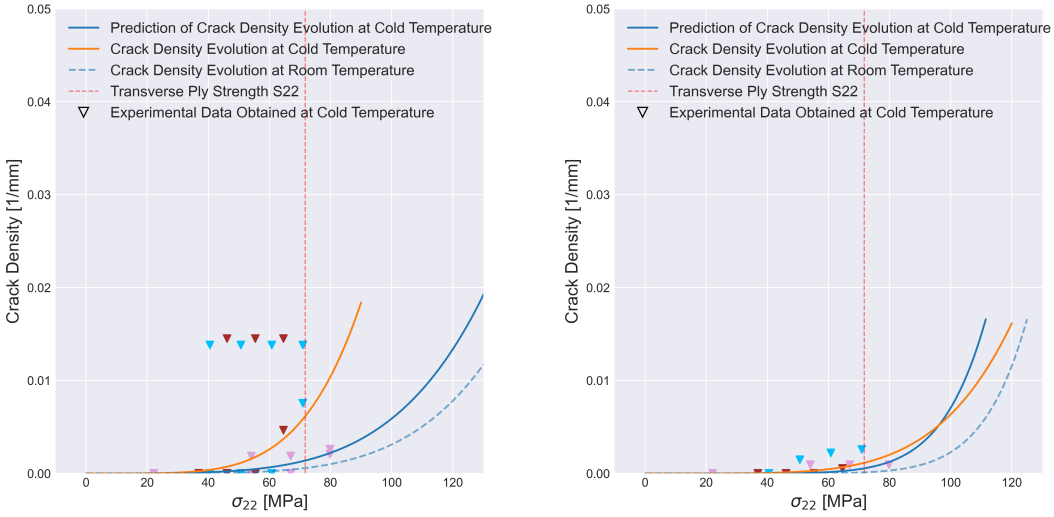

(a) Temperature Shift for a Single 90° Ply in CR Layup.

(b) Temperature Shift for a Block of 4x 90° Plies in CR Layup.

Figure 6.5: Temperature Shift for Inner Plies of CR Layup.

The results for the inner plies of the CR layup are shown in Figure 6.5. In both cases, the temperature shift brings the room temperature results closer to those at -65°C. However, a larger shift is needed for single plies to better match the cold temperature data, while a block of four 90° plies aligns well. The single ply data show skewness, with some plies cracking early and not evolving further, while others do not crack at all.

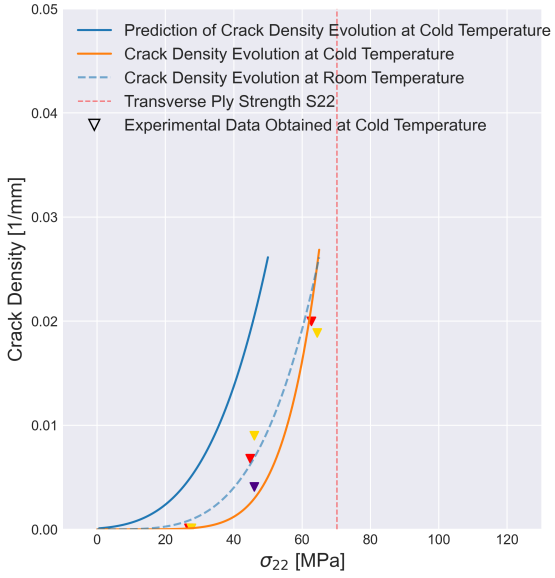

Figure 6.6: Temperature Shift for a Block of 2x 90° Plies in CR2 Layup.

The final set of samples tested at both room and cold temperatures are from the CR2 layup. The results for the middle block of two 90° plies are shown in Figure 6.6 . Here, the samples tested at low temperatures show a similar resistance to matrix microcracking as those tested at room temperature, which is unexpected since residual stresses would typically reduce performance.

Considering the research question, which aimed to determine if there is any correlation between room temperature tests and cold temperature tests, the presented results indicate that no correlation exists. There is no apparent relationship between the microcracking stress onset in the room temperature tests and the cold temperature results (-65°C). The change in results from room temperature to cold temperature could not be predicted using the residual stress model.

The results for the outer, form side 90° ply of the CR layup (shown in Figure 6.4a) and the middle block of two 90° plies of the CR2 layup (shown in Figure 6.6) indicated a slightly negative correlation, as decreasing temperature led to an increase in the stress onset of microcracking. However, this result might be influenced by low number of plies tested. As the stress onset for both the room temperature experimental curve and cold temperature experimental curve fall within expected standard deviation.

Conversely, the results for the single 90° ply of the CR layup (shown in Figure 6.5a) pointed to a positive correlation, as a decrease in temperature resulted in a decrease in the stress onset of microcracking. However, the residual stress shift was not sufficient for a good match of the results. Finally, the outer, vacuum bag side 90° ply of the CR layup (shown in Figure 6.4b) and the middle block of four 90° plies of the CR layup (shown in Figure 6.5b) showed also positive correlation and reasonably good agreement of results with the use of residual stress model.

7

Conclusions and Recommendations

This chapter presents the key findings of the research behind this thesis, comments on their significance, and provides implications resulting from these findings. It also offers theoretical recommendations and practical suggestions based on the results.

7.1. Conclusions

The objective of this thesis is to determine if there is a correlation between matrix microcracking test results at room temperature and cold temperatures, and to explore the possibility of constructing a model that allows to shift room temperature microcracking test results to match those obtained at cold temperatures.

The experimental part of this thesis focused on material characterization and provided the longitudinal and transverse modulus at room temperature and -65°C, the shear modulus and Poisson's ratio at room temperature, and a matrix stiffness evolution between -150°C and 110°C.

The measurements of curvatures of the non-symmetrical layup, combined with the elastic properties, provided input for the residual stress model. This model attempts to determine the mesoscale ply residual stresses based on the Classical Lamination Theory (CLT), with extensions for the transverse stiffness and the transverse CTE evolution.

The residual stress model was tested as the minimum required model to predict the stress onset of microcracking at cold temperatures using the results from room temperature tests.

Additionally, experimental microcracking data were generated at room temperature and at -65°C to understand the microcracking behaviour of the material, including the effects of thickness and temperature.

7.1.1. Key Findings

The material characterization confirmed that the matrix-dominated elastic properties evolve with temperature. However, the rule-of-mixtures model was not successful in estimating this evolution using the matrix stiffness data, indicating that proper laminate testing at various temperatures is necessary to accurately observe the material behaviour down to cryogenic temperatures.

The CLT model, when incorporating evolving elastic and thermal parameters, resulted in lower calculated residual stresses compared to using constant, non-evolving inputs.

Microcracking testing using optical microscopy demonstrated the reproducibility of crack observation. Results revealed that the outer 90° plies were the most susceptible to microcracking, while single 90° plies exhibited the highest stress onset for microcracking. Additionally, tests conducted at room and cold temperatures showed a similar evolution in microcracking density for the layups tested at both temperatures.

The proposed parameter evolving residual stress model gives significantly lower residual stresses due to the temperature evolution of the material properties used. However, this might be overly optimistic, as some parameters were calculated from curvature measurements of the non-symmetric RS laminate. Due to the restricted deformation field of the real panel, compared to the infinite plate assumed in the CLT model, the curvatures depend on the physical width of the specimen.

The absence of the so-called thickness effect can be explained by the differences in crack propagation between epoxy matrices and thermoplastic ones. In epoxy-based composites, microcracks are typically assumed to span the entire height of the 90° ply. This behaviour contrasts with tougher thermoplastic matrices, where, after a crack nucleates, there is no significant evolution, and the crack growth is very slow, even at higher load levels. These results show that single plies still outperform ply blocks consisting of two or four 90° plies. However, the difference in stress onset between two- and four-ply blocks is not significant.

Lastly, no correlation between decreasing temperature and the stress onset of microcracking was found based on the results of five different transverse ply configurations. A negative correlation was observed for two configurations, where the stress onset increased with decreasing temperature. A positive correlation was observed for the other three configurations, but only two configuration produced reasonable results with the proposed temperature shifting model based on determined residual stresses.

7.1.2. Limitations

The residual stress model did not incorporate all the necessary inputs. The shear modulus and Poisson's ratio were kept constant, even though they are influenced by matrix stiffness, which evolves with temperature. The used CTE functions were derived from analysis; direct measurement of these values would provide more accurate inputs.

The number of tested plies was limited, and due to the random nature of crack initiation, a large standard deviation in the stress onset of microcracking is expected. Increasing the number of tested specimens would improve the statistical significance of the microcracking evolution curves and would decrease the effect of randomness on resulting curves.

7.1.3. Implications for Engineering Design

The tested material demonstrates good adhesion between the matrix and the fibres, as well as good cohesion across the tested temperature range (22°C to -65°C). The tensile strength of the transverse plies does not seem to be a reliable parameter for limiting the maximum allowed stress to minimise microcracking, as such a design parameter should depend on both the ply position and the acceptable crack density for the application. Consequently, the maximum allowable stress could be significantly increased.

To maximise the stress onset of microcracking, the layup should avoid thick blocks of 90° plies. Instead, single 90° plies should be used between plies of different orientations. In addition, the layup design should ensure that no 90° plies are positioned on the outer layers, as these are the most prone to matrix microcracking.

During manufacturing, particular attention should be given to ply consolidation and heat treatment. Defects such as ply waviness, voids, or matrix-rich areas promote crack growth in these regions. While heat treatment can lower the stress-free temperature and thus reduce residual stresses, poorly designed heat treatments can also increase the stress-free temperature, and therefore the residual stresses.

7.1.4. Implications for Academia

Residual stresses in thermoplastic composites are still not fully understood. Further research is needed into how very low temperatures and varying degrees of crystallinity due to heat treatment influence these stresses.

Cracks can nucleate even at relatively low stress levels, so attempting to avoid them completely would result in overly heavy designs. It is therefore crucial to establish an acceptable crack density for service conditions. To achieve this, it is necessary to study how the increased free volume due to microcracking affects the hydrogen permeability of the material.

Non-symmetric layup samples, used in the residual stress model, are sensitive to their width. Improved cutting techniques could reduce the sample width, potentially yielding better results. Additionally, the curvature should be measured closer to the predicted stress-free temperature, rather than relying on linear extrapolation. A better curvature measurement strategy should be employed that does not require opening the climate chamber or the oven during the process, ensuring measurements are taken in thermal equilibrium.

7.2. Recommendations

When continuing the research on matrix microcracking of thermoplastic composites, it is recommended to extend the residual stress model by incorporating proper temperature evolutions for all necessary input parameters and then validating this model. Improving the measurement techniques to accurately capture curvature at different temperatures is also advised. This could involve advanced non-contact laser measurement tools, which would provide more precise data. Understanding how to design a heat treatment that decreases, rather than increases, residual stresses would be beneficial. This requires detailed studies on the effects of different heat treatment protocols on residual stress levels and the development of optimized processes to enhance material performance.

Next, long-term ageing studies should be conducted to assess the durability and reliability of thermoplastic composites under continuous and cyclic loading over extended periods. The results from high-cycle fatigue tests would be more representative of in-service loading. Additionally, microcracking tests should be performed at cryogenic temperatures, as structural changes leading to brittleness may occur that would not be captured in other tests at higher temperatures.

On a broader scale, research should focus on understanding how microcracking density influences hydrogen permeation. It is necessary to determine the microcracking density that merely increases the diffusion rate and the density at which crack networks form continuous paths, leading to hydrogen leakage.

References

[1] United States National Aeronautics and Space Administration. *NASA Technical Note*. en. Google-Books-ID: bEYDZAAzeMUC. National Aeronautics and Space Administration., 1959.

[2] IATA. *Our Commitment to Fly Net Zero by 2050*. en. URL: https://www.iata.org/en/programs/sustainability/flynetzero/ (visited on 08/20/2024).

[3] Subodh K Mital et al. “Review of Current State of the Art and Key Design Issues With Potential Solutions for Liquid Hydrogen Cryogenic Storage Tank Structures for Aircraft Applications”. en. In: (2006).

[4] *COCOLIH2T - Project context and challenge*. en-GB. Apr. 2023. URL: https://www.cocolih2t.eu/context-and-challenges/ (visited on 02/13/2024).

[5] Ni Liu et al. “Progress in research on composite cryogenic propellant tank for large aerospace vehicles”. In: *Composites Part A: Applied Science and Manufacturing* 143 (Apr. 2021), p. 106297. ISSN: 1359-835X. DOI: 10.1016/j.compositesa.2021.106297. URL: https://www.sciencedirect.com/science/article/pii/S1359835X21000270 (visited on 02/13/2024).

[6] Anand Kumar et al. “Thermodynamic investigation of hydrogen enrichment and carbon suppression using chemical additives in ethanol dry reforming”. In: *International Journal of Hydrogen Energy* 41.34 (Sept. 2016), pp. 15149–15157. ISSN: 0360-3199. DOI: 10.1016/j.ijhydene.2016.06.157. URL: https://www.sciencedirect.com/science/article/pii/S0360319916314537 (visited on 02/14/2024).

[7] C Koroneos et al. “Life cycle assessment of hydrogen fuel production processes”. In: *International Journal of Hydrogen Energy* 29.14 (Nov. 2004), pp. 1443–1450. ISSN: 0360-3199. DOI: 10.1016/j.ijhydene.2004.01.016. URL: https://www.sciencedirect.com/science/article/pii/S0360319904000655 (visited on 02/14/2024).

[8] Andreas Westenberger. *Liquid hydrogen fuelled aircraft - system analysis*. FINAL TECHNICAL REPORT (PUBLISHABLE VERSION). Airbus Deutschland GmbH, Jan. 2000, p. 80. URL: https://www.fzt.haw-hamburg.de/pers/Scholz/dglr/hh/text_2004_02_26_Cryoplane.pdf (visited on 02/14/2024).

[9] Dries Verstraete. “Long range transport aircraft using hydrogen fuel”. In: *International Journal of Hydrogen Energy* 38.34 (Nov. 2013), pp. 14824–14831. ISSN: 0360-3199. DOI: 10.1016/j.ijhydene.2013.09.021. URL: https://www.sciencedirect.com/science/article/pii/S036031991302212X (visited on 02/14/2024).

[10] Gunyoung Park, Hyoseong Jang, and Chul Kim. “Design of composite layer and liner for structure safety of hydrogen pressure vessel (type 4)”. en. In: *Journal of Mechanical Science and Technology* 35.8 (Aug. 2021), pp. 3507–3517. ISSN: 1976-3824. DOI: 10.1007/s12206-021-0723-9. URL: https://doi.org/10.1007/s12206-021-0723-9 (visited on 02/14/2024).

[11] Alexander Air, Md Shamsuddoha, and B. Gangadhara Prusty. “A review of Type V composite pressure vessels and automated fibre placement based manufacturing”. In: *Composites Part B: Engineering* 253 (Mar. 2023), p. 110573. ISSN: 1359-8368. DOI: 10.1016/j.compositesb.2023.110573. URL: https://www.sciencedirect.com/science/article/pii/S1359836823000768 (visited on 01/16/2024).

[12] Nour-Eddine Laadel et al. “Permeation barriers for hydrogen embrittlement prevention in metals – A review on mechanisms, materials suitability and efficiency”. In: *International Journal of Hydrogen Energy* 47.76 (Sept. 2022), pp. 32707–32731. ISSN: 0360-3199. DOI: 10.1016/j.ijhydene.2022.07.164. URL: https://www.sciencedirect.com/science/article/pii/S0360319922032165 (visited on 02/14/2024).

[13] Yinan Qiu et al. “Research Progress of Cryogenic Materials for Storage and Transportation of Liquid Hydrogen”. en. In: *Metals* 11.7 (July 2021). Number: 7 Publisher: Multidisciplinary Digital Publishing Institute, p. 1101. ISSN: 2075-4701. DOI: 10.3390/met11071101. URL: https://www.mdpi.com/2075-4701/11/7/1101 (visited on 02/14/2024).

[14] Johannes Macher et al. “Critical review of models for H2-permeation through polymers with focus on the differential pressure method”. In: *International Journal of Hydrogen Energy* 46.43 (June 2021), pp. 22574–22590. ISSN: 0360-3199. DOI: 10.1016/j.ijhydene.2021.04.095. URL: https://www.sciencedirect.com/science/article/pii/S0360319921014440 (visited on 02/14/2024).

[15] Winoj Balasooriya et al. “A Review on Applicability, Limitations, and Improvements of Polymeric Materials in High-Pressure Hydrogen Gas Atmospheres”. In: *Polymer Reviews* 62.1 (Feb. 2022). Publisher: Taylor & Francis _eprint: https://doi.org/10.1080/15583724.2021.1897997, pp. 175–209. ISSN: 1558-3724. DOI: 10.1080/15583724.2021.1897997. URL: https://doi.org/10.1080/15583724.2021.1897997 (visited on 02/14/2024).

[16] Julie Pepin et al. “Determination of key parameters responsible for polymeric liner collapse in hyperbaric type IV hydrogen storage vessels”. In: *International Journal of Hydrogen Energy* 43.33 (Aug. 2018), pp. 16386–16399. ISSN: 0360-3199. DOI: 10.1016/j.ijhydene.2018.06.177. URL: https://www.sciencedirect.com/science/article/pii/S0360319918320810 (visited on 02/14/2024).

[17] Marina Williams. *CompositesWorld: The markets. Pressure vessels (2022)*. en. Dec. 2021. URL: https://etcwinders.com/news/compositesworld-the-markets-pressure-vessels-2022/ (visited on 07/22/2024).

[18] Mohammad Azeem et al. “Application of Filament Winding Technology in Composite Pressure Vessels and Challenges: A Review”. In: *Journal of Energy Storage* 49 (May 2022), p. 103468. ISSN: 2352-152X. DOI: 10.1016/j.est.2021.103468. URL: https://www.sciencedirect.com/science/article/pii/S2352152X2101152X (visited on 02/14/2024).

[19] Brian H. Jones and Min-Chung Li. “Liner-less Tanks for Space Application - Design and Manufacturing Considerations”. In: NTRS Author Affiliations: Kaiser Compositek, Inc. NTRS Document ID: 20040084010 NTRS Research Center: Marshall Space Flight Center (MSFC). Nov. 2003. URL: https://ntrs.nasa.gov/citations/20040084010 (visited on 02/14/2024).

[20] Kaushik Mallick et al. “Ultralight Linerless Composite Tanks for In-Space Applications”. en. In: *Space 2004 Conference and Exhibit*. San Diego, California: American Institute of Aeronautics and Astronautics, Sept. 2004. ISBN: 978-1-62410-084-0. DOI: 10.2514/6.2004-5801. URL: https://arc.aiaa.org/doi/10.2514/6.2004-5801 (visited on 02/14/2024).

[21] Edward H. Glaessgen et al. “Debonding Failure of Sandwich-Composite Cryogenic Fuel Tank with Internal Core Pressure”. en. In: *Journal of Spacecraft and Rockets* 42.4 (July 2005), pp. 613–627. ISSN: 0022-4650, 1533-6794. DOI: 10.2514/1.5567. URL: https://arc.aiaa.org/doi/10.2514/1.5567 (visited on 02/14/2024).

[22] Duo Chen et al. “A Review of the Polymer for Cryogenic Application: Methods, Mechanisms and Perspectives”. en. In: *Polymers* 13.3 (Jan. 2021). Number: 3 Publisher: Multidisciplinary Digital Publishing Institute, p. 320. ISSN: 2073-4360. DOI: 10.3390/polym13030320. URL: https://www.mdpi.com/2073-4360/13/3/320 (visited on 02/14/2024).

[23] Jun-Fei Long et al. “Enhancements in LOX compatibility and fracture toughness of carbon fiber/epoxy composite for liquid oxygen cryotank by simultaneously introducing Al(OH)3 and phosphorous-nitrogen flame retardants”. In: *Composites Communications* 39 (Apr. 2023), p. 101562. ISSN: 2452-2139. DOI: 10.1016/j.coco.2023.101562. URL: https://www.sciencedirect.com/science/article/pii/S2452213923000700 (visited on 02/14/2024).

[24] Jörg Hohe et al. “Performance of fiber reinforced materials under cryogenic conditions—A review”. In: *Composites Part A: Applied Science and Manufacturing* 141 (Feb. 2021), p. 106226. ISSN: 1359-835X. DOI: 10.1016/j.compositesa.2020.106226. URL: https://www.sciencedirect.com/science/article/pii/S1359835X20304620 (visited on 01/19/2024).

[25] Zsombor Sápi and Richard Butler. “Properties of cryogenic and low temperature composite materials – A review”. In: *Cryogenics* 111 (Oct. 2020), p. 103190. ISSN: 0011-2275. DOI: 10.1016/j.cryogenics.2020.103190. URL: https://www.sciencedirect.com/science/article/pii/S0011227520301922 (visited on 02/19/2024).

[26] Jennifer L. Jordan et al. “Mechanical Properties of Low Density Polyethylene”. en. In: *Journal of Dynamic Behavior of Materials* 2.4 (Dec. 2016), pp. 411–420. ISSN: 2199-7454. DOI: 10.1007/s40870-016-0076-0. URL: https://doi.org/10.1007/s40870-016-0076-0 (visited on 02/19/2024).

[27] P. J. Hine et al. “Failure mechanisms in continuous carbon-fibre reinforced PEEK composites”. In: *Composites Science and Technology* 35.1 (Jan. 1989), pp. 31–51. ISSN: 0266-3538. DOI: 10.1016/0266-3538(89)90069-9. URL: https://www.sciencedirect.com/science/article/pii/0266353889900699 (visited on 02/19/2024).

[28] C. A. Mahieux and K. L. Reifsnider. “Property modeling across transition temperatures in polymers: application to thermoplastic systems”. en. In: *Journal of Materials Science* 37.5 (Mar. 2002), pp. 911–920. ISSN: 1573-4803. DOI: 10.1023/A:1014383427444. URL: https://doi.org/10.1023/A:1014383427444 (visited on 01/26/2024).

[29] Z. Zhang and G. Hartwig. “Low-temperature viscoelastic behavior of unidirectional carbon composites”. In: *Cryogenics* 38.4 (Apr. 1998), pp. 401–405. ISSN: 0011-2275. DOI: 10.1016/S0011-2275(98)00022-8. URL: https://www.sciencedirect.com/science/article/pii/S0011227598000228 (visited on 08/27/2024).

[30] J. A. Barnes et al. “Thermal expansion characteristics of PEEK composites”. In: *Journal of Materials Science* 26.8 (Apr. 1991), pp. 2259–2271. ISSN: 1573-4803. DOI: 10.1007/BF00549197. URL: https://doi.org/10.1007/BF00549197.

[31] Ramesh Talreja and Chandra Veer Singh. *Damage and Failure of Composite Materials*. Cambridge: Cambridge University Press, 2012. ISBN: 978-0-521-81942-8. DOI: 10.1017/CBO9781139016063. URL: https://www.cambridge.org/core/books/damage-and-failure-of-composite-materials/181DA4F27223B3A26C8F2D75FC99735B (visited on 02/16/2024).

[32] Thomas Jolliveta, Catherine Peyrac, and Fabien Lefebvre. “Damage of Composite Materials”. In: *Procedia Engineering*. Fatigue Design 2013, International Conference Proceedings 66 (Jan. 2013), pp. 746–758. ISSN: 1877-7058. DOI: 10.1016/j.proeng.2013.12.128. URL: https://www.sciencedirect.com/science/article/pii/S1877705813019619 (visited on 01/24/2024).

[33] Jiaqiao Zhang et al. “Cryogenic mechanical and hydrogen-barrier properties of carbon fiber composites for type V cryo-compressed hydrogen storage vessels”. In: *Composites Communications* 43 (Nov. 2023), p. 101733. ISSN: 2452-2139. DOI: 10.1016/j.coco.2023.101733. URL: https://www.sciencedirect.com/science/article/pii/S2452213923002413 (visited on 01/18/2024).

[34] Susumu Kumagai and Yasuhide Shindo. “Experimental and Analytical Evaluation of the Notched Tensile Fracture of CFRP-Woven Laminates at Low Temperatures”. en. In: *Journal of Composite Materials* 38.13 (July 2004). Publisher: SAGE Publications Ltd STM, pp. 1151–1164. ISSN: 0021-9983. DOI: 10.1177/0021998304042080. URL: https://doi.org/10.1177/0021998304042080 (visited on 02/16/2024).

[35] X. X. Chu et al. “Mechanical and thermal expansion properties of glass fibers reinforced PEEK composites at cryogenic temperatures”. In: *Cryogenics* 50.2 (Feb. 2010), pp. 84–88. ISSN: 0011-2275. DOI: 10.1016/j.cryogenics.2009.12.003. URL: https://www.sciencedirect.com/science/article/pii/S0011227509002033 (visited on 01/29/2024).

[36] Tomohiro Yokozeki, Toshio Ogasawara, and Takashi Ishikawa. “Evaluation of gas leakage through composite laminates with multilayer matrix cracks: Cracking angle effects”. In: *Composites Science and Technology* 66.15 (Dec. 2006), pp. 2815–2824. ISSN: 0266-3538. DOI: 10.1016/j.compscitech.2006.02.024. URL: https://www.sciencedirect.com/science/article/pii/S0266353806000832 (visited on 02/19/2024).

[37] S. M. A. Hosseini et al. “Methodology for the identification of hydrogen gas permeation path in damaged laminates”. en. In: *Proceedings of the 20th European Conference on Composite Materials: Composites Meet Sustainability* (2022). Publisher: EPFL Lausanne, Composite Construction Laboratory. URL: https://repository.tudelft.nl/islandora/object/uuid%3A9d338d09-cad9-4ed4-a4ef-f28c149a9444 (visited on 02/19/2024).

[38] M. Flanagan et al. “Permeability of carbon fibre PEEK composites for cryogenic storage tanks of future space launchers”. In: *Composites Part A: Applied Science and Manufacturing* 101 (Oct. 2017), pp. 173–184. ISSN: 1359-835X. DOI: 10.1016/j.compositesa.2017.06.013. URL: https://www.sciencedirect.com/science/article/pii/S1359835X17302403 (visited on 02/19/2024).

[39] John A. Nairn. “Matrix Microcracking in Composites”. en. In: *Comprehensive Composite Materials*. Elsevier, 2000, pp. 403–432. ISBN: 978-0-08-042993-9. DOI: 10.1016/B0-08-042993-9/00069-3. URL: https://linkinghub.elsevier.com/retrieve/pii/B0080429939000693 (visited on 01/16/2024).

[40] William D. Callister and David G. Rethwisch. *Materials Science And Engineering*. en. 3rd. Wiley, Feb. 2006. ISBN: 978-0-471-73696-7. (Visited on 02/20/2024).

[41] ALFRED PASIEKA/SCIENCE PHOTO LIBRARY. *Photoelastic stress of laboratory glasses - Stock Image - C011/6476*. en. URL: https://www.sciencephoto.com/media/439741/view/photoelastic-stress-of-laboratory-glasses (visited on 07/23/2024).

[42] Ying Shi et al. “Evaluation of principal residual stress and its relationship with crystal orientation and mechanical properties of polypropylene films”. In: *Polymer* 123 (Aug. 2017), pp. 137–143. ISSN: 0032-3861. DOI: 10.1016/j.polymer.2017.07.006. URL: https://www.sciencedirect.com/science/article/pii/S0032386117306651 (visited on 02/20/2024).

[43] Anna Maria El Bayssari. “Etude de l’état des contraintes et des déformations résiduelles dans les composites à matrices thermoplastiques fabriqués par dépose de bandes”. These de doctorat. Nantes Université, Sept. 2022. URL: https://www.theses.fr/2022NANU4035 (visited on 02/20/2024).

[44] Ba Nghiep Nguyen et al. “Modeling the effects of loading scenario and thermal expansion coefficient on potential failure of cryo-compressed hydrogen vessels”. In: *International Journal of Hydrogen Energy* 45.46 (Sept. 2020), pp. 24883–24894. ISSN: 0360-3199. DOI: 10.1016/j.ijhydene.2019.09.200. URL: https://www.sciencedirect.com/science/article/pii/S0360319919336481 (visited on 02/20/2024).

[45] M. Safarabadi and M. M. Shokrieh. “8 - Understanding residual stresses in polymer matrix composites”. In: *Residual Stresses in Composite Materials*. Ed. by Mahmood M. Shokrieh. Woodhead Publishing, Jan. 2014, pp. 197–232. ISBN: 978-0-85709-270-0. DOI: 10.1533/9780857098597.2.197. URL: https://www.sciencedirect.com/science/article/pii/B9780857092700500080 (visited on 07/24/2024).

[46] Mahmood M. Shokrieh. “Residual stresses in composite material”. In: *Residual stresses in composite materials*. Woodhead Publishing Limited, 2014. ISBN: 978-0-85709-270-0.

[47] R. Akkerman. “On the properties of quasi-isotropic laminates”. In: *Composites Part B: Engineering* 33.2 (Mar. 2002), pp. 133–140. ISSN: 1359-8368. DOI: 10.1016/S1359-8368(02)00002-1. URL: https://www.sciencedirect.com/science/article/pii/S1359836802000021 (visited on 02/20/2024).

[48] M. M. Shokrieh, S. Akbari, and A. Daneshvar. “A comparison between the slitting method and the classical lamination theory in determination of macro-residual stresses in laminated composites”. In: *Composite Structures* 96 (Feb. 2013), pp. 708–715. ISSN: 0263-8223. DOI: 10.1016/j.compstruct.2012.10.001. URL: https://www.sciencedirect.com/science/article/pii/S026382231200476X (visited on 08/07/2024).

[49] Patricia P. Parlevliet, Harald E. N. Bersee, and Adriaan Beukers. “Residual stresses in thermoplastic composites—A study of the literature—Part I: Formation of residual stresses”. In: *Composites Part A: Applied Science and Manufacturing* 37.11 (Nov. 2006), pp. 1847–1857. ISSN: 1359-835X. DOI: 10.1016/j.compositesa.2005.12.025. URL: https://www.sciencedirect.com/science/article/pii/S1359835X06000145 (visited on 02/20/2024).

[50] Mael Péron et al. “Measurement and prediction of residual strains and stresses during the cooling of a glass fibre reinforced PA66 matrix composite”. In: *Composites Part A: Applied Science and Manufacturing* 137 (Oct. 2020), p. 106039. ISSN: 1359-835X. DOI: 10.1016/j.compositesa.2020.106039. URL: https://www.sciencedirect.com/science/article/pii/S1359835X20302785 (visited on 02/20/2024).

[51] Patricia P. Parlevliet, Harald E. N. Bersee, and Adriaan Beukers. “Residual stresses in thermoplastic composites—A study of the literature—Part II: Experimental techniques”. In: *Composites Part A: Applied Science and Manufacturing* 38.3 (Mar. 2007), pp. 651–665. ISSN: 1359-835X. DOI: 10.1016/j.compositesa.2006.07.002. URL: https://www.sciencedirect.com/science/article/pii/S1359835X06002223 (visited on 02/20/2024).

[52] 22 September 1999. *X-33 tanks prepared for testing*. en. URL: https://www.flightglobal.com/x-33-tanks-prepared-for-testing/28533.article (visited on 07/23/2024).

[53] Peter Ifju, Donald Myers, and William Schulz. “Residual stress and thermal expansion of graphite epoxy laminates subjected to cryogenic temperatures”. In: *Composites Science and Technology*. Special Issue in Honour of Professor C.T. Sun 66.14 (Nov. 2006), pp. 2449–2455. ISSN: 0266-3538. DOI: 10.1016/j.compscitech.2006.02.011. URL: https://www.sciencedirect.com/science/article/pii/S0266353806000510 (visited on 02/20/2024).

[54] D. M. Grogan et al. “Damage characterisation of cryogenically cycled carbon fibre/PEEK laminates”. In: *Composites Part A: Applied Science and Manufacturing* 66 (Nov. 2014), pp. 237–250. ISSN: 1359-835X. DOI: 10.1016/j.compositesa.2014.08.007. URL: https://www.sciencedirect.com/science/article/pii/S1359835X14002401 (visited on 01/22/2024).

[55] Chen Wang et al. “Modelling of Damage Evolution in Braided Composites: Recent Developments”. In: *Mechanics of Advanced Materials and Modern Processes* 3.1 (Aug. 2017), p. 15. ISSN: 2198-7874. DOI: 10.1186/s40759-017-0030-4. URL: https://doi.org/10.1186/s40759-017-0030-4 (visited on 07/23/2024).

[56] Ming-fa Ren et al. “An integrated macro/micro-scale approach for *in situ* evaluation of matrix cracking in the polymer matrix of cryogenic composite tanks”. In: *Composite Structures* 216 (May 2019), pp. 201–212. ISSN: 0263-8223. DOI: 10.1016/j.compstruct.2019.02.079. URL: https://www.sciencedirect.com/science/article/pii/S0263822318323353 (visited on 02/25/2024).

[57] J. Zheng et al. “A Comparative Study on the Failure Criteria for Predicting the Damage Initiation in Fiber-Reinforced Composites”. en. In: *Mechanics of Composite Materials* 58.1 (Mar. 2022), pp. 125–140. ISSN: 1573-8922. DOI: 10.1007/s11029-022-10016-3. URL: https://doi.org/10.1007/s11029-022-10016-3 (visited on 02/19/2024).

[58] Hiroshi Saito, Hiroki Takeuchi, and Isao Kimpara. “Experimental Evaluation of the Damage Growth Restraining in 90° Layer of Thin-ply CFRP Cross-ply Laminates”. In: *Advanced Composite Materials* 21.1 (Feb. 2012). Publisher: Taylor & Francis _eprint: https://www.tandfonline.com/doi/pdf/10. pp. 57–66. ISSN: 0924-3046. DOI: 10.1163/156855112X629522. URL: https://www.tandfonline.com/doi/abs/10.1163/156855112X629522 (visited on 08/29/2024).

[59] M. A. Caminero et al. “Flexural damage response of symmetric cross-ply carbon fiber reinforced laminates: Effects of thickness and ply-scaling technique”. In: *Mechanics of Advanced Materials and Structures* 28.2 (Jan. 2021). Publisher: Taylor & Francis _eprint: https://doi.org/10.1080/15376494.2018.1553260, pp. 212–219. ISSN: 1537-6494. DOI: 10.1080/15376494.2018.1553260. URL: https://doi.org/10.1080/15376494.2018.1553260 (visited on 08/29/2024).

[60] S. Huguet et al. “Use of acoustic emission to identify damage modes in glass fibre reinforced polyester”. In: *Composites Science and Technology* 62.10 (Aug. 2002), pp. 1433–1444. ISSN: 0266-3538. DOI: 10.1016/S0266-3538(02)00087-8. URL: https://www.sciencedirect.com/science/article/pii/S0266353802000878 (visited on 02/25/2024).

[61] J. A. Pascoe et al. “Using acoustic emission to understand fatigue crack growth within a single load cycle”. In: *Engineering Fracture Mechanics* 194 (May 2018), pp. 281–300. ISSN: 0013-7944. DOI: 10.1016/j.engfracmech.2018.03.012. URL: https://www.sciencedirect.com/science/article/pii/S0013794417306847 (visited on 01/15/2024).

[62] Xi Li. “Unfolding the Early Fatigue Damage Accumulation for Cross-ply Laminates”. en. PhD thesis. TU Delft, 2022. URL: https://repository.tudelft.nl/islandora/object/uuid%3A710d7600-a6c3-4ad2-ada0-214005e28cb2 (visited on 02/25/2024).

[63] Paul J. Schilling et al. “X-ray computed microtomography of internal damage in fiber reinforced polymer matrix composites”. In: *Composites Science and Technology* 65.14 (Nov. 2005), pp. 2071–2078. ISSN: 0266-3538. DOI: 10.1016/j.compscitech.2005.05.014. URL: https://www.sciencedirect.com/science/article/pii/S0266353805001879 (visited on 02/25/2024).

[64] M. Munz et al. “The scanning force microscope as a tool for the detection of local mechanical properties within the interphase of fibre reinforced polymers”. In: *Composites Part A: Applied Science and Manufacturing* 29.9 (Jan. 1998), pp. 1251–1259. ISSN: 1359-835X. DOI: 10.1016/S1359-835X(98)00077-3. URL: https://www.sciencedirect.com/science/article/pii/S1359835X98000773 (visited on 02/25/2024).

[65] Edward C. Peterson, Ranjit R. Patil, and Alan R. Kallemeyer. “A Micromechanical Damage Model for Carbon Fiber Composites at Reduced Temperatures”. en. In: *Journal ofCOMPOSITEMATERIALS* 42 (2008), pp. 2063–2082. DOI: 10.1177/0021998308094547. URL: https://journals.sagepub.com/doi/epdf/10.1177/0021998308094547?src=getftr (visited on 01/29/2024).

[66] Sukjoo Choi and Bhavani V. Sankar. “Micromechanical Analysis of Composite Laminates at Cryogenic Temperatures”. en. In: *Journal of Composite Materials* 40.12 (June 2006). Publisher: SAGE Publications Ltd STM, pp. 1077–1091. ISSN: 0021-9983. DOI: 10.1177/0021998305057365. URL: https://doi.org/10.1177/0021998305057365 (visited on 01/25/2024).

[67] Cheng Huang et al. “Trans-scale modeling framework for failure analysis of cryogenic composite tanks”. In: *Composites Part B: Engineering* 85 (Feb. 2016), pp. 41–49. ISSN: 1359-8368. DOI: 10.1016/j.compositesb.2015.09.023. URL: https://www.sciencedirect.com/science/article/pii/S1359836815005582 (visited on 01/30/2024).

[68] J. Steven Mayes and Andrew C. Hansen. “Composite laminate failure analysis using multicontinuum theory”. In: *Composites Science and Technology*. Failure criteria in fibre reinforced polymer composites Part C: Additional theories conclusions and recommendations 64.3 (Mar. 2004), pp. 379–394. ISSN: 0266-3538. DOI: 10.1016/S0266-3538(03)00219-7. URL: https://www.sciencedirect.com/science/article/pii/S0266353803002197 (visited on 01/30/2024).

[69] John F. Timmerman and James C. Seferis. “Predictive modeling of microcracking in carbon-fiber/epoxy composites at cryogenic temperatures”. en. In: *Journal of Applied Polymer Science* 91.2 (2004), pp. 1104–1110. ISSN: 1097-4628. DOI: 10.1002/app.13172. URL: https://onlinelibrary.wiley.com/doi/abs/10.1002/app.13172 (visited on 02/23/2024).

[70] Karen S. Whitley and Thomas S. Gates. “Thermal/Mechanical Response of a Polymer Matrix Composite at Cryogenic Temperatures”. en. In: *AIAA Journal* 42.10 (Oct. 2004), pp. 1991–2001. ISSN: 0001-1452, 1533-385X. DOI: 10.2514/1.1063. URL: https://arc.aiaa.org/doi/10.2514/1.1063 (visited on 01/25/2024).

[71] K. Ahlborn. “Cryogenic mechanical response of carbon fibre reinforced plastics with thermoplastic matrices to quasi-static loads”. In: *Cryogenics* 31.4 (Apr. 1991), pp. 252–256. ISSN: 0011-2275. DOI: 10.1016/0011-2275(91)90087-D. URL: https://www.sciencedirect.com/science/article/pii/001122759190087D (visited on 01/29/2024).

[72] Patrick Johnson and Fu-Kuo Chang. “Characterization of Matrix Crack-Induced Laminate Failure—Part I: Experiments”. en. In: *Journal of Composite Materials* 35.22 (), pp. 1985–2074. DOI: 10.1106/7RN1-PFBN-XQR9-3KDK. URL: https://journals.sagepub.com/doi/epdf/10.1106/7RN1-PFBN-XQR9-3KDK (visited on 08/13/2024).

[73] John D. Ferry. *Viscoelastic properties of polymers*. en. Third edition. New York Chichester Brisbane Toronto Singapore: John Wiley & Sons, 1980. ISBN: 978-0-471-04894-7.

[74] Caroline A. Schneider, Wayne S. Rasband, and Kevin W. Eliceiri. “NIH Image to ImageJ: 25 years of image analysis”. en. In: *Nature Methods* 9.7 (July 2012). Publisher: Nature Publishing Group, pp. 671–675. ISSN: 1548-7105. DOI: 10.1038/nmeth.2089. URL: https://www.nature.com/articles/nmeth.2089 (visited on 08/13/2024).

[75] J. C. Halpin Affdl and J. L. Kardos. “The Halpin-Tsai equations: A review”. en. In: *Polymer Engineering & Science* 16.5 (1976). _eprint: https://onlinelibrary.wiley.com/doi/pdf/10.1002/pen.760160512, pp. 344–352. ISSN: 1548-2634. DOI: 10.1002/pen.760160512. URL: https://onlinelibrary.wiley.com/doi/abs/10.1002/pen.760160512 (visited on 07/17/2024).

[76] Michael W. Hyer. *Stress analysis of fiber-reinforced composite materials*. en. Updated edition. Lancaster, Pennsylvania: DEStech Publications, Inc, 2009. ISBN: 978-1-932078-86-2.

[77] Toray Advanced Composites. *Toray Cetex® TC1225 data sheet*. Data sheet. Toray Advanced Composites. URL: https://www.toraytac.com/media/3bd72fac-0406-48e4-bfc4-2ffd2398ac0c/fxj5OQ/TAC/Documents/Data_sheets/Thermoplastic/UD%20tapes,%20prepregs%20and%20laminates/Toray-Cetex-TC1225_PAEK_PDS.pdf (visited on 07/21/2024).

[78] Keiichi Shirasu et al. “Experimental and numerical study on open-hole tension/compression properties of carbon-fiber-reinforced thermoplastic laminates”. en. In: *Journal of Composite Materials* 56.14 (June 2022), pp. 2147–2308. DOI: 10.1177/00219983221096880. URL: https://journals.sagepub.com/doi/epub/10.1177/00219983221096880 (visited on 08/05/2024).

A

TU Delft

CHADA

Material characterisation

Material characterization of T800 / TC1225

Used in COCOLIH$_2$T

Template filled by: Matej Moravčík

Overview of the Characterisation

1	**Specimen**	UD and ±45° CFRP, with LM-PAEK thermoplastic matrix and T800 fibres. Tape lay-up with vacuum bagging as consolidation.
2	**Chain of methods**	Standards for UD: ASTM D3039M-17 For ±45°: ASTM D3518M-18
		1. UD specimens tensile tests with biaxial/uniaxial strain gauges and extensometer
		2. ±45° tensile test with extensometer and strain gauge
3	**Data publication**	*N/A*
4	**Access conditions**	*TBD*
5	**Workflow**	*Received panels are cut into desired dimensions.* *All specimen layouts (90°, ±45) except for 0° UD are put into an oven for the heat treatment.* *Tabs made of glass fibre composite material are joined with the CF specimens using Loctite EA 3425 epoxy adhesive.* *Strain gauges are attached to the specimens according to the manufacturer's specifications.* *The specimens are tensile tested using Zwick 250kN tensile machine.* *Standard force, extensometer displacement and strain gauge voltages are recorded during the tests.* *The obtained data is converted into stress strain curves using method in ASTM D3039/ D3518 standards.*

1. Sample		
1.1	**Material**	*TC1225 thermoplastic matrix, T800 carbon fibres*
1.2	**Specimen specifications and nomenclature**	*UD specimens layup* - $[0]_6$ *Nominal specimen thickness: for 0° tests – 15mm* *for 90° specimen – 25 mm* ±45° specimens layup - $[\pm 45]_6$ *Nominal specimen thickness: for* ±45° specimen – 25mm *Nominal length of all specimens is 150mm with tab length of 30mm on each side.* *Nomenclature – XX-YY-Z* *XX – specimen layup – UD for 0° specimens, TRA for 90° specimens, SHR for* ±45° specimen YY – heat treatment – HT for heat treated, NT for not heat treated *Z – specimen number in a series*
1.3	**Manufacturing & preparation**	*1. ATL with a vacuum bag consolidation.* *2. The plates were cut to final dimensions using a diamond saw.* *3. Tabs were bonded to the specimens using Loctite EA 3425 epoxy adhesive.*
1.4	**Test environment**	*Room temperature – lab air – 22°C* *Cold temperature – climate chamber - -65°C*

2. Method		
2.1	**Probe**	*Zwick 250kN tensile testing machine with a climate chamber*
2.2	**Test set-up**	*Tensile test setup with hydraulic clamps for RT testing and manual wedge clamps for low temperature testing*
2.3	**Signal**	*Force, displacement*
2.4	**Detectors**	*1. Zwick machine 250 kN capacity load cell for force measurement* Displacement is measured with multiple different sensors *2a. Extensometer – used for RT displacement measurement for 0°, 90°,* ±45° specimens *2b. Biaxial strain gauge – used for RT displacement measurement in 0° specimens in both along the fibres and transversely to fibres directions* *2c. Axial strain gauge – used for RT measurement of transverse shortening of* ±45° specimens and for cold temperature tests of main axis measurement for 0° and 90° specimens
2.5	**Test procedure**	*Specimens were loaded quasi-statically under displacement control, with 0.1 mm/min displacement rate. The samples were loaded until final failure.*
2.6	**Input parameters**	*The tests were performed at 0.1mm/min displacement rate.* *The room temperature tests were performed at around 22°C, with slight variation due to multiple days of testing.* *The cold temperature tests were performed in a climate chamber set to -65°C, however temperature variation up to* ±8°C was measured in the vicinity of the samples during the testing.

3. Raw Data		
3.1	**Raw Data**	*For the room temperature tests, the obtained data is stored in following files:* *0° UD test in UD24_4_2024-UD2 – where sheets have name Z, which corresponds do UD-NT-Z specimen nomenclature. The column C has stored extensometer displacements in mm, which gauge length was set to 50 mm, the column D Standard force in N from the Zwick 250kN loadcell. The columns E and F have stored transverse and along-the-fibre strain gauge voltage in V, except for sample UD-NT-6 for which along-the-fibre voltage in in the column E and transverse in column F. The bridge setting for the columns E for all samples was set to 10mV/V, in which 10V of signal is equal to 2% of strain. The columns F have 5mV/V, which means 10V of signal corresponds to 1% of strain.* *90° UD test in TRA29_4_2024-TRA – where sheets have name TRA-HT-Z, where Z corresponds to the number of the specimen. The extensometer standard travel in mm is stored in column C,*

		which gauge length was set to 30mm. The column D has stored standard force in N from the Zwick 250kN loadcell. ±45° tensile shear test in SHR07_5_2024-SHR – where sheet name SHR-HT-Z represents the sample number in the series. The columns B have stored Standard force in N from Zwick 250kN loadcell. The columns C have stored transverse strain gauge voltage in V, with bridge setting of 20mV/V, where 10V of voltage represents 4% of strain. The columns D have stored extensometer Standard travel in mm, which gauge length of 30mm. *For the low temperature tests, the obtained data is stored in following files:* *0° UD test in cold_UD-NT_tensile – where sheet name UD-NT-Z represents sample number is series. The columns D have stored Standard force in N. The axial displacement in measured by strain gauge, which voltage in V is stored in columns E. The bridge setting is 5mV/V where 10V corresponds to 1% of strain.* *90° UD test in cold_TRA-HT-10-15 where sheet name TRA-HT-Z represents the sample number. The columns D have stored Standard force in N. The axial displacement in measured by strain gauge, which voltage in V is stored in columns E. The bridge setting is 20mV/V where 10V corresponds to 4% of strain* *For all tests, the specimen cross-sectional area is recorded in each file under sheet Results.*
3.2	**Data acquisition rate**	*The Zwick machine recorded data points 10 times every second.*

4. Data Processing		
4.1	**Data filtering processes**	*For some clamp slippage, data was altered to delete horizontal part of displacement force curve. This was done manually.*
4.2	**Properties or relationships of interest**	*Stiffness (E) is slope of linear relationship between strain and stress.*
4.2	**Data analysis procedures**	*The raw data of standard force was converted to stress by dividing it by specimen cross-section area. Displacement was converted into strain, depending on data acquisition by division by extensometer gauge or by bridge setting for strain gauge voltages.* *Afterwards, the slope of linear part was determined at instances set by standard* ASTM D3039M-17 for UD tests and ASTM D3518M-18 for shear tests.

CHADA

Visual observation and characterization of microcracks in thermoplastic composite materials

Microcracking testing

Used in COCOLIH$_2$T

Template filled by: *Matej Moravčík*

Overview of the Characterisation

1	**Specimen**	*Multiple cross-ply layups of T800/T1225 thermoplastic composite are loaded to a given load level, and their edge is scanned using optical microscopy to find microcracks. Then the microcracks are measured and counted.*
2	**Chain of methods**	*1. Quasi-static loading to predetermined load level*
		2. Scanning the sample with optical microscope
3	**Data publication**	*TBD*
4	**Access conditions**	*TBD*
5	**Workflow**	*Received panels are cut into desired dimensions.* *All specimens are put into an oven for the heat treatment.* *Tabs made of glass fibre composite material are joined with the CF specimens using Loctite EA 3425 epoxy adhesive.* *Edge of each sample is polished. The grain sizes used are 340, 600, 1000, 2000, 4000 and lastly a chemical polish in performed.* *The quality of polish is accessed with an optical microscope.*

1. Sample		
1.1	**Material**	*TC1225 thermoplastic matrix, T800 carbon fibres*
1.2	**Specimen specifications and nomenclature**	*Five different cross-ply layups are tested:* *CR* - $[90/0/90/0/90/90]_S$ *CR1* - $[0/90_2]_S$ *CR2* - $[0/90]_S$ *CR3* - $[90/0/90]_T$ *CR4* - $[0/90/0]_T$ *Nominal length of all specimens is 150mm with tab length of 30mm on each side. Nominal thickness of a specimen is 25mm.* *Nomenclature – XX-YY-Z* *XX – specimen layup* YY – heat treatment – HT for heat treated, NT for not heat treated *Z – specimen number in a series*
1.3	**Manufacturing & preparation**	*1. ATL with a vacuum bag consolidation.* *2. The plates were cut to final dimensions using a diamond saw.* *3. Tabs were bonded to the specimens using Loctite EA 3425 epoxy adhesive.*
1.4	**Test environment**	*Room temperature – lab air – 22°C* *Cold temperature – climate chamber - -65°C*

2. Method		
2.1	**Probe**	*Zwick 250kN tensile machine with a climate chamber*
2.2	**Test set-up**	*Cyclic tensile testing with interruptions to optically access crack density of the specimen. Tests also done in the climate chamber at low temperatures.*
2.3	**Signal**	*Force, extensometer standard travel, crosshead displacement*
2.4	**Detectors**	*1. Zwick 250kN extensometer* *2. Zwick 250 kN capacity load cell for force measurement* *3. Zwick 250kN cross head displacement sensor*
2.5	**Test procedure**	*Specimens were loaded quasi-statically under displacement control, with 0.5 mm/min displacement rate. The samples were loaded until predetermined load level.*
2.6	**Input parameters**	*The tests were performed at 0.5mm/min displacement rate.* *The room temperature tests were performed at around 22°C, with slight variation due to multiple days of testing.* *The cold temperature tests were performed in a climate chamber set to -65°C, however temperature variation up to* ±8°C was measured in the vicinity of the samples during the testing.

3. Raw Data		
3.1	**Raw Data**	*All force displacement data are stored in folder named Microcracking raw data. The nomenclature of the .xls files is the same as the nomenclature of the samples:* *Nomenclature – XX-YY-Z.xls* *XX – specimen layup* YY – heat treatment – HT for heat treated, NT for not heat treated *Z – specimen number in a series* *Samples which name starts cold_ XX-YY-Z.xls were tested at -65°C. The second row in the files is the Standard force reading in N and the third row is the Standard travel of the extensometer in mm. Each sheet is named as SAMPLE NAME-LOAD LEVEL.* *The pictures of the cracks are stored in Microcracking photos folder. Inside of it are folder RT for the room temperature tests and CT for cold temperature test. In each of these folders are folders per sample family, then per sample inside a family and finally per sample tested at given load level.*

		Extensometer gauge length for all of the measurements was set to 30mm.
3.2	**Data acquisition rate**	*The Zwick machine recorded data points 10 times every second. Optical microscopy scan of an edge of the sample was performed after each load step.*

4. Data Processing		
4.1	**Data filtering processes**	*For some clamp slippage, data was altered to delete horizontal part of displacement force curve. This was done manually.*
4.2	**Properties or relationships of interest**	*The length of crack observed was divided by local ply thickness to get relative crack length. The relative crack lengths were summed in each load instance and divided by the observed edge length to get crack density per millimetre.*
4.2	**Data analysis procedures**	*Firstly, standard force was converted to stress by dividing it by specimen cross-section area. Displacement was converted into strain, depending on data acquisition by division by extensometer gauge. Then the strain stress curve was divided into n intervals and the stiffness is evaluated at each interval. Then the stiffness evolution was plotted against maximum load at given interval to obtain stiffness evolution graphs.* *The obtained crack densities are plotted against local applied stress level σ22. A Weibull curve was model fitted into data to obtain model prediction. Firstly, the shape parameter was obtained to fit all selected data points. IF multiple samples/plies are used in the selected, the strength parameter of Weibull model is obtained as average strength of model fit with the found shape parameter per sample.*

B

Microcracking Detailed Data

Test name: Microcracking test - CR - RT
Standard followed: -
Operator: Matej Moravcik
Material: TC1225/T800
Temperature RT
Layup: $[90/0/90/0/90/90]_s$

Individual crack count [-]

Name	Layer	Applied load [kN] 20.00	24.00	28.00	32.00
CR-HT-1	I - 90°	0.00	0.00	0.00	0.35
	II - 90°	0.00	0.00	0.00	0.00
	III - 4x90°	0.30	0.30	0.90	0.90
	IV - 90°	1.00	1.00	1.00	1.45
	V - 90°	9.92	12.49	20.89	24.39

	Layer	Applied load [kN] 18.00	22.00	26.00	30.00
CR-HT-2	I - 90°	1.44	1.44	2.95	6.28
	II - 90°	0.00	0.00	0.00	0.57
	III - 4x90°	0.15	0.00	0.19	0.84
	IV - 90°	0.00	0.00	0.00	0.33
	V - 90°	5.20	10.97	12.76	19.61

	Layer	Applied load [kN] 13.00	15.00	17.00	21.00
CR-HT-3	I - 90°	0.00	0.00	0.00	0.58
	II - 90°	0.00	0.00	0.00	0.00
	III - 4x90°	0.00	0.00	0.00	0.00
	IV - 90°	0.00	0.00	0.00	0.00
	V - 90°	4.20	5.72	6.26	10.38

Crack density [1/mm]

Local stress [MPa] 78.7110	94.4532	110.1954	125.9376
0.0000	0.0000	0.0000	0.0069
0.0000	0.0000	0.0000	0.0000
0.0059	0.0059	0.0178	0.0178
0.0198	0.0198	0.0198	0.0287
0.1962	0.2470	0.4131	0.4823

Local stress [MPa] 75.5350	92.3206	109.1061	125.8917
0.0250	0.0250	0.0513	0.1092
0.0000	0.0000	0.0000	0.0099
0.0026	0.0026	0.0033	0.0146
0.0000	0.0000	0.0000	0.0057
0.0904	0.1907	0.2218	0.3409

Local stress [MPa] 48.2720	55.6985	63.1249	77.9778
	0.0000	0.0000	0.0118
0.0000	0.0000	0.0000	0.0000
0.0000	0.0000	0.0000	0.0000
0.0000	0.0000	0.0000	0.0000
0.0858	0.1168	0.1278	0.2120

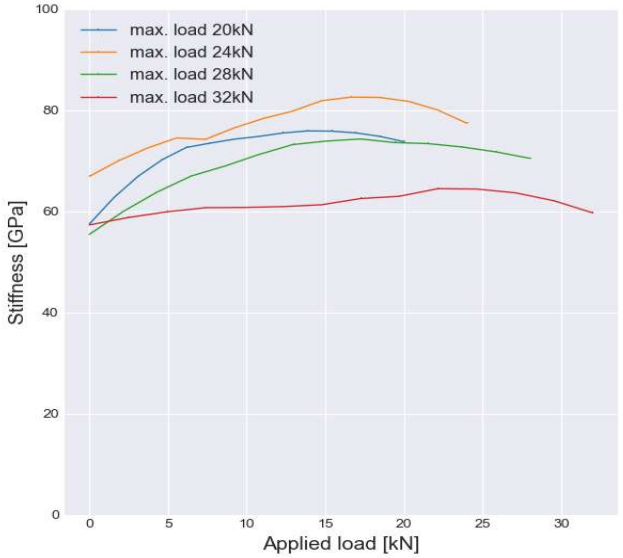
max. load 20kN
max. load 24kN
max. load 28kN
max. load 32kN
Stiffness [GPa]
Applied load [kN]

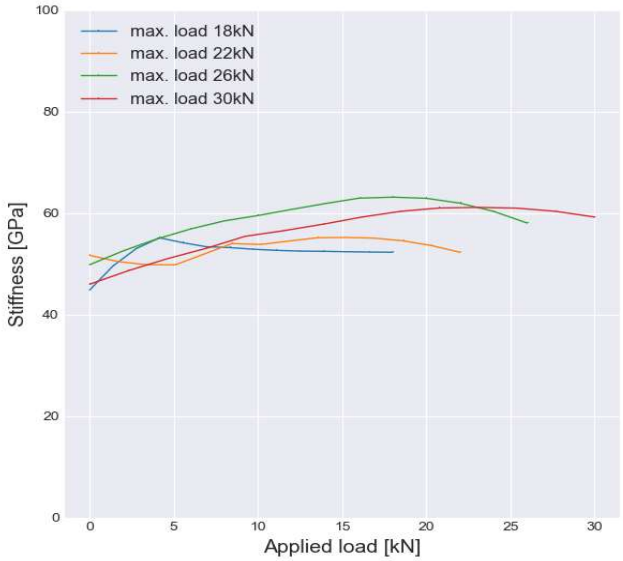
max. load 18kN
max. load 22kN
max. load 26kN
max. load 30kN
Stiffness [GPa]
Applied load [kN]

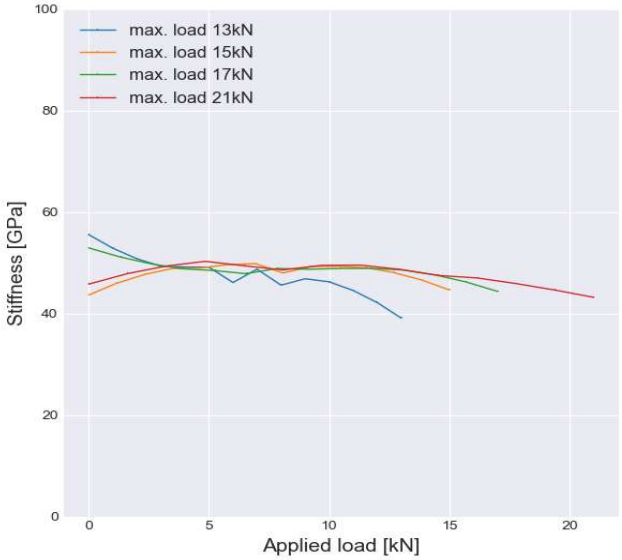
max. load 13kN
max. load 15kN
max. load 17kN
max. load 21kN
Stiffness [GPa]
Applied load [kN]

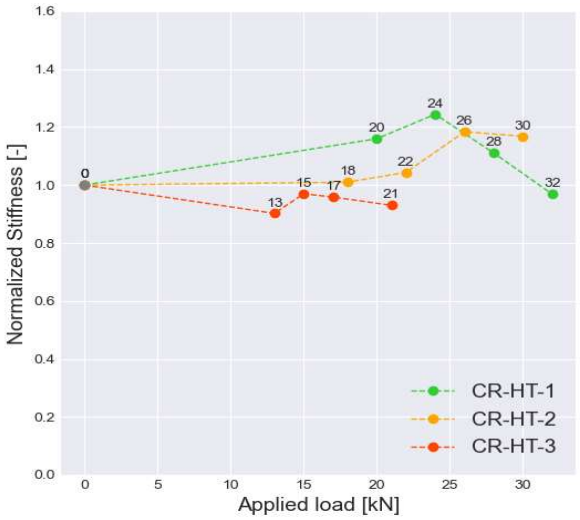
Normalized Stiffness [-]
Applied load [kN]
CR-HT-1
CR-HT-2
CR-HT-3

Test name:	Microcracking test - CR1 - RT
Standard followed:	-
Operator:	Matej Moravcik
Material:	TC1225/T800
Temperature	RT
Layup:	$[0/90_2]_s$

Individual crack count [-]

		Applied load [kN]				
Name	Layer	5.00	7.50	10.00	12.00	15.00
CR-HT-1	I - 90°	0.00	0.15	0.48	0.75	1.36

		Applied load [kN]	
Name	Layer	8.00	9.66
CR-HT-2	I - 90°	0.45	0.8

		Applied load [kN]		
Name	Layer	7.00	9.00	9.40
CR-HT-3	I - 90°	0.39	0.59	1.27

Crack density [1/mm]

		Local stress [MPa]				
Name	Layer	41.4380	62.1570	82.8760	99.4512	124.3140
CR-HT-1	I - 90°	0.0000	0.0026	0.0082	0.0128	0.0232

		Local stress [MPa]	
Name	Layer	67.1500	81.0836
CR-HT-2	I - 90°	0.0079	0.0140

		Local stress [MPa]		
Name	Layer	59.0390	75.9073	79.2809
CR-HT-3	I - 90°	0.0067	0.0101	0.0217

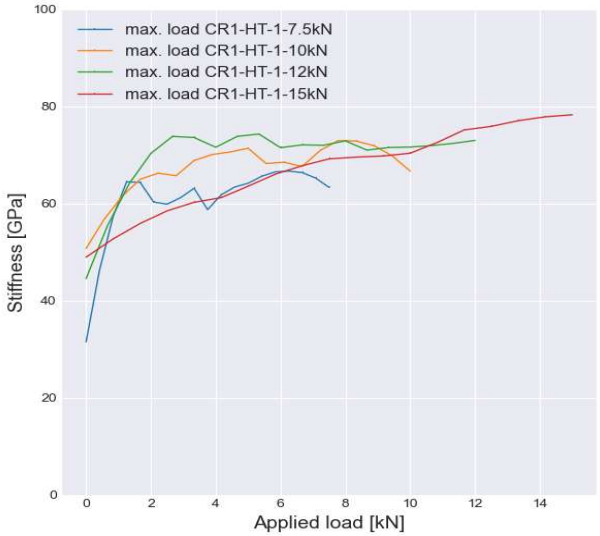
max. load CR1-HT-1-7.5kN
max. load CR1-HT-1-10kN
max. load CR1-HT-1-12kN
max. load CR1-HT-1-15kN
Stiffness [GPa]
Applied load [kN]

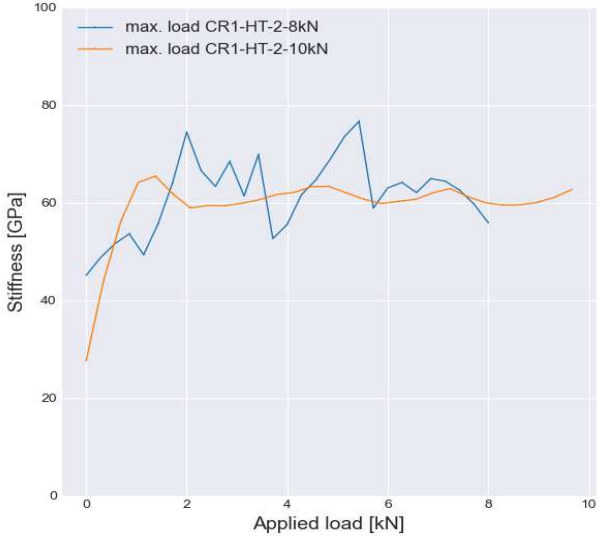
max. load CR1-HT-2-8kN
max. load CR1-HT-2-10kN
Stiffness [GPa]
Applied load [kN]

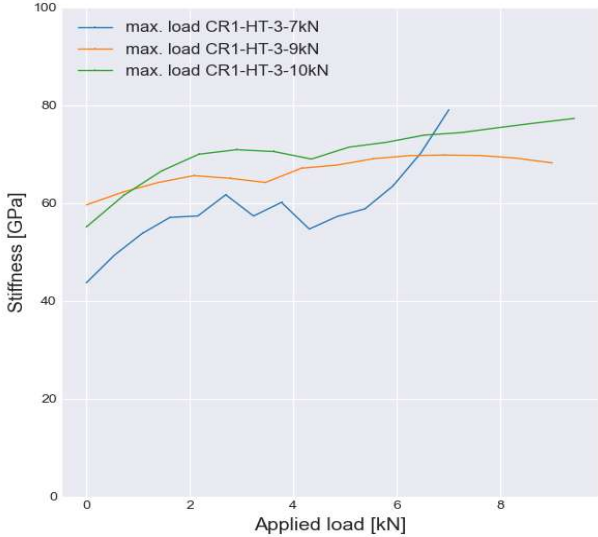
max. load CR1-HT-3-7kN
max. load CR1-HT-3-9kN
max. load CR1-HT-3-10kN
Stiffness [GPa]
Applied load [kN]

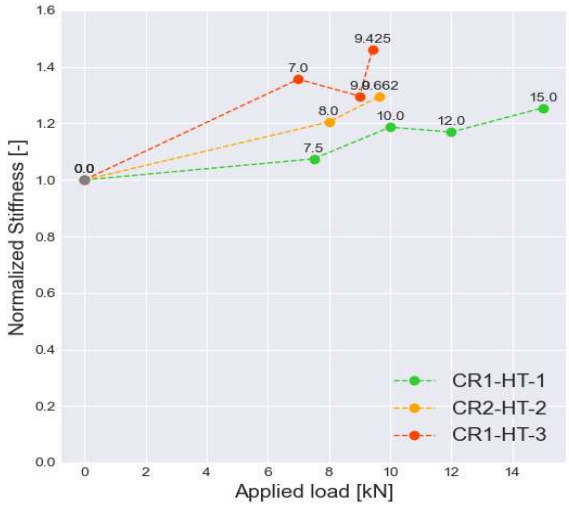
9.425
7.0
9.662
8.0
10.0
12.0
15.0
7.5
0.0
CR1-HT-1
CR2-HT-2
CR1-HT-3
Normalized Stiffness [-]
Applied load [kN]

Test name:	Microcracking test - CR2 - RT
Standard followed:	-
Operator:	Matej Moravcik
Material:	TC1225/T800
Temperature	RT
Layup:	$[0/90]_s$

Individual crack count [-]

		Applied load [kN]			
Name	Layer	4.00	6.00	8.00	10.00
CR2-HT-1	I - 2x90°	0.17	0.27	0.57	1.64

		Applied load [kN]			
Name	Layer	4.00	6.00	8.00	10.00
CR2-HT-2	I - 2x90°	0.08	0.64	3.48	9.40

		Applied load [kN]			
Name	Layer	4.00	6.00	8.00	10.00
CR2-HT-3	I - 2x90°	0.32	0.92	3.16	9.01

Crack density [1/mm]

		Local stress [MPa]			
Name	Layer	35.6850	53.5275	71.3700	89.2125
CR2-HT-1	I - 2x90°	0.0035	0.0056	0.0118	0.0341

		Local stress [MPa]			
Name	Layer	36.8740	55.3110	73.7480	92.1850
CR2-HT-2	I - 2x90°	0.0015	0.0118	0.0642	0.1734

		Local stress [MPa]			
Name	Layer	36.7650	55.1475	73.5300	91.9125
CR2-HT-3	I - 2x90°	0.0065	0.0187	0.0642	0.1830

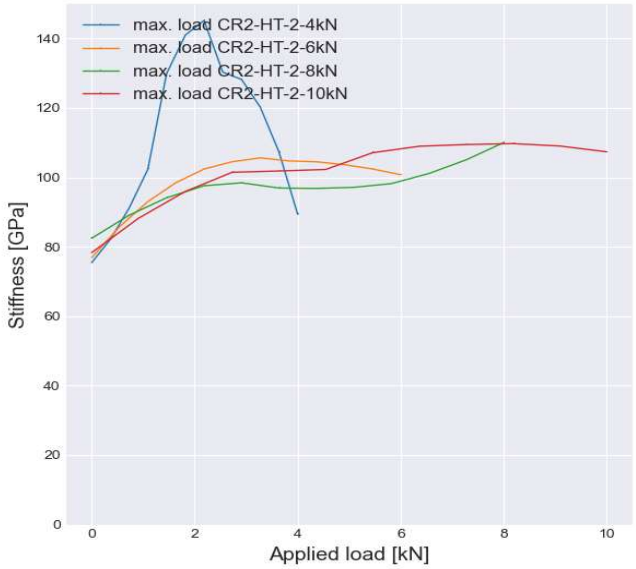
max. load CR2-HT-2-4kN
max. load CR2-HT-2-6kN
max. load CR2-HT-2-8kN
max. load CR2-HT-2-10kN
Stiffness [GPa]
Applied load [kN]

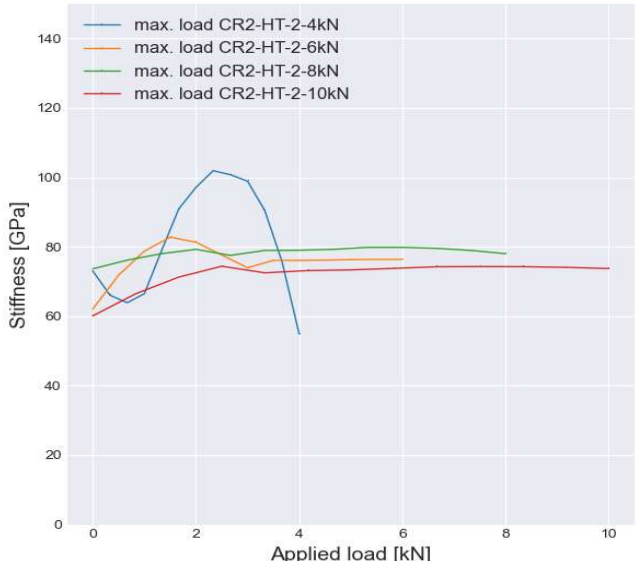
max. load CR2-HT-2-4kN
max. load CR2-HT-2-6kN
max. load CR2-HT-2-8kN
max. load CR2-HT-2-10kN
Stiffness [GPa]
Applied load [kN]

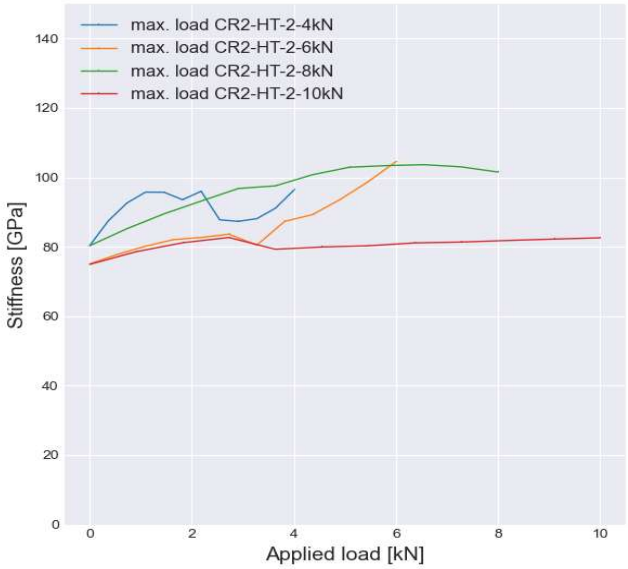
max. load CR2-HT-2-4kN
max. load CR2-HT-2-6kN
max. load CR2-HT-2-8kN
max. load CR2-HT-2-10kN
Stiffness [GPa]
Applied load [kN]

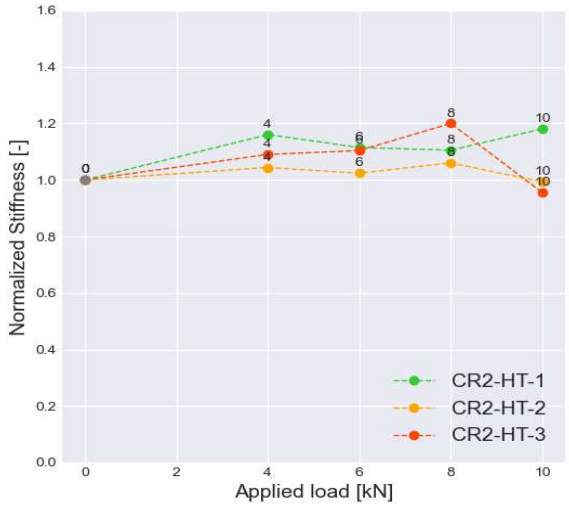
Normalized Stiffness [-]
Applied load [kN]
CR2-HT-1
CR2-HT-2
CR2-HT-3

Test name:	Microcracking test - CR3 - RT
Standard followed:	-
Operator:	Matej Moravcik
Material:	TC1225/T800
Temperature	RT
Layup:	$[90/0/90]_T$

Individual crack count [-]

		Applied load [kN]			
Name	Layer	3.00	4.00	5.00	6.00
CR3-HT-3	I - 90°	1.47	6.91	8.36	13.00
	II - 90°	0.57	2.39	4.19	4.87

Crack density [1/mm]

Local stress [MPa]			
50.3820	67.1760	83.9700	100.7640
0.0256	0.1203	0.1455	0.2262
0.00992	0.041594	0.07292	0.084755

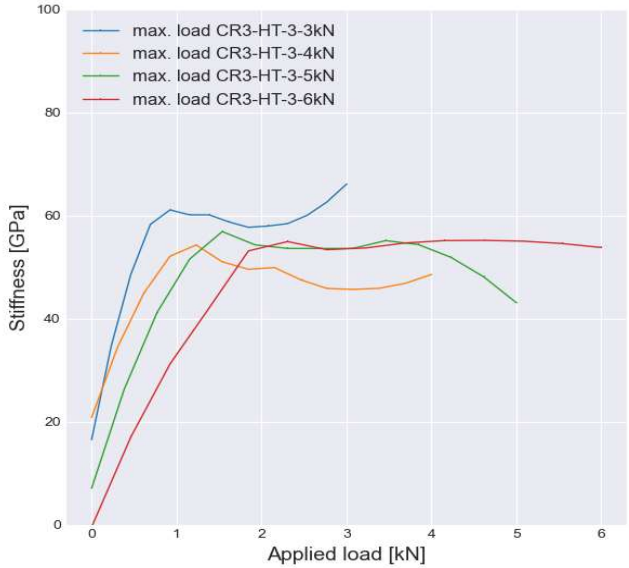
max. load CR3-HT-3-3kN
max. load CR3-HT-3-4kN
max. load CR3-HT-3-5kN
max. load CR3-HT-3-6kN
Stiffness [GPa]
Applied load [kN]
0
20
40
60
80
100
0
1
2
3
4
5
6

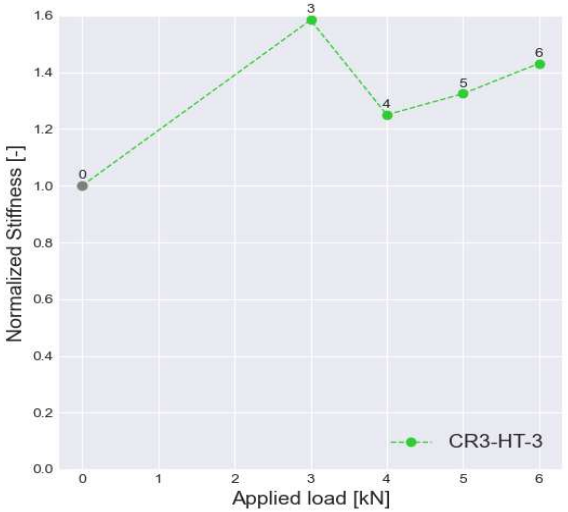
Normalized Stiffness [-]
Applied load [kN]
CR3-HT-3
0.0
0.2
0.4
0.6
0.8
1.0
1.2
1.4
1.6
0
1
2
3
4
5
6

Test name:	Microcracking test - CR4 - RT
Standard followed:	-
Operator:	Matej Moravcik
Material:	TC1225/T800
Temperature	RT
Layup:	$[0/90/0]_T$

Individual crack count [-]

		Applied load [kN]			
Name	Layer	4.00	6.00	8.00	10.00
CR4-HT-1	I - 90°	0.35	0.67	1.00	1.28

		Applied load [kN]			
Name	Layer	4.00	6.00	8.00	10.00
CR4-HT-2	I - 90°	0.00	0.50	0.86	2.16

		Applied load [kN]			
Name	Layer	4.00	6.00	8.00	10.00
CR4-HT-3	I - 90°	0.22	0.22	0.22	0.74

Crack density [1/mm]

		Local stress [MPa]			
Name	Layer	35.4450	53.1675	70.8900	88.6125
CR4-HT-1	I - 90°	0.0061	0.0117	0.0175	0.0224

		Local stress [MPa]			
Name	Layer	37.0400	55.5600	74.0800	92.6000
CR4-HT-2	I - 90°	0.0000	0.0089	0.0152	0.0383

		Local stress [MPa]			
Name	Layer	36.0120	54.0180	72.0240	90.0300
CR4-HT-3	I - 90°	0.0039	0.0039	0.0039	0.0132

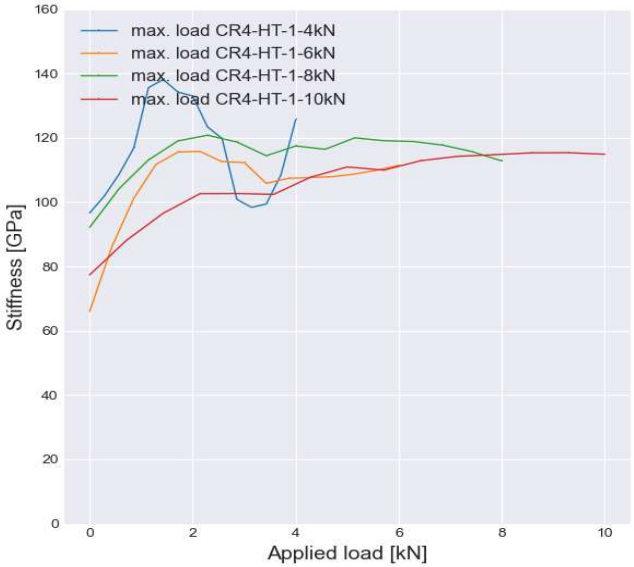
max. load CR4-HT-1-4kN
max. load CR4-HT-1-6kN
max. load CR4-HT-1-8kN
max. load CR4-HT-1-10kN
Stiffness [GPa]
Applied load [kN]

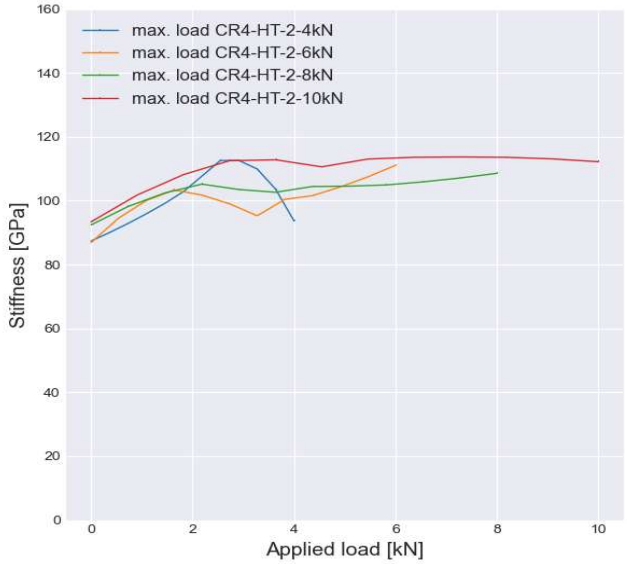
max. load CR4-HT-2-4kN
max. load CR4-HT-2-6kN
max. load CR4-HT-2-8kN
max. load CR4-HT-2-10kN
Stiffness [GPa]
Applied load [kN]

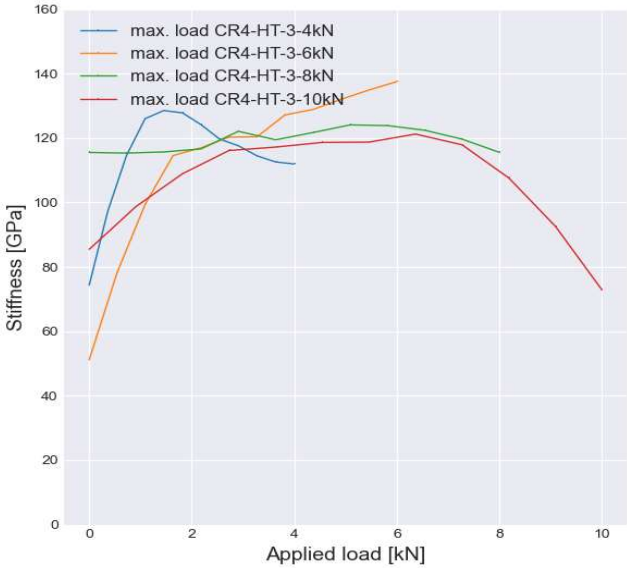
max. load CR4-HT-3-4kN
max. load CR4-HT-3-6kN
max. load CR4-HT-3-8kN
max. load CR4-HT-3-10kN
Stiffness [GPa]
Applied load [kN]

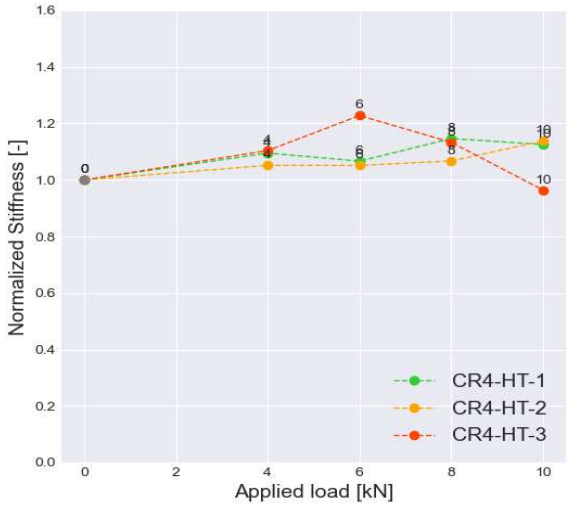
Normalized Stiffness [-]
CR4-HT-1
CR4-HT-2
CR4-HT-3
Applied load [kN]

Test name: Microcracking test - CR - cold temperature
Standard followed: -
Operator: Matej Moravcik
Material: TC1225/T800
Temperature -65°C
Layup: $[90/0/90/0/90/90]_s$

Individual crack count [-]

Crack density [1/mm]

Residual thermal stress:
29.6929 MPa

		Applied load [kN]				Local external stress [MPa]			
Name	Layer	10.00	12.50	15.00	17.50	36.9100	46.1375	55.3650	64.5924
CR-HT-4	I - 90°	0.00	0.00	2.23	4.36	0.0000	0.0000	0.0399	0.0781
	II - 90°	0.00	0.00	0.00	0.26	0.0000	0.0000	0.0000	0.0047
	III - 4x90°	0.00	0.00	0.00	0.03	0.0000	0.0000	0.0000	0.0005
	IV - 90°	0.00	0.81	0.81	0.81	0.0000	0.0145	0.0145	0.0145
	V - 90°	2.31	3.71	4.38	6.31	0.0414	0.0665	0.0785	0.1130

		Applied load [kN]				Local external stress [MPa]			
	Layer	10.00	12.50	15.00	17.50	40.5311	50.6639	60.7967	70.9295
CR-HT-5	I - 90°	0.11	0.11	0.33	1.85	0.0020	0.0020	0.0061	0.0341
	II - 90°	0.00	0.00	0.00	0.41	0.0000	0.0000	0.0000	0.0076
	III - 4x90°	0.00	0.08	0.12	0.14	0.0000	0.0015	0.0022	0.0026
	IV - 90°	0.75	0.75	0.75	0.75	0.0138	0.0138	0.0138	0.0138
	V - 90°	3.28	6.55	8.34	9.06	0.0604	0.1207	0.1537	0.1670

		Applied load [kN]				Local external stress [MPa]			
	Layer	4.30	10.50	13.00	15.50	22.1436	54.0717	66.9459	79.8201
CR-HT-6	I - 90°	0.00	0.07	0.94	1.37	0.0000	0.0013	0.0176	0.0257
	II - 90°	0.00	0.00	0.00	0.11	0.0000	0.0000	0.0000	0.0021
	III - 4x90°	0.00	0.05	0.05	0.05	0.0000	0.0009	0.0009	0.0009
	IV - 90°	0.00	0.10	0.10	0.14	0.0000	0.0019	0.0019	0.0026
	V - 90°	1.42	2.76	3.30	8.55	0.0266	0.0517	0.0618	0.1601

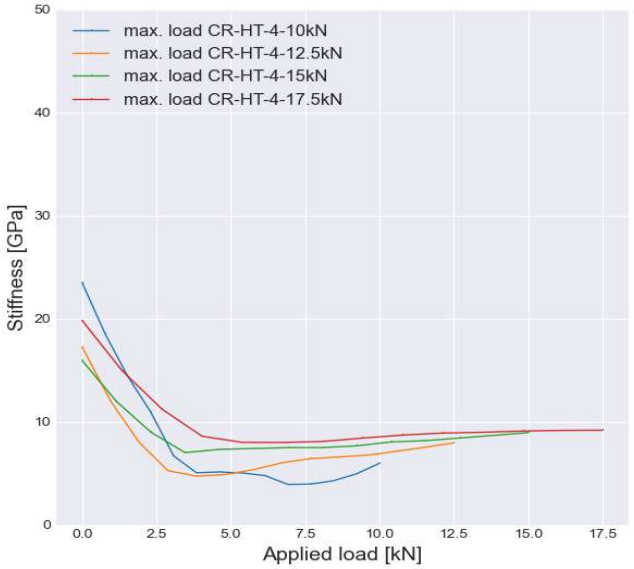
max. load CR-HT-4-10kN
max. load CR-HT-4-12.5kN
max. load CR-HT-4-15kN
max. load CR-HT-4-17.5kN
Stiffness [GPa]
Applied load [kN]

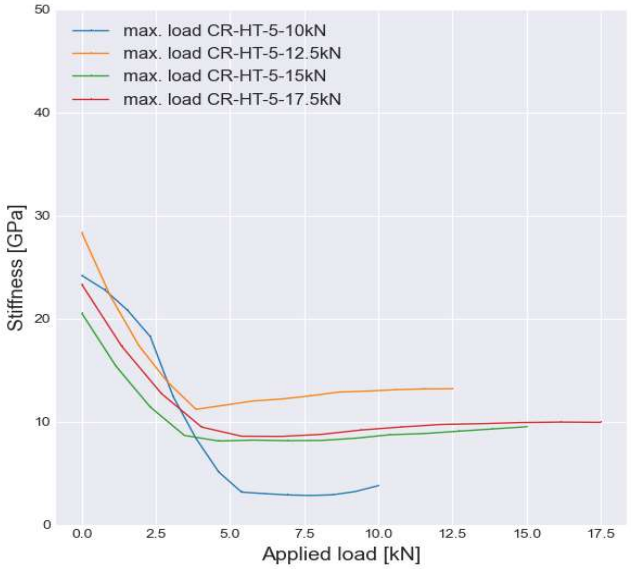
max. load CR-HT-5-10kN
max. load CR-HT-5-12.5kN
max. load CR-HT-5-15kN
max. load CR-HT-5-17.5kN
Stiffness [GPa]
Applied load [kN]

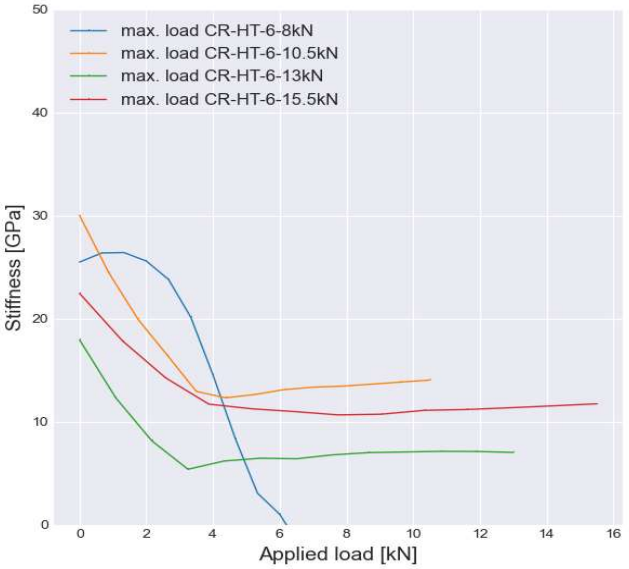
max. load CR-HT-6-8kN
max. load CR-HT-6-10.5kN
max. load CR-HT-6-13kN
max. load CR-HT-6-15.5kN
Stiffness [GPa]
Applied load [kN]

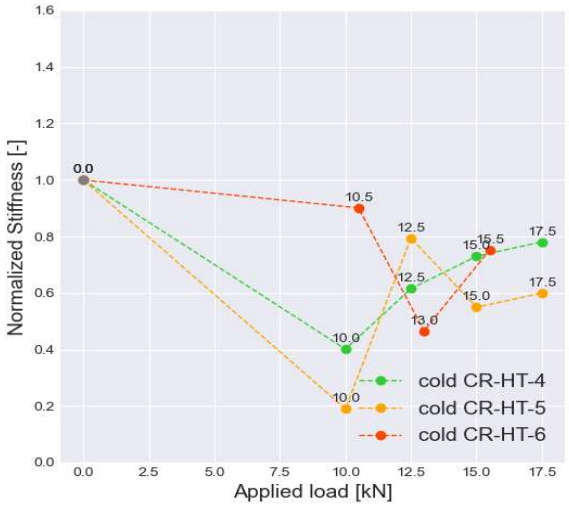
Normalized Stiffness [-]
Applied load [kN]
cold CR-HT-4
cold CR-HT-5
cold CR-HT-6

Test name: Microcracking test - CR2 - cold temperature
Standard followed: -
Operator: Matej Moravcik
Material: TC1225/T800
Temperature -65°C
Layup: $[0/90]_s$

Individual crack count [-]

Crack density [1/mm]

Residual thermal stress:
29.6929 MPa

		Applied load [kN]			Local stress [MPa]		
Name	Layer			7.00			64.4280
CR2-HT-4	I - 2x90°	-	-	0.20	-	-	0.0041

		Applied load [kN]			Local stress [MPa]		
Name	Layer	3.00	5.00	7.00	27.6120	46.0200	64.4280
CR2-HT-5	I - 2x90°	0.00	0.41	0.86	0.0000	0.0090	0.0189

		Applied load [kN]			Local stress [MPa]		
Name	Layer	3.00	5.00	7.00	26.8860	44.8100	62.7340
CR2-HT-6	I - 2x90°	0.00	0.35	1.03	0.0000	0.0068	0.0200

- test results lost

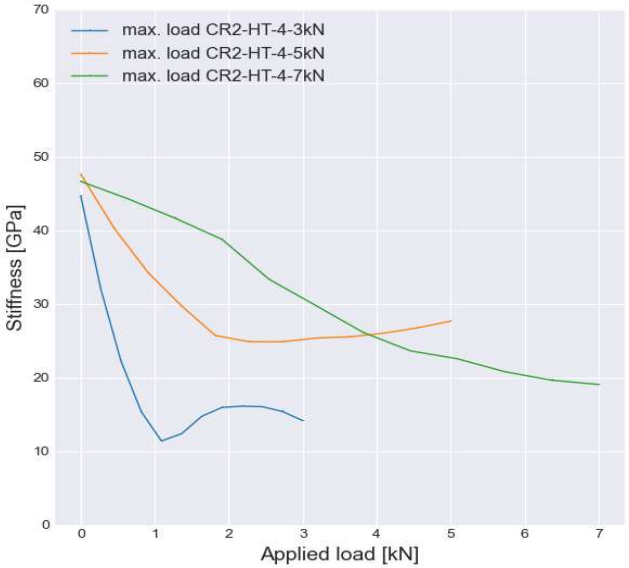
max. load CR2-HT-4-3kN
max. load CR2-HT-4-5kN
max. load CR2-HT-4-7kN
Stiffness [GPa]
Applied load [kN]

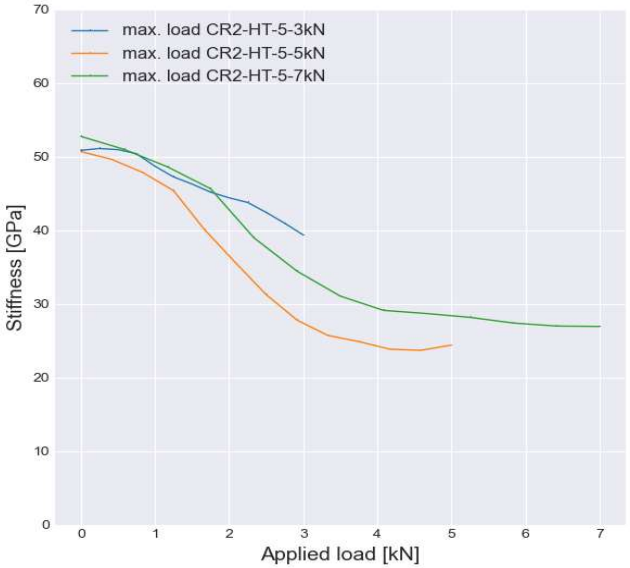
max. load CR2-HT-5-3kN
max. load CR2-HT-5-5kN
max. load CR2-HT-5-7kN
Stiffness [GPa]
Applied load [kN]

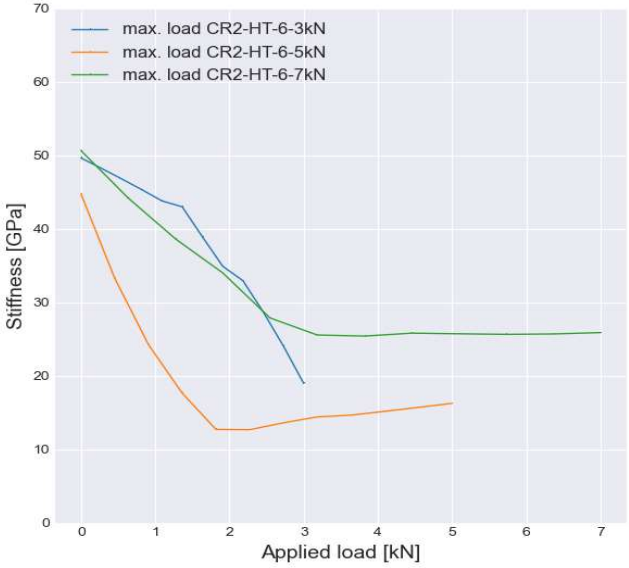
max. load CR2-HT-6-3kN
max. load CR2-HT-6-5kN
max. load CR2-HT-6-7kN
Stiffness [GPa]
Applied load [kN]

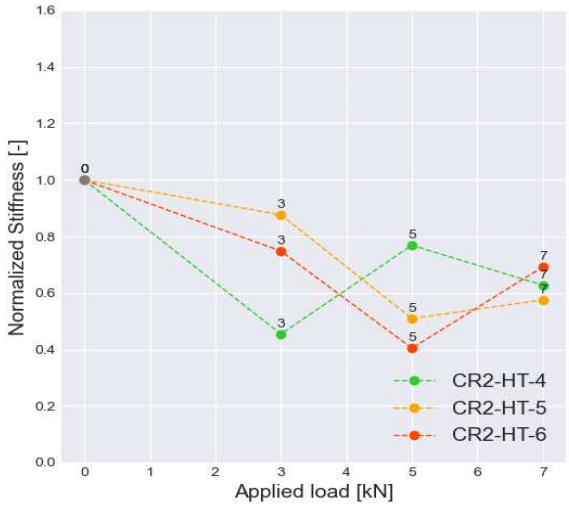
Normalized Stiffness [-]
Applied load [kN]
CR2-HT-4
CR2-HT-5
CR2-HT-6